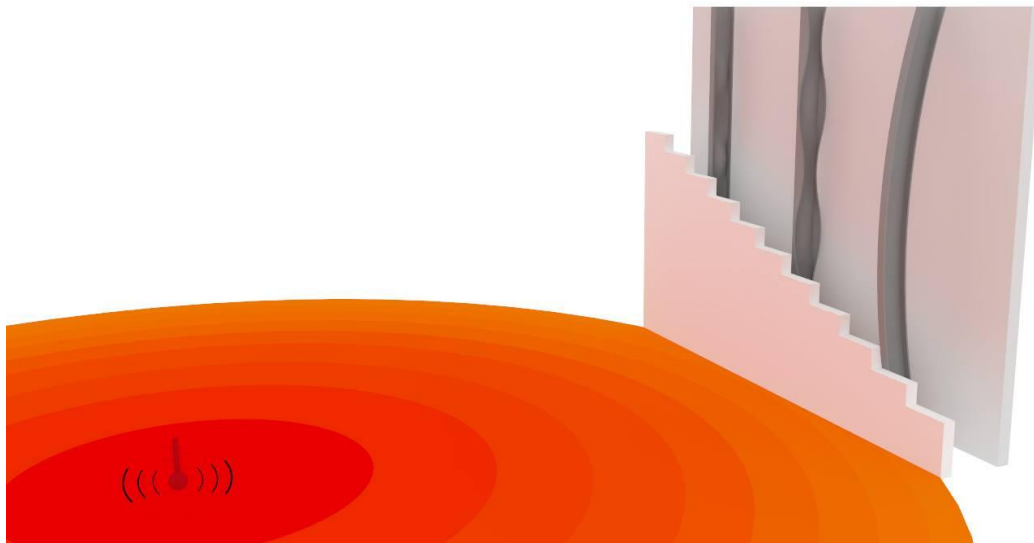# NATIONAL TECHNICAL UNIVERSITY OF ATHENS

School of Civil Engineering

Institute of Steel Structures

# Structural Behavior of Light Gauge Cold-Formed Steel Frame Walls under Fire Conditions

Postgraduate Thesis

Iason Vardakoulias

ISS PT 2015/07

Supervisor: Charis Gantes, Dr. Civil Engineer, Professor N.T.U.A.

Athens, October 2015

# NATIONAL TECHNICAL UNIVERSITY OF ATHENS

School of Civil Engineering

Institute of Steel Structures

# Structural Behavior of Light Gauge Cold-Formed Steel Frame Walls under Fire Conditions



Postgraduate Thesis

Iason Vardakoulias

ISS PT 2015/07

Supervisor: Charis Gantes, Dr. Civil Engineer, Professor N.T.U.A.
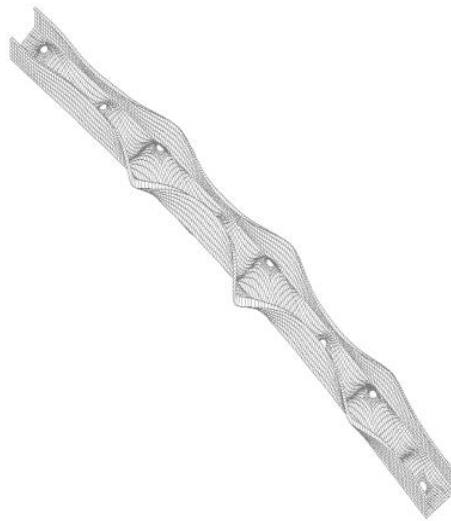
Athens, October 2015

Ιάσων Βαρδακούλιας (2015)

Συμπεριφορά λεπτότοιχων μεταλλικών φερόντων στοιχείων ψυχρής ελάσεως σε συνθήκες πυρκαγιάς
Μεταπτυχιακή Εργασία ΕΜΚ ΜΕ 2015/07
Εργαστήριο Μεταλλικών Κατασκευών, Εθνικό Μετσόβιο Πολυτεχνείο, Αθήνα.

Iason Vardakoulias (2015)

Postgraduate Thesis ISS PT 2015/07
Structural Behavior of Light Gauge Cold-Formed Steel Frame Walls under Fire Conditions
Institute of Steel Structures, National Technical University of Athens, Greece

# Acknowledgments

ΕΘΝΙΚΟ ΜΕΤΣΟΒΙΟ ΠΟΛΥΤΕΧΝΕΙΟ
ΣΧΟΛΗ ΠΟΛΙΤΙΚΩΝ ΜΗΧΑΝΙΚΩΝ
ΕΡΓΑΣΤΗΡΙΟ ΜΕΤΑΛΛΙΚΩΝ ΚΑΤΑΣΚΕΥΩΝ

ΜΕΤΑΠΤΥΧΙΑΚΗ ΕΡΓΑΣΙΑ
ΕΜΚ ΜΕ 2015/07

**Συμπεριφορά λεπτότοιχων μεταλλικών φερόντων στοιχείων ψυχρής ελάσεως
σε συνθήκες πυρκαγιάς**

**Ιάσων Βαρδακούλιας**

Επιβλέπων: Χάρης Γαντές, Δρ. Πολιτικός Μηχανικός, Καθηγητής ΕΜΠ

# ΠΕΡΙΛΗΨΗ

Η παρούσα εργασία διερευνά τη συμπεριφορά των σύγχρονων συστημάτων ξηράς δόμησης σε συνθήκες πυρκαγιάς. Τα συστήματα ξηράς δόμησης αποτελούνται συνήθως από φέροντα μεταλλικά στοιχεία ψυχρής έλασης, εξωτερική επένδυση από γυψοσανίδες ή τσιμεντοσανίδες και ενδιάμεση θερμική μόνωση από πετροβάμβακα, υαλοβάμβακα ή άλλα θερμομονωτικά υλικά. Τα πλεονεκτήματα αυτών των συστημάτων έναντι των συμβατικών μεθόδων δόμησης είναι η μεγάλη ευελιξία τους στο σχεδιασμό, η ενεργειακή αποδοτικότητα τους καθώς και η μεγάλη ταχύτητα και το μικρότερο κόστος κατασκευής. Στην παρούσα εργασία μελετήθηκαν τέσσερις παραλλαγές τέτοιων συστημάτων με μονή ή διπλή γυψοσανίδα, με ή χωρίς θερμική μόνωση. Χρησιμοποιήθηκε χάλυβας ποιότητας S320GD+Z και μέλη διατομής C με χείλη και δύο διαμήκεις νευρώσεις στον κορμό. Αερόκαρφα συνδέουν τις γυψοσανίδες με τα μεταλλικά στοιχεία, τα οποία εξασφαλίζουν παράλληλα το λυγισμό περί τον ασθενή άξονα της διατομής των στύλων. Η τυποποιημένη καμπύλη πυρκαγιάς που προβλέπεται στο πρότυπο ISO 834 επιβάλλεται στη μια όψη του τοίχου, προκειμένου να προσομοιωθούν κατάλληλα οι συνθήκες πυρκαγιάς, προκαλώντας έτσι ανομοιόμορφη κατανομή θερμοκρασίας κατά μήκος της διατομής.

Το λογισμικό ANSYS χρησιμοποιήθηκε για τον προσδιορισμό της θερμοκρασιακής κατανομής σε δισδιάστατο περιβάλλον προσομοιώνοντας ολόκληρο το σύστημα γυψοσανίδα-μόνωση-μεταλλικά στοιχεία. Οι θερμικές και μηχανικές ιδιότητες των υλικών εκφράζονται συναρτήσει της θερμοκρασίας τους, βάσει πρόσφατων ερευνητικών αποτελεσμάτων, ενώ για το χάλυβα λήφθηκαν σύμφωνα με τις προβλέψεις του Ευρωκώδικα 3, μέρος 1.2. Τα αποτελέσματα της ανάλυσης μεταφοράς θερμότητας εισήχθησαν στο πρόγραμμα πεπερασμένων στοιχείων ADINA, ώστε να καταστρωθούν οι καμπύλες απομείωσης της φέρουσας ικανότητας συναρτήσει της θερμοκρασίας ή/και του χρόνου. Το πεδίο του χρόνου χρησιμεύει για τον προσδιορισμό του δείκτη πυραντίστασης των στοιχείων και αξιοποιείται για παρατηρήσεις σε επίπεδο

σχεδιασμού. Αντιθέτως, από το πεδίο της θερμοκρασίας εξάγονται τα βασικά συμπεράσματα της στατικής συμπεριφοράς των μελών, τα οποία απορρέουν από τα ποικίλα μεγέθη θερμοκρασίας που δύναται να αξιοποιηθούν, όπως μέγιστη θερμοκρασία, μέση θερμοκρασία κτλ.

Για τον προσδιορισμό των κρίσιμων φορτίων λυγισμού στους ορθοστάτες, πραγματοποιήθηκε γραμμική ανάλυση λυγισμού στο λογισμικό πεπερασμένων στοιχείων ADINA. Τα αποτελέσματα αυτά επιβεβαιώθηκαν από αντίστοιχη γραμμική ανάλυση λυγισμού με τη μέθοδο των πεπερασμένων λωρίδων που υλοποιήθηκε στο πρόγραμμα CUFSM. Τα σχήματα των ιδιομορφών λυγισμού χρησιμοποιήθηκαν ως αρχικές γεωμετρικές ατέλειες, για την εκτέλεση μη γραμμικών αναλύσεων γεωμετρίας και υλικού (GMNIA) υπό την επίδραση αξονικού θλιπτικού φορτίου εφαρμοζόμενο στο κέντρο βάρους της αρχικής διατομής, τόσο με έλεγχο μετατόπισης όσο και με έλεγχο δύναμης. Κατά τη διαδικασία επίλυσης έγινε χρήση των αλγορίθμων Newton-Raphson και Arc-Length για επιβεβαίωση των αποτελεσμάτων. Έπειτα, τα αριθμητικά αποτελέσματα συγκρίθηκαν με τις προβλέψεις κανονιστικών μεθόδων, όπως είναι η εναλλακτική μέθοδος ¨Direct Strength¨ που προτείνει ο Αμερικάνικος κανονισμός και η μέθοδος ¨Ενεργού πλάτους¨, η οποία προτείνεται στον Ευρωκώδικα 3, μέρος 1.3, περί μελών ψυχρής ελάσεως.

Οι αναλύσεις των μεταλλικών ορθοστατών υπό συνθήκες πυρκαγιάς πραγματοποιήθηκαν τόσο για ομοιόμορφη θερμοκρασία, εντός της διατομής, όσο και για τις κατανομές θερμοκρασίας που προέκυψαν από τις αναλύσεις μεταφοράς θερμότητας των τεσσάρων συστημάτων τοίχου ξηράς δόμησης. Η θερμοκρασία κατά μήκος του μέλους θεωρήθηκε σταθερή σε όλες τις περιπτώσεις. Ο προσδιορισμός του ρυθμού απομείωσης της αντοχής έγινε με μη γραμμικές αναλύσεις GMNIA σταθερού αξονικού φορτίου και σταδιακά αυξανόμενης θερμοκρασίας (transient-state) όσο και σταθερής θερμοκρασίας και σταδιακά αυξανόμενου φορτίου (steady-state). Επιπρόσθετα, διαμορφώθηκαν διαγράμματα αλληλεπίδρασης αξονικής δύναμης-ροπής κάμψης υπό τριγωνικό και ομοιόμορφο διάγραμμα ροπής για διάφορες τιμές ομοιόμορφης θερμοκρασίας μέλους.

Τα αποτελέσματα των αριθμητικών αναλύσεων επιβεβαιώνονται με αναλυτικούς και ημι-αναλυτικούς υπολογισμούς βάσει της μεθόδου του Ευρωκώδικα 3 και της direct strength αντίστοιχα. Ο Ευρωκώδικας 3 εξετάσθηκε σύμφωνα με τη μεθοδολογία που προτείνεται στο EN 1993-1-2, όσο και μιας τροποποιημένης μεθόδου που προτείνεται στη διεθνή βιβλιογραφία και βασίζεται στο πρότυπο EN 1993-1-3 χρησιμοποιώντας όμως απομειωμένες τιμές μηχανικών ιδιοτήτων του χάλυβα για κάθε εξεταζόμενη θερμοκρασία. Ομοίως ελέγχθηκε, ως μια άλλη προσέγγιση, η εφαρμογή της μεθόδου direct strength για το σχεδιασμό μελών σε συνθήκες πυρκαγιάς με χρήση απομειωμένων τιμών μηχανικών ιδιοτήτων για κάθε στάθμη θερμοκρασίας. Τέλος, για την εξέταση της παραδοχής του Ευρωκώδικα, περί χρήσεως της μέγιστης θερμοκρασίας της διατομής σε περίπτωση ανομοιόμορφης κατανομής, συγκρίθηκαν τα αποτελέσματα των αριθμητικών αναλύσεων με ομοιόμορφη θερμοκρασία με αυτά που προέκυψαν για την ανομοιόμορφη θερμοκρασία και προέκυψαν χρήσιμα συμπεράσματα για το σχεδιασμό μεταλλικών μελών έναντι πυρκαγιάς με βάση τις αναλυτικές και ημι-αναλυτικές μεθόδους των κανονισμών.

NATIONAL TECHNICAL UNIVERSITY OF ATHENS
SCHOOL OF CIVIL ENGINEERING
INSTITUTE OF STEEL STRUCTURES

POSTGRADUATE THESIS
ISS PT 2015/07

**Structural Behavior of Light Gauge Cold-Formed Steel Frame Walls
under Fire Conditions**

**Iason Vardakoulias**

Supervisor: Charis Gantes, Dr. Civil Engineer, Professor N.T.U.A.

# ABSTRACT

This study investigates the structural behavior of modern load-bearing drywall formations under fire conditions. Drywall systems comprise load bearing cold-formed steel members sheathed in gypsum or cement boards and may additionally include thermal insulation placed in the cavities forming between the wallboards and the steel studs. These systems provide high design flexibility, energy efficiency, low cost and short installation time. Four different drywall configurations were considered with single or double plasterboards layers, with or without mineral wool as cavity insulation. The studs are made of steel S320GD+Z and have lipped channel sections with two web stiffeners. The plasterboards are attached to the studs using ballistic nails which additionally prevent minor axis buckling of the steel members. The standard ISO 834 fire curve is imposed at the inner wall face in order to simulate the fire conditions and non-uniform temperature distribution which is expected to occur across the member.

ANSYS CFX is used in a 2D finite element environment to derive proper temperature profiles across the investigated sections by modeling the whole plasterboard-insulation-stud system. For each material, temperature dependent thermal and mechanical property models are incorporated. Specifically, Eurocode 3 part 1.2 is utilized for the diminishing properties of steel and state of the art models proposed by recent researches are considered for the plasterboards and the mineral wool. The results of the thermal analysis were used to feed the finite element software ADINA in order to generate diminishing curves corresponding to bearing capacity deterioration as a function of time and/or temperature. Results in time domains are used to present a solution regarding the fire resistance rating of the four drywall assemblies considered. On the other hand, temperature domains are employed to display and compare the structural performance of the specimens in terms of various temperature aspects, such as maximum cross-sectional temperature, average temperature etc.

The finite element method is utilized by ADINA to perform linearized buckling analysis in order to determine the elastic buckling loads of the studs. These results are cross-validated using the freely available software CUFSM that incorporates the finite strip method in its solution process. Mesh refinements were examined in both programs in order to extrapolate the most efficient solutions in terms of both precision and computational effort. The shapes of the elastic buckling modes were used as initial geometric imperfections during the execution of geometric and material non-linear analyses with initial geometric imperfections in order to determine the most unfavorable mode-imperfection combination at ambient temperature conditions. In each case, the stud was strained by a vertical concentric compressive action, placed at the gravity center of the gross cross-section, under both load-control and displacement-control situations; Newton-Raphson and Arc-Length solution processes were performed in order to verify the corresponding results. The numerical results were compared to the predictions of AISI's direct strength method and the effective width method, executed according to the provisions of EN 1993-1-3.

The most unfavorable mode combination, comprising local and distortional buckling modes, was used to carry out the non-linear analyses at elevated temperatures. Uniform and non-uniform temperature profiles were considered across the member while the temperature distribution along the stud was considered constant. The temperature gradient was extracted by the heat transfer analyses for each of the four cases and non-linear analyses were performed to identify load-bearing capacity deterioration as a function of time and temperature. Load ratio reduction curves were determined using both steady state and transient state conditions which are supposed to produce identical solutions. Additionally, the results of the steady state are employed to construct equilibrium paths. Apart from merely imposing an axial load, an external bending moment is introduced to produce uniform and triangular moment distributions in order to create axial force-bending moment interaction diagrams under uniform temperature profiles.

The numerical investigation was followed by analytical and semi-analytical calculations relying on the provisions of the direct strength method and Eurocode 3. Regarding Eurocode 3, the official EN 1993-1-2 method was examined along with a modified EN 1993-1-3 solution process that was widely used by various literature sources. The modified method employs the equations of Eurocode 3, part 1.3 using the diminished values of elasticity modulus and yield stress at each considered temperature. CUFSM's solution process was executed with reduced elasticity modulus values to reflect the lesser behavior corresponding to higher temperatures; its results fed the direct strength method along with diminished yield stress values to represent the behavior at each temperature. These solutions were compared to the numerical results to investigate the prediction accuracy of the pertinent regulations. Finally, the results of the uniform temperature distribution were compared to the non-uniform profiles to provide significantly important information regarding the claim of Eurocode 3, part 1.2 to use the maximum cross-sectional temperature if a temperature gradient is applied across the members.

# Table of Contents

# 1  Theoretical Background

## 1.1  General Remarks

Carbon steel sections comprise two big families of structural members; the more popular and frequently used members deriving from hot-rolling and the less familiar but of growing importance cold-formed members. Hot-rolled sections have been excessively utilized for more than a century; however, cold-formed members' popularity escalated only after the 1950s. This lack of confidence in cold-formed members resulted from their inherent tendency to respond non-linear when exposed to load-bearing conditions. However, the release of the first publication concerning the design of cold-formed sections by the American Iron and Steel Institute in 1946 signaled the acceleration of the acceptance rate of such structural members by the civil engineering community.

The advantages of cold-formed members enabled their use in a variety of constructions. Single or double storey buildings can comprise the sole use of cold-formed members whereas multi storey or high-rise constructions employ hot-rolled members for the main frames and cold-formed sections for the secondary or auxiliary elements. Another popular application of cold-formed sections concerns the formation of light gauge steel assemblies. Light steel formations include wall and floor systems and are widely supplied to cover industrial and residential building demands. These assemblies employ cold-formed thin-walled sections, usually C (channel) or Z-sections, as load-bearing members lined by a variety of different possible materials. Identifying the thermal performance of steel framed walls is the subject of this study.

The rise of light gauge steel frame wall (LSF) systems has clarified the necessity to be accompanied by a proper fire safety issuance even though fire safety was not always a dominant factor in designing steel constructions. Nevertheless, fire hazard has been gaining ground following the loss of human lives and property damages accumulating during the last decades. Furthermore, the foundation of fire safety engineering increased the efficiency of fire safety mechanisms in terms of both performance and cost reduction establishing a decent return on investment for construction companies after incorporating fire safety aspects in prospective structures.

The exposure of cold-formed thin-walled members to fire situations is followed by rapid cross-sectional temperature escalation. Plasterboard linings are usually used to clad the structural elements in order to mitigate strength and stiffness reduction caused by temperature amplification through hindering heat transfer from the fire source to the ambient wall side. These usual load-bearing wall systems, that incorporate cold-formed sections sheathed in plasterboard layers, often employ composite materials as insulation to fill the air cavities formed by the plasterboards and the steel elements or utilize a more modern approach [1] suggesting the use of insulation sandwiched between double plasterboard layers at each wall face.

## 1.2   Cold-Formed Steel Members

The main considerations regarding cold-formed members derive from their thinness and manufacturing processes. Compared to hot-rolled members, thin-walled sections may have one order of magnitude less nominal thickness, ranging from 0.378 to 25.4mm, resulting in local instabilities [2], [3]. Triggering these instabilities rarely leads to instant failure, reflecting the strength of the postbuckling regime, but rather reduces stiffness; a fact scarcely influencing the behavior of hot-rolled members. Furthermore, the manufacturing process alters the homogeneity of steel properties across the section adding peculiar residual stress distributions that have to be considered in pertinent studies to avoid bearing capacity overestimation. In addition, cold-formed members can be very sensitive to imperfections caused during fabrication or handling resulting in a necessity to include them in the numerical models.

### 1.2.1   Manufacturing processes

The standardization following the fabrication of hot-rolled members is negligible in the industry of cold-forming. Hence, while companies associated with hot-rolling create cross-sectional shapes with identical dimensions according to the provisions of pertinent regulations, cold-forming companies can manufacture different sections in an attempt to compete against each other. This fact arises from the convenient production of thin-walled members. Hot-rolled structural elements involve significant financial investments in heavy machinery, auxiliary equipment and production lines. On the other hand, all it takes for a thin-walled member to be created is bending a flat sheet into a specific shape; an operation that could literally be home-made. As a result, it's extremely easy for manufacturing companies to put a lump here and there and rearrange the equipment to produce different geometries or add stiffeners in the plane parts.

Two main methods are used to produce cold-formed members: i) roll forming and ii) brake operation. Roll forming is the most popular manufacturing process while at the same time allows more automation to take place. Its use is beneficial when high production rates are required, especially if accompanied by identical cross-sectional shapes, resulting from the high tooling but low labor cost. On the other hand, brake operation can be efficient in low-volume and geometrically diversified production while limitations arise from the difficulty to produce lengths higher than 6-7m [4].

Roll forming equipment is fed by continuous steels strip and consists of a set of opposing rolls that progressively deform the inserted strip into the desired geometry. Each pair of rolls is called a station and imposes an ad hoc specified plastic deformation (Figure 1-1). The whole operation is performed at room temperature and the set up can take several days. Simple sections can be produced by up to 6 roll sets while most complicated shapes require the use of up to 15 series of rolls. The rolling speed falls in the range of 6 to 92m/min, with an average range of 23 to 46m/min, and the cutoff lengths are usually 6 to 12m [2]. The resulting thicknesses of carbon steels can be as high as 19mm while stainless steels have been produced with thicknesses ranging from 0.2 to 7.6mm [5].
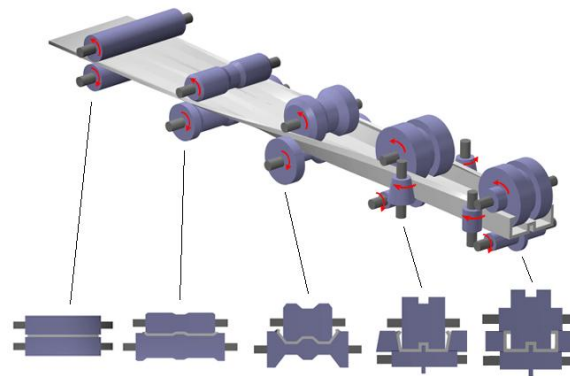
Figure 1-1: Roll forming process [6]

Brake forming operation involves a movable top beam (punch) and a fixed bottom layer. The bottom layer consists of a cavity that matches either a lump on the upper beam or the gross geometry of the movable beam (Figure 1-2). The steel sheet is placed between those two in order to perform the brake operation and create the desired shape. To form different sections differentiated dies are placed in the cavity of the bottom bed and produce the required geometries. Brake forming exhibits limitations regarding cross-sectional dimensions and production capacity thus requiring [7]: i) simplified section configuration, ii) production rates for linear members lower than 91.5m/min and iii) wide sections, i.e. usually more than 457mm.
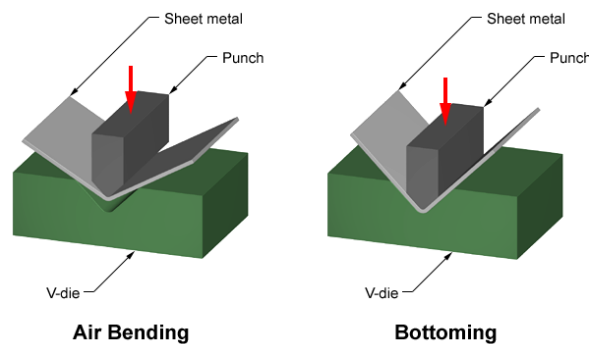


Figure 1-2: Brake forming operation [8]

### 1.2.2 Advantages and applications

The nature of cold-forming process allows the creation of variously differentiated cross-sectional geometries easily and boosts the innovation of new and more efficient element shapes. The application of cold-formed members ranges from residential to industrial and agricultural buildings; it also includes temporary constructions like scaffolds, hovels and load-bearing frames. When it comes to structural elements, cold-formed members are grouped into two categories, i) structural framing members and ii) panels and decks. Structural framing members can be used to form space frames, arches, joist, storage rack sections, purlins etc. using various section profiles likes the ones depicted in Figure 1-3. Pre-fabricated walls incorporate load-bearing cold-formed elements as studs and tracks whilst corrugated sheets are employed to fabricate plates and decks. Steel panels and decks additionally provide working surfaces, electrical conduits, acoustic/heat insulation if filled with proper materials, and section perforations combined with panel cells are useful as heating and air-conditioning ducts.
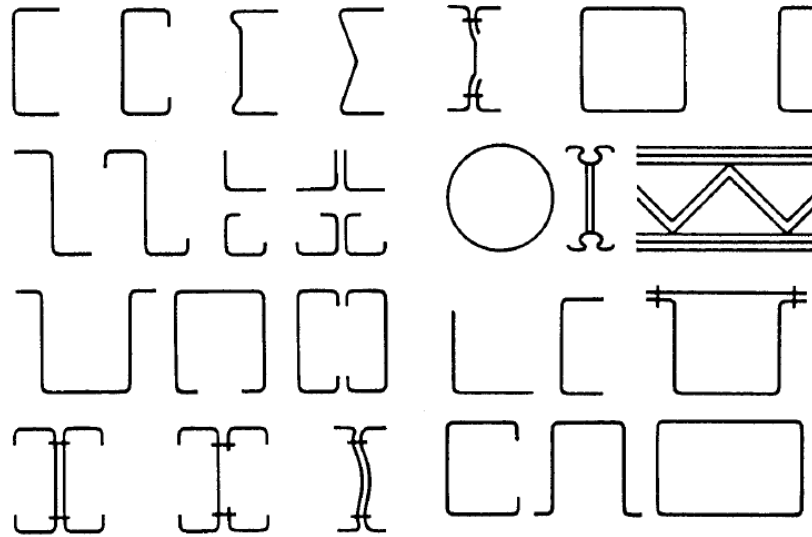
Figure 1-3: Typical cold-formed sections [9]

Comparing cold-formed steel structural elements to members composed by other materials such as timber, concrete and hot-rolled structural steel, the following advantages can be realized [7]:

> *Lightness*, cold-formed members achieve high strength/stiffness to weight ratios and their lightness facilitates transportation and handling.

> *Manufacturing*, the manufacturing process allows for mass and relatively flexible production while providing economical transportation and handling costs.

> *Prefabrication*, the ability to fabricate members at the factory and not at the construction site enhances detailing quality; annihilates efficiency ambiguities related to poor quality labor work; reduces erection time while assuaging installation difficulties.

> *Installation*, weather-free erection/installation operations not accompanied by formwork necessity.

> *Material*, regarding comparisons with timber or concrete, cold-formed steel members exhibit no creep/shrinking at ambient temperature; they are incombustible, termite and rot proof; provide substantial uniformity and can be recycled; present lower long-term and maintenance expenses.

These reasons equip cold-formed constructions with very high financial competitiveness. The former limitation for constructing multi-storey buildings solely from cold-formed members has now been waived. Light gauge steel framing-oriented construction companies have achieved to deliver competitive prices for commercial buildings up to 16 stories [10] in an attempt to alleviate this market segment from the dominating wood and concrete structures. At the same time, the significantly low steel prices experienced after the initiation of the great recession in 2007 have stabilized and an incremental growth rate is expected to characterize the world steel industry, starting in 2015 [11]. Ongoing inquiries of the Thompson Research Group have verified the increase in production/revenues of cold-formed steel manufacturing-oriented companies in this year's first half so far, only to enhance the promising predictions for the years to come [12].

### 1.2.3    Light gauge steel frames

Light gauge steel frames (LSF) utilize cold-formed thin-walled sections usually centered at small distances. Their application includes both floors and walls, with the latter being the subject of this clause. LSF walls comprise horizontal and vertical members known as tracks and studs, respectively (Figure 1-4). In most cases, channel sections are used as studs both in curtain wall systems and load-bearing walls. Knockouts (holes at the web at regular intervals) frequently appear as they provide a convenient means to accommodate electrical conduits, pipes and mechanical equipment. U-sections are typically used as tracks in order to secure the vertical elements or prevent excessive deflections. Both interior and exterior wall formations are manufactured using steel as the load-bearing material. For this reason, steel members are delivered with a galvanized coating that provides resistance against corrosion.

Although steel is classified as non-combustible material its exposure to high temperatures can cause rapid reduction of its bearing capacity. Thus, cladding is required to secure the steel elements against fire. Gypsum plasterboards are usually employed to provide fire protection due to the high moisture content of gypsum. In the air cavities formed between the plasterboards and the studs, an infill material is placed to provide heat or sound insulation. Single or double plasterboard layers can be used in either face of the wall, while insulation materials can be placed between these layers and not in the air cavities. This configuration, i.e. externally insulated walls, was proposed after scientific evidence suggesting that cavity insulation has a negative impact on the thermal performance of LSF walls came to see the light. Nevertheless, contradictive results are continuously published regarding the matter of cavity insulation on the structural response at elevated temperatures with no solidifying conclusion being available to date.
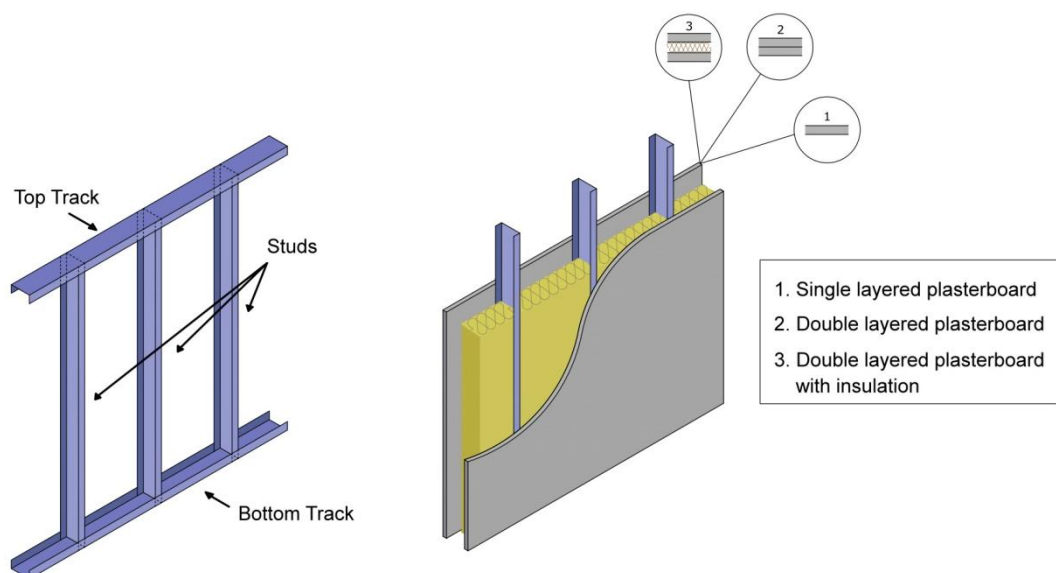


Figure 1-4: Typical light gauge steel frame wall

It shall be noted that, in most cases, LSF walls' critical limit state is the serviceability, predominated by the requirement to limit the lateral deflections of the corresponding studs. Hence, exploiting high strength steel is generally not efficient since studs are centered at narrow

intervals and their axial loads are small. Transverse displacements are mostly influenced by the relevant stiffness of the stud which in turn is a function of its dimensions and elasticity modulus; since elasticity modulus is considered constant among different steels and the cross-sectional dimensions are decided a priori, the mean distance between the studs is the critical design factor. Moreover, providing the studs with bridging can substantially increase the available stiffness thus reducing relevant deflections even more. Bridging is achieved by connecting the studs with additional horizontal beams passing through the knockouts and includes three main types: i) space bars, ii) U-channels, iii) block and strap bridging. If successfully implemented, bridging secures the vertical alignment of the studs and prevents weak axis buckling.



(a) Space bars                    (b) U-channels                    (c) Block and strap
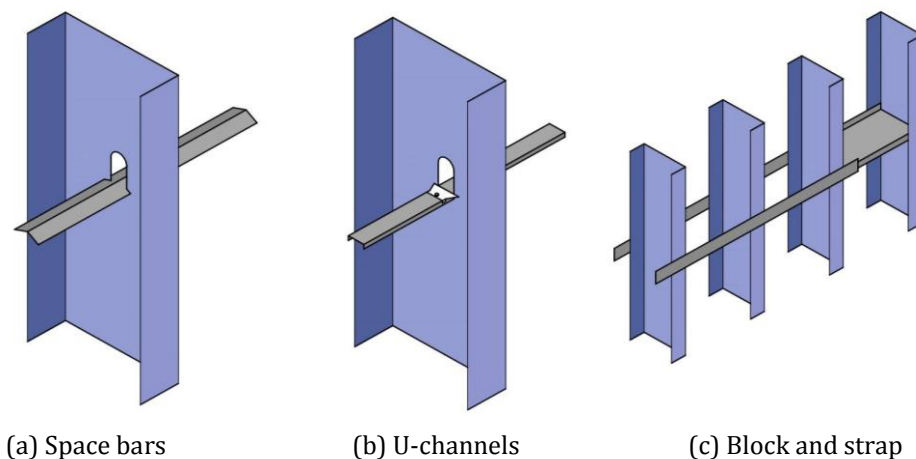
Figure 1-5: Bridging types

LSF walls can also contribute to the reduction of the lateral deflections occurring at heavy steel frame constructions. Depending on geometry, loading and floor assemblies e.g. joists, corrugated sheets, floor material etc., various exterior deflection systems can be utilized to provide additional lateral stiffness. Each type is recommended for different stress intensities and incorporates various aspects that establish its competitiveness with respect to the other available systems. The most popular systems are [13]:

i. *Slide clip connectors*, can accommodate imperfect perimeter angles; cheap equipment but increased labor costs

ii. *Strut connectors*, used when perimeter angles are not provided at the top of the slab

iii. *Top clip connectors*, used in connections applied between floors or at the top of window jambs

iv. *Vertical clip connectors*, attached directly to the slab to prevent loading of the bottom flange of the beam when this is necessary

v. *Spacing bar assemblies*, effective in assemblies installed between floor decks; may not be allowed in areas with potential high seismic hazard due to lack of mechanical fasteners

vi. *Double track assemblies*, doesn't require bridging; can't be used in axially loaded studs

vii. *Slotted slip tracks*, easiest installation and high design loads; provide mechanical attachment, ideal for seismic regions; does not work in inclined end wall conditions

### 1.2.4 Special design considerations

Using thinner elements and cold-formed manufacturing processes causes unusual structural behavior; a one not encountered when dealing with hot-rolled sections. Different constitutive material laws apply to cold-formed members compared to hot-rolled elements. Behavior can prove to be far more bewildering when material non-linearity interacts with geometric non-linearity, i.e. buckling effects that take place in segments under compression. Failure pattern unraveling can be significantly affected by residual stresses and yield stress non-uniform distribution resulting from the manufacturing process. The final response reflects all these interactions combined with the postbuckling regime that differentiates with respect to the section's geometry and the applied load.

#### 1.2.4.1 Buckling

Buckling is the phenomenon associated with sudden displacement increase for small increase in the applied load. Lateral deflections become large enough to defuse the principal of superposition and the constitutive relationships between stresses and strains have to be reformed, considering the deformed shape of the member. Elastic buckling introduces two alternative equilibrium states that characterize structural members: straight and buckled. Each buckled shape of thin-walled sections can reflect three relevant types of elastic buckling modes: local, distortional and global. Moreover, members susceptible to buckling exhibit two types of response associated with each buckling type: bifurcation and snap through.

In bifurcation buckling, the system responses linearly to the imposed load and at a certain level the equilibrium path bifurcates followed by a steady, neutral or unsteady state. The first or primary path reflects the behavior up to the bifurcation point whereas the secondary path introduces the postbuckling response. Steady secondary path means that the member has still some reserves and that ultimate load has yet to be reached; failing to identify such a postbuckling regime might result in underestimating the bearing capacity. Neutral or unsteady secondary paths are more dangerous because they might cause excessively high deformations even leading to sudden collapse. On the other hand, snap through buckling corresponds to structural behaviors where when a specific point is reached the member suddenly toggles, by substantially escalating its deflection. Snap through buckling can appear in two forms: postbuckled/bifurcated snap through or limit point snap through [14]. The equilibrium paths expressing the response for each buckling type, by performing load or displacement control, are depicted in the next figure.
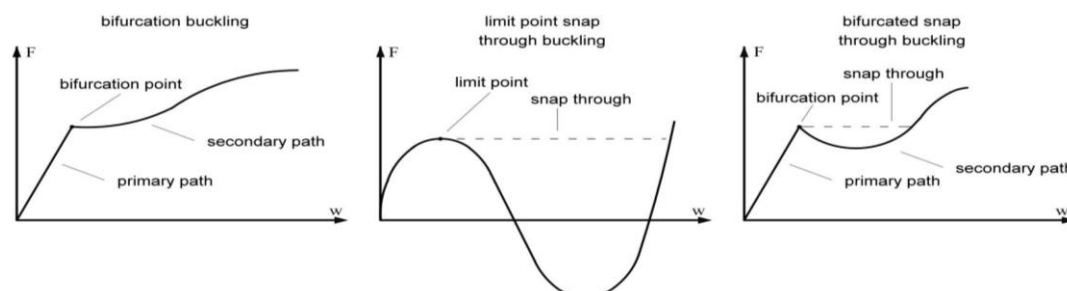


Figure 1-6: Buckling response types

Local buckling corresponds to a buckling mode that involves major distortion of the section; however, this distortion comprises only rotation at the fold lines, and not translation [15]. The distortioned part of the cross-section, usually the web due to its relatively higher depth, can buckle at half-wavelengths lower than the maximum width of the plates that form the cross-section. The use of intermediate stiffeners can mitigate local buckling-oriented failure because local buckling is explicitly affected by width to thickness ratio. Stiffeners can reduce the potential buckling length of a plate, thus triggering higher local buckling modes that occur at increased elastic critical loads.

Distortional buckling is evident at intermediate half-wavelengths, in the range between local and global buckling. Contrary to local buckling, distortional buckling causes both rotation and translation at web/flange junctures of a cross-section [16]. Normally, an element will exhibit distortion, usually the web, while the other elements will respond as rigid bodies. Distortional buckling has proved to be more severe than local buckling as its susceptibility to imperfection amplitudes is higher while its postbuckling strength is lower. Distortional buckling may not present a minima corresponding to a specific half-wavelength; it is even possible for some cross-sections to not exhibit distortional buckling modes at all.

Global (Euler) buckling might present as flexural, torsional or flexural-torsional in steel columns or as lateral-torsional in beams bending about their strong axis. Global buckling critical elastic load (minima), corresponding to the first global mode, presents at a half-wavelength equal to the column's length, for a concentrically compressed column. Members will usually exhibit weak axis buckling unless lateral restraints hinder it, thus leading to higher minor axis modes or even better to strong axis bending. In addition to flexural buckling, cold-formed members are often thin and single symmetric; their shear center does not coincide with the gravity center and their torsional rigidity is small (torsional rigidity is proportional to $t^3$); hence, torsional-flexural buckling is usually the case when global buckling contributes significantly to the structural response.

### 1.2.4.2    Material non-linearity

Two general constitutive stress-strain laws apply to structural steel members [17], the sharp-yielding type and the gradual-yielding type (Figure 1-7). Steel elements manufactured using hot-rolling processes usually follow the sharp-yielding stress-strain relationship. Their yield point is determined by the stress level of the plateau occurring right after the proportional limit $f_{pr}$ is breached. For cold-worked steel the behavior matches more with gradual-yielding law. After the proportional limit is reached, the curve displays a "knee" and the tangent modulus $E_t$ gradually decreases to reach the tensile stress level. The shift from sharp to gradual yielding is mainly the result of strain hardening and cold-reducing; a technique applied to sections in order to reduce their thickness and can also be accompanied by annealing, namely heating the steel to a high temperature to reinstate its softness and formability [18]. The derivation of the design yield stress follows a more dubious process which is approached by two methods [7].
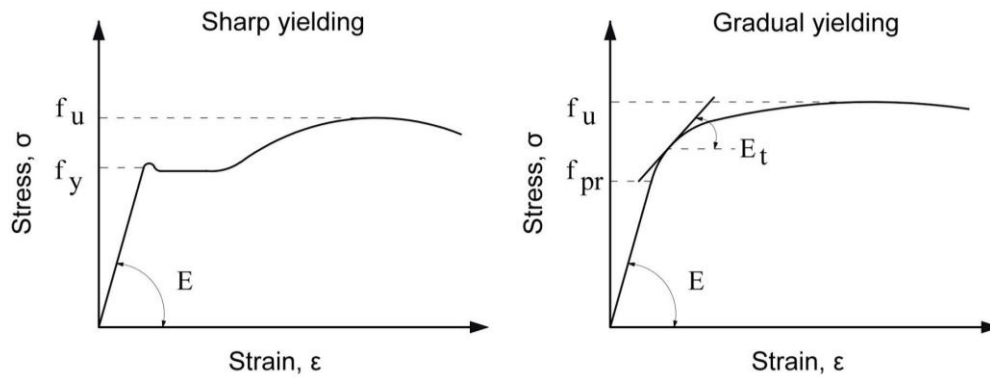
Figure 1-7: Constitutive stress-strain laws for steel sections

The first, called the offset method, assumes a line parallel to the linear path offset by a specific strain value, usually 0.2%; the intersection of this line with the original curve defines the yield point. The second, called the strain-underload method, defines the yield point as the stress that corresponds to a specific elongation value, usually 0.5% [4]. Furthermore, while the elasticity modulus can accurately characterize the behavior of hot-rolled members up to the yield point the tangent modulus is a more precise measurement when it comes to cold-formed members. The tangent modulus equals the elasticity modulus until the proportional limit but its incremental decrease causes gradually escalating deformations to occur for augmentative stress variations. Since the buckling response of sections is affected by both the yield stress and the modulus of elasticity or the tangent modulus, special attention must be given to the selection of the appropriate values relevant to those mechanical properties.

The cold-working process influences the mechanical properties of steel by adding inhomogeneous aspects to the cross-sectional properties. These effects might prove to be substantially different for the final section compared to the initial sheet, strip or plate before forming [19]. Usually, cold-formed members experience higher yield and ultimate stress points while at the same time display reduced ductility. Properties at the corners can be significantly differentiated than those corresponding to the center part of the plated elements as most cold-working is performed at the corners. Hence, yielding generally initiates in the middle parts of the web or flanges and spreads gradually towards the fold lines.

Various researches [19], [20], [21] have examined the non-uniform section properties of steel, concentrated at the corners and the adjacent flat parts. They concluded that the effects of strain hardening and strain aging are the main contributors to the unequal properties between the cold-formed product and the virgin material. Strain hardening refers to the necessity of imposing additional stress in order to achieve progressively further deformation. Strain aging is achieved by allowing the steel to remain idle either at ambient temperatures for several weeks or at elevated temperatures for shorter time periods.

When steel alloys are strained beneath their yield point there is a change in the crystalline atomic formation of steel. This is the result of plastic deformation caused by crystalline lattice defects,

known as dislocations. When two adjacent atom planes slide with respect to each other for the first time, thus causing permanent change in the crystalline formation, they mark the initiation of yielding at a monocrystalline material. In polycrystalline materials, each crystal consists of different dislocations whose motion initiates by different shear stress direction compared to the other crystals. Yielding starts from the weaker crystals and gradually spreads and to the stronger ones [22].

Strain hardening range marks the area between the horizontal plateau and the ultimate stress. It is the result of dislocation accumulation near the grain boundaries of the crystalline material that works either as self-destruction mechanism or as motion obstacle for the dislocations. In any case, dislocation movement is temporary impeded, hence requiring additional stress to cause more deformation; thus explaining the strain hardening mechanism. Cold-working increases dislocation density, i.e. decreases the mean distance between different dislocations, allowing for dislocations to block one another. This effect increases strength at the cost of ductility deterioration.

If a steel product is loaded to reach the strain hardening area (Figure 1-8), unloaded, and then immediately reloaded, an increase in proportional limit will occur while ductility is going to diminish. The material will continue its path to fracture, following the path of the virgin material beyond the unload point (Curve *C*) and the new curve has transformed from sharp yielding to gradual yielding type in most cases [21]. If some aging intervenes before unloading and reloading, the proportional limit, yield stress and ultimate stress display higher values and the constitutive model gradually restores to match the sharp yielding law (Curve *D*). These conclusions apply for test specimens of mild steel accompanied by different techniques for eliminating oxygen from the molten steel; see pertinent reference for more information about the assumptions of the presented observations.
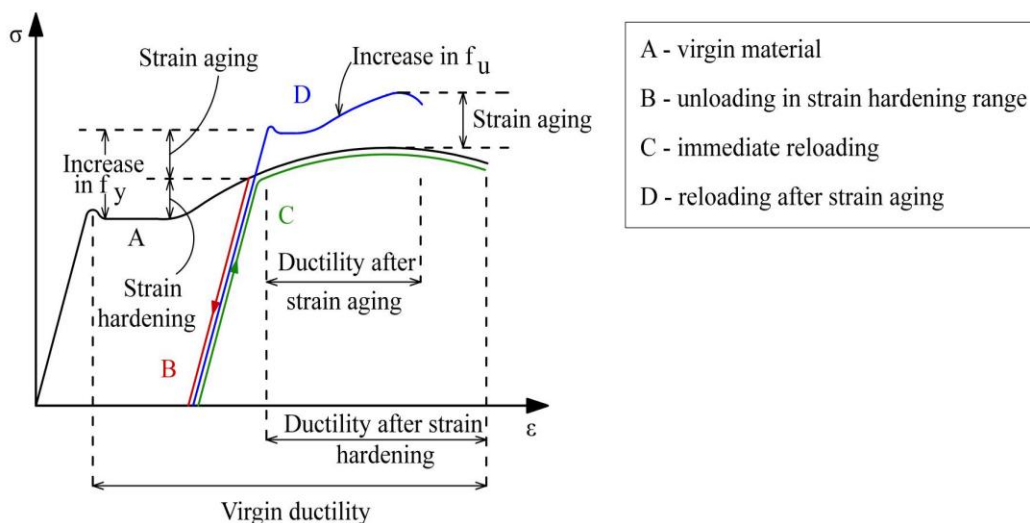


Figure 1-8: Effects of strain hardening and strain aging on stress-strain relationships [21]

Another interesting effect of cold-forming is the addition of anisotropic aspects in stretched steel sheets caused by the Bauschinger effect. [23]Assume a sharp yielding curve corresponding to the constitutive material law. If such a material is strained until the end of the plateau ($\sigma = +f_y$) and then unloaded until reaching $\sigma = -f_y$, the bump existing at the end of the linear path will transform into a smooth curve that marks the transition from the elastic to the inelastic range by gradually reducing the effective stiffness (Figure 1-9a). If the same procedure applies but the member is strained in the strain hardening range, then both the yielding plateau and the former strain hardening response are replaced by bilinear response paths with a smooth transition curve at the juncture of the two paths (Figure 1-9b). This phenomenon is called the Bauschinger effect for sections strained "before" or "in" the strain hardening range and is graphically displayed in the next figure.
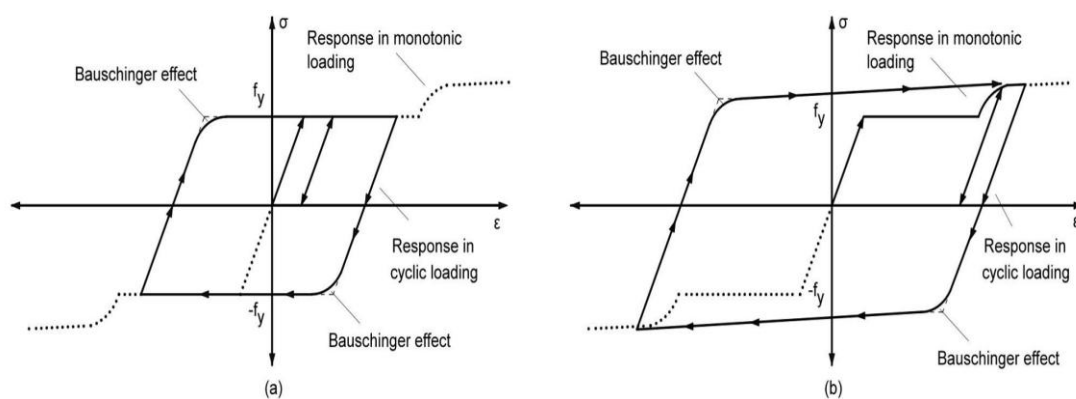


Figure 1-9: Bauschinger effect for cyclic load applied (a) before or (b) in the strain hardening range [23]

In the test specimens examined in reference [21], Bauschinger effect manifestations appeared in both directions of the investigated section. Specimens including hot-rolled sheets or annealed cold-rolled sheets were exposed to cold-stretching, i.e. tensioned in the longitudinal direction in room temperature. By the end of the stretching procedure the Bauschinger effect was evident in the longitudinal direction whereas an inverse Bauschinger effect took place in the transverse direction. The longitudinal specimens showed higher resistance to tension than compression while the transverse specimens exhibited higher resistance to compression than tension; both specimens demonstrated gradual yielding behaviors[1]. The effect of pre-tension in the longitudinal direction has increased the tensional strength of the steel sheets while the compression occurring due to shrinkage in the transverse direction has lead to an escalation in the corresponding transverse compressive strength compared to the tension resistance.

The information provided hereinbefore concerns the amount of cold-working performed in a cross-section. One can understand that since most working takes place at the fold lines, in order to create the required cross-sectional shape, corners present higher yield and tensile stress but reduced ductility than the virgin material behavior which mostly governs the middle area of the

---

[1] some steel specimens acquired through different manufacturing processes deviated from this effect; for more information visit the original study website available at:
http://scholarsmine.mst.edu/cgi/viewcontent.cgi?article=1169&context=ccfss-library

plane elements. Yield strength incremental increase is higher proportionally to tensile stress rise, thus the gap between them decays as more cold-working is carried out. Yield stress can be almost doubled near corners whereas tensile stress can present rises near 50% (Figure 1-10). Close-formed solutions are also available to derive the precise values with respect to the amount of cold-working. High ultimate to yield stress ratios of the virgin material allow for more cold-work to take place since there is greater available ductility to diminish. On the other hand, when small corner radiuses to thicknesses ratios are required, a greater amount of cold-work has to be applied. Hence, the axial resistance is amplified and the strength differential across the section is intensified.
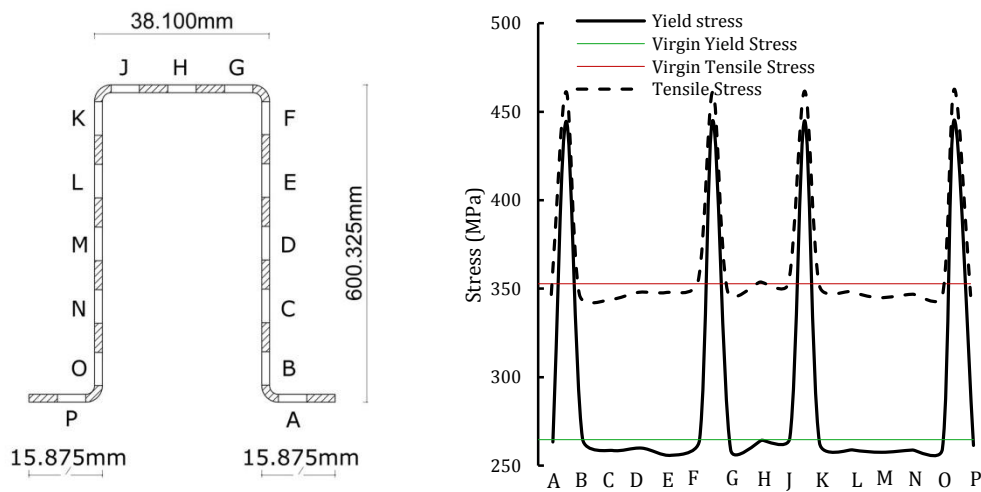


Figure 1-10: Yield and tensile stress variation across the section [21]

### 1.2.4.3   Residual stresses

Residual stresses are stresses created by manufacturing or handling processes. For hot-rolled members, residual stress distribution is usually considered to be uniform across the element thickness following the assumption that residual stress creation is the result of uneven cooling of the molten alloy. However, in cold-formed sections, residual stresses can have significant variation across the thickness resulting from the operation of cold-forming [24]. Furthermore, residual stresses may arise due to coiling and uncoiling, that is before the application of cold-working. Residual stresses can cause premature yielding by reducing the proportional limit while impeding stiffness from reaching its nominal value [25]. Their inclusion in numerical simulations is cumbersome while their amplitudes remain uncertain. As a result, residual stresses are generally excluded from the models or more conservative stress-strain laws are incorporated to account for their impacts implicitly.

Residual stress distribution generally comprises the summation of two idealized sub-types: flexural and membrane; incorporation of both can lead to feasible models of prediction when it comes to through-thickness stress variation [26]. Although real tests [27], [28] demonstrated more complex variations, measuring residual stresses is not easy particularly around corners, even though residual stresses mostly affect corner behavior. Membrane residual stresses regard

uniform distributed compressive stresses mainly aggregated around the corners. They are more prevalent in roll-formed than press-braked sections and cause rapid reduction in compressive resistance; however, their contribution is relatively small, less than 10% of initial yield stress. Flexural residual stresses have a linear distribution across the element thickness identical to elastic bending stress distribution shape while their existence dominates the response, especially around corners. Flexural residual stresses initiate premature yielding in the section's faces with amplitudes exceeding 50% of the nominal yield stress. However, the importance of residual stresses underlined in reference [26] does not agree with the investigations conducted at the University of Sydney regarding plain and lipped channel sections [29], [30].

Residual stresses are not easily incorporated in numerical analyses mainly due to the uncertainties surrounding their amplitudes. Past investigations in this matter suggest the use of residual stresses as initial conditions with respect to the element type. Types include corners, lips, stiffened or unstiffened parts. If the lip depth is relatively small, corner values can be conservatively input at the lips as well. The highest residual stresses are observed around the fold lines, i.e. at the junctures between different parts, and on edge-stiffened elements like webs. A typical flexural residual stress distribution is depicted in Figure 1-11. In order to provide more accurate computational models, residual stresses should not be included without additionally considering the effects of cold-work on the mechanical properties of steel. The interaction that takes place between residual stresses and yield stress variation, sometimes counteracting the effects of one another, is an interesting aspect that becomes increasingly popular.
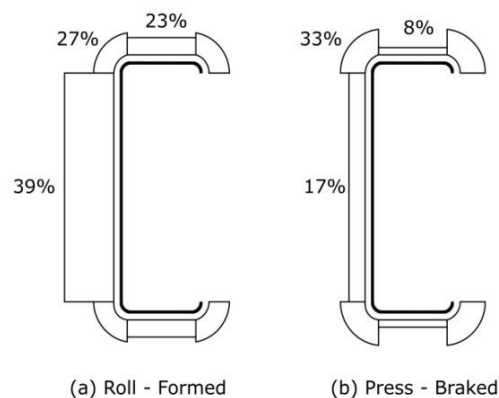


Figure 1-11: Average bending residual stress as %$f_y$ with respect to manufacturing process [26]

### 1.2.4.4    Imperfections

Real members can hardly be classified as "perfect"; imperfections arise from boundary condition defects, geometry or cross-sectional deviations from the nominal shape, load distribution and residual stresses and/or yield stress non-uniform distribution across the section [31]. Cold-formed thin-walled members are particularly susceptible to imperfections according to the buckling modes of the member under investigation. The use of initial geometric imperfections corresponding to global or local defects is vital for the proper estimation of the bearing capacity of a load-bearing member.

Finite element analysis has proved to provide accurate results of the buckling modes and their influence on the member's strength. After performing linearized buckling analysis, one can obtain the elastic buckling loads corresponding to various modes. Local, distortional and global modes are usually evident in every thin-walled member, unless lateral constraints are utilized to prevent some modes to develop. The modes with the lesser elastic buckling loads of each buckling type are usually the most critical and their contribution to the structural response is substantial. Modes corresponding to different buckling types may display different susceptibility to imperfection amplitude variation with local modes generally being the most insusceptible. Selecting the modes with the most unfavorable effect is not an easy task as there is no close-formed process that determines them, although many researchers have attempted to present proper identification methods [31], [32].

In addition, choosing proper amplitudes for each mode is extremely important as it yields highly differentiated results. Reference [26] presents maybe the most fundamental study regarding the matter of choosing imperfection amplitudes. Different values correspond to local web or flange buckling and global buckling. These values are in general consistent with the geometric tolerances proposed by EN 1090-2 [33]. Eurocode 3 presents values for local and global imperfections in the relevant parts, parts 1.1 for global bow defects and 1.5 for local plate flaws. It also presents how different modes can be combined after adjusting their initial imperfection amplitudes to realistic values. The regulation does not suggest the modes which should be incorporated in the model; however, special attention should be given at the process of combining buckling modes. Since buckling modes reflect eigenmodes, which in turn comprise eigenvectors in ad hoc degrees of freedom, adding buckling modes is practically a sum of eigenvectors that may yield favorable or unfavorable results as well.

It is important to note that the actual response during an imposed load will not be perfectly consistent with any of the facts discussed in clause 1.2.3 independently; instead, it shall incorporate data from all of them. These phenomena will interact with one another intervening in the smooth ideal responses of the individual paths of each effect only to produce sharper equilibrium paths. Initially, the response is likely to follow a path caused by a specific failure mechanism, e.g. local buckling. Then, other failure mechanisms might be triggered in some parts of the section, e.g. Euler buckling or yielding, causing a deviation from the starting response. The member will try to find a new state of static equilibrium considering all the failure mechanisms that affect the response. This process reflects the difficulty in predicting the structural behavior of sections vulnerable against material and geometric non-linearities. A thorough investigation is necessary to demonstrate the most unfavorable combination of factors influencing the behavior; nevertheless, inclusion of unfavorable factors should be performed meticulously to prevent overconservative outputs.

## 1.3   Elevated Temperature Impacts

Elevated temperature adversely affects all construction materials either combustible or incombustible. When a material is classified as combustible, it means that it contributes to the intensity and spread of the fire. However, even in non-combustible materials, property deterioration varies significantly when they are exposed to high temperature conditions. Fireproof materials are usually incorporated to clad materials more prone to deterioration due to fire situations. Since light gauge steel frame walls are typically constituted by several materials, understanding their properties' variation with respect to temperature is crucial in order to consider appropriate values to carry out pertinent simulations.

### 1.3.1   Gypsum plasterboard

When referring to gypsum plasterboards or drywalls we basically describe paper (or fiberglass) faces filled with gypsum core [34]; usually additives like vermiculite are also involved depending on the manufacturer. Dry gypsum contains around 3% by weight free water, although this percentage is affected by ambient temperature and humidity [35], [36], and 21% by weight chemically combined water [37]. By the time the temperature of the exposed drywall face exceeds approximately 80°C a dehydration process is initiated following water evaporation that continues until about 200°C [38]; this process is called "calcination". During temperature rise from 80°C to 200°C the unexposed side presents a temperature plateau known as the "time delay". At 300°C the paper clad will have completely burn out and will not provide sufficient tensile strength to the plasterboard in order to prevent minor axis buckling of the studs.

The first dehydration of gypsum takes place at around 80°C, where gypsum is converted to calcium sulphate hemihydrates, and ends at approximately 120°C. In the second reaction, the calcium sulphate hemihydrates are converted to calcium sulphate anhydrite at 225°C. These values are subjected to variations depending on the assumptions of the relevant analyses, e.g. heating rate, environment, additives, resulting in discrepancies among relevant researches, especially regarding the second dehydration point. Scientific results converge on the fact that the starting plasterboard density deteriorates at almost 75% of its nominal value caused by the evaporating free and combined water; later on it remains constant in most cases except some specimens that may display shrinkage. Hence, analyses are usually carried out with constant density values at 75% of the value provided by the manufacturer.

Moreover, when water is driven off from the crystal lattices of gypsum an increase in porosity is observed. This escalation impedes heat transfer and validates the diminishing of thermal conductivity coefficient gradually until the point of the second dehydration. As the temperature continues to rise the pore structure is modified again [39]. The existing pores begin to translate until merging thus forming larger pores that facilitate convection heat transfer. Meanwhile, thermal contact between single anhydrite crystals is enhanced allowing for better conduction heat transfer. The increasingly higher convective and conductive heat transfer regime causes the resulting increments in thermal conductivity starting at the end of the dehydration process [40].

Specific heat coefficient is mostly affected by the chemical composition of the plasterboard. When large amounts of energy are required to increase the plasterboard's temperature, specific heat to temperature graphs displays minor or larger spikes, depending on the amount of energy. The first dehydration process evaporates 75% of the chemically combined water thus requiring high energy (endothermic reaction) supply followed by a second energy demand to evaporate the rest of the water. It shall be noted that while most researches neglected the effect of moisture transferring inside drywalls' pores Wang [41] suggested the utilization of this movement as the previous researches provided overconservative models. Thus, present models incorporate this favorable effect of water movement and the corresponding specific heat coefficient is called "effective". More simple models can also combine the dehydration processes into one Gaussian. The final spikes depicted in specific heat diagrams correspond to decomposition of additives that are present during the mining operation or are employed to increase the thermal performance.
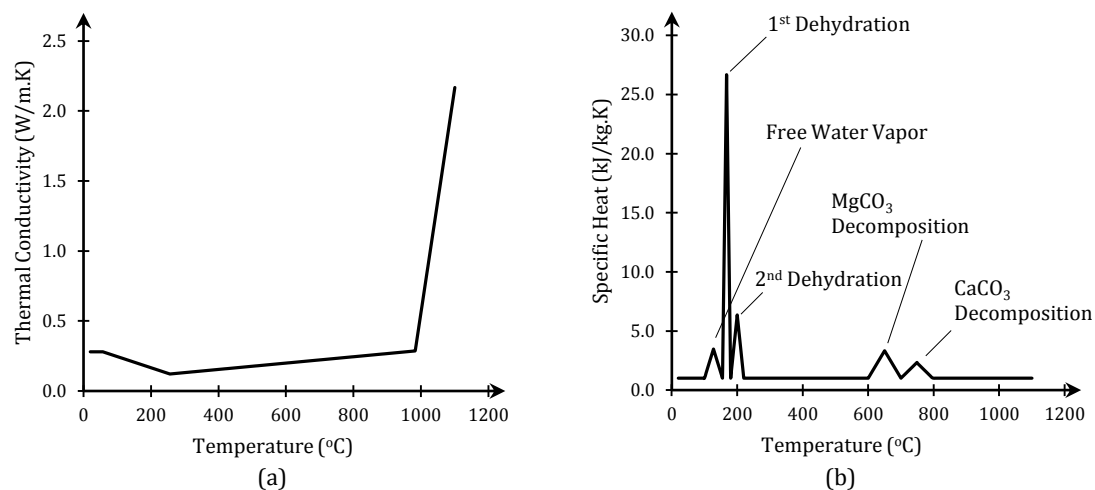


Figure 1-12: Typical drywall (a) thermal conductivity and (b) specific heat variation with temperature

Irrespective of impeding heat transfer to the load-bearing cold-formed members, the overall bearing capacity of the LSF wall system depends on securing the studs against minor axis buckling. Screws, ballistic nails and other connection types are utilized to provide lateral stability to the plasterboards as well as weak axis buckling hindering and are usually attached in the center of the flanges at regular intervals. Sultan [42] reported after his tests that plasterboard fall off occurred when the temperature at the mid-thickness of the exposed plasterboard reached 600°C whereas Kaitila [43] suggested a value of 550°C. At the tests performed by Gunalan [44], plasterboards fell off when the temperature of the inner face of the exposed plasterboard reached 900°C. However, it was reported that the constraints provided by the unexposed plasterboard layer were enough to secure the stud against both minor axis flexural and torsional buckling. Hence, valid numerical analyses can be carried out assuming that plasterboards secure the load-bearing studs against flexural-torsional buckling about the weak axis throughout the whole process. Nevertheless, most past researches indicated that when the exposed plasterboards reached 600°C they cannot provide the same heat resistance due to degradation and the temperature rises more quickly in the cavity and the unexposed plasterboard layer.

### 1.3.2    Insulation

Insulation materials are usually incorporated to fill the air cavities created by the structural members and the plasterboards. Rock fiber, glass fiber, cellulose fiber and mineral wool are the most common insulation materials; they are characterized by small thermal conductivity values to impair hit transfer from one side of the LSF wall system to the other. There is limited information available on literature to describe the thermal performance of insulating materials whereas the few existing studies display inconsistencies and scattering results. The ever increasing implementation of numerical models to assess the structural performance of load-bearing structures, that employ such materials, developed a necessity to create consolidated constitutive models to reflect the thermal properties of insulating materials. A thorough study on the thermal properties of various insulating materials was carried out at the National Research Council of Canada [45] and the corresponding results are depicted in the next figure; the values for the figures are obtained from Appendix A of the corresponding reference.



(a)                                                    (b)
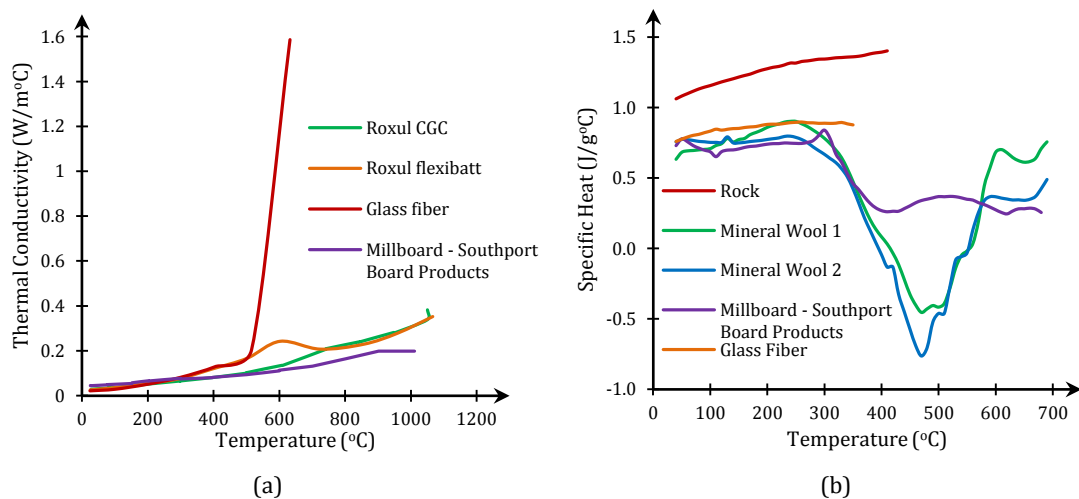
Figure 1-13: Thermal properties of various insulation materials [45]

Mineral fibers usually perform better than glass fibers because the latter present a melting point in the temperature range of 700-800$^o$C [46] which leads to sudden loss of their utility. Placing cavity insulation in light gauge steel frame walls hinders heat transfer from the fire side to the ambient side by acting as a thermal barrier due to its low thermal conductivity. This property can be crucial at temperatures greater than 600$^o$C in which plasterboard fall off [47] might occur; the insulated cavity will continue to prevent heat transfer to the unexposed plasterboard. However, many controversies dominate the benefits of cavity insulated drywall assemblies. Bridge effects have been displayed due to the low thermal conductivity of insulation compared to steel. Although temperature rise on the unexposed side is impaired, most heat transfers through the steel elements hence escalating their temperature and feeding mechanical property deterioration. Nevertheless, the assumption of earlier failure of cavity insulated formations still remains ambiguous resulting from inconsistencies between scientific evidence. Finally, thermal barriers like non-conductive materials lead in an accumulation of heat on the exposed side of the barrier which in our case yields higher temperatures on the exposed plasterboard.

### 1.3.3    Steel

Fire tampers with the thermal, mechanical and deformation properties of steel alloys. Thermal properties are associated with heat transfer and determine the temperature profile across the section; mechanical properties reflect the loss of strength and stiffness; deformation properties define the longitudinal and transverse extensions of steel elements when exposed to fire conditions. These properties are affected by the phase changes in steel thus differentiating at the presence of high temperatures. Proper assessment of all three property types is necessary to comprehend steel behavior at elevated temperatures in order to form relevant constitutive models that represent the structural response with sufficient accuracy.

Two attributes mainly concern the thermal properties of steel, thermal conductivity and specific heat. Thermal conductivity-related publishes and regulation provisions are consistent with each other and display a linear decrease with respect to temperature. Models referring to specific heat present a linear increase until 700°C with infinitesimal variations. However, the phase change occurring around 750°C, that modifies steel's atom structure from a face centered cubic to a body centered cubic, requires tremendous amounts of heat [48]. This high heat demand yields the large spike that occurs at these temperatures which also marks the initiation of high discrepancies between the available models; a fact enhanced partly by the use of iron and non structural steel alloys in many of the conducted tests.
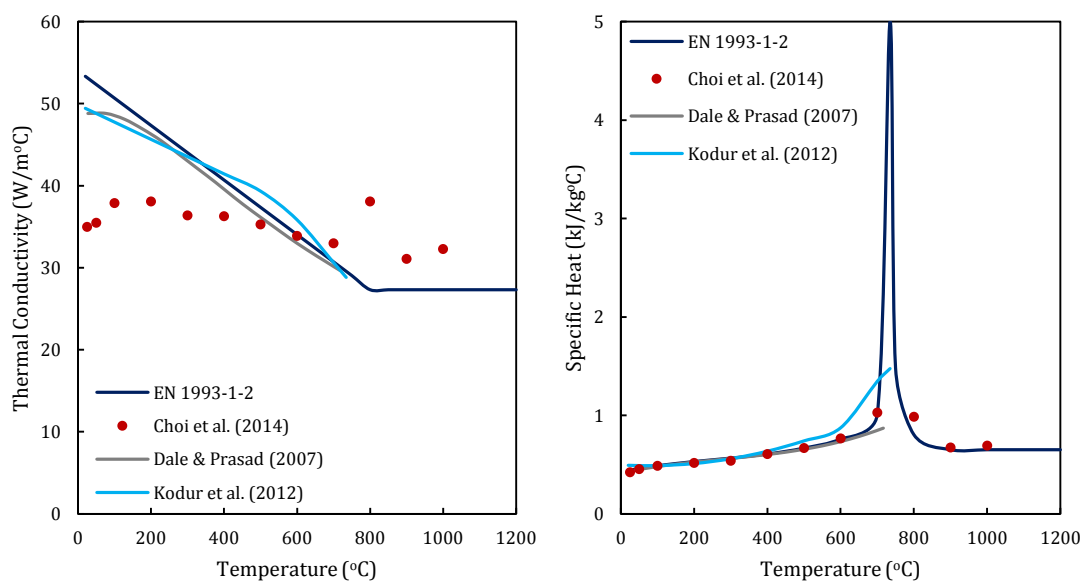


Figure 1-14: Steel thermal conductivity and specific heat variation with temperature

While thermal property variation faced low scientific interest mechanical property deterioration encountered much higher attention [49], [50], [51]. Mechanical properties consider the reduction in proportional limit, yield point, ultimate stress, elasticity modulus and strain hardening modulus; depending on the constitutive stress-strain relationship employed in pertinent studies, some of the above characteristics may be neglected. Two analyses types are utilized to derive mechanical property variation with respect to temperature rise; transient state and steady state analyses. In transient state analysis, a load is input first and then a rising temperature is imposed.

On the contrary, in steady state analysis a temperature profile is applied and then an incremental load is imposed; either load-controlled or strain-controlled. Both methods should output identical results according to Anderberg [52]. Note that, usually, tensile test are carried out and the mechanical properties during compression are generally assumed to be equivalent to properties during tension. An additional important factor influencing the test results is the heating rate as it affects the strain rate of steel [53]; relevant values can be found in the literature ranging from 3°C/min to 50°C/min depending on fire and insulation conditions [54].

As steel is heated and the temperature increases the atoms are moving further apart displaying reduced bond strength. Hence, both elasticity modulus and yield stress deteriorate with respect to temperature escalation. Relevant studies demonstrate variations in the corresponding results, a fact mainly attributed to the differences of the test specimens used in each one. Furthermore, Eurocode 3 suggests the use of different reduction factors for the yield stress of cold-formed and welded class 4 hot-rolled sections compared to hot-rolled class 1, 2 and 3 sections. Moreover, Outinen & Makelainen [55] observed that the higher yield stress of cold-formed sections was brought back to normal levels if the material was heated and then left to cool down; a process relevant to annealing process of metallurgy. They also presented constitutive stress-strain curves for pieces extracted from corners or flat parts of the cross-section in order to examine the residual effects of cold-forming on material properties at elevated temperatures using different heating rates, 45 and 20°C/min; thus also accounting for thermal creep effects (Figure 1-15).
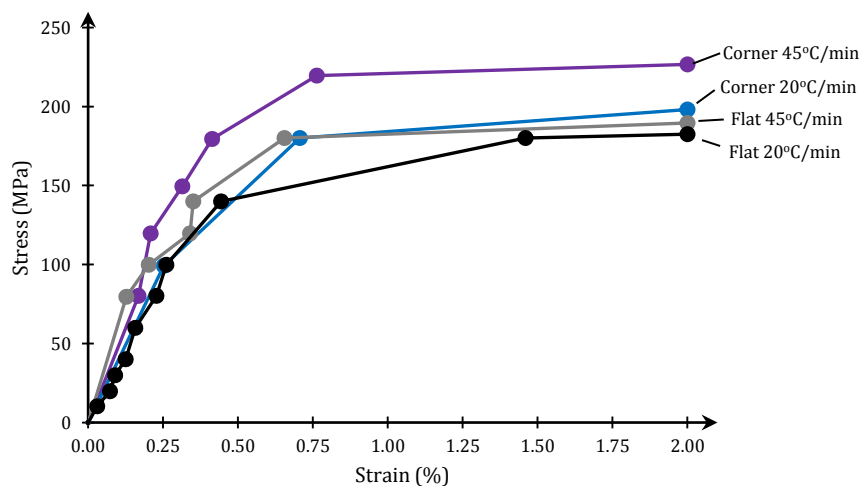


Figure 1-15: Stress-strain curves of different specimens and heating rates for steel S355J2H at 600°C [55]

Several researchers have worked on identifying proper relationships for mechanical property decay at elevated temperatures. Some of them are depicted in Figure 1-16 regarding cold-formed members following Zhao et al. [56], Outinen & Makelainen [55] and Dolamune Kankanamge & Mahendran [57] studies; the three of them are displayed along with Annex *E* of EN 1993-1-2 values for cold-formed members. In every of the four cases considered in these figures, reference to the yield stress stands for the 0.2% proof stress, i.e. the stress that yields 0.2% permanent elongation after loading and reloading (or see §1.2.4.2).
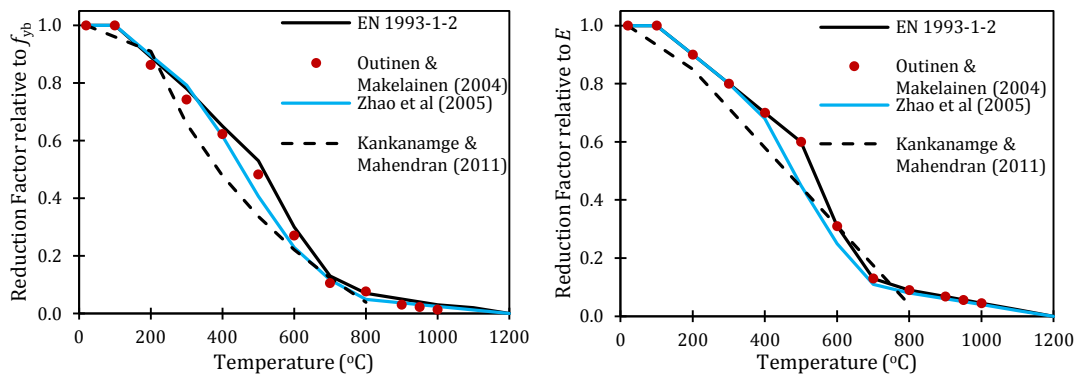
Figure 1-16: Reduction factors relative to $f_{yb}$ and $E$ for cold-formed members by pertinent sources

Finally, deformation properties concern thermal strains and elevated temperature creep. The final deformation of steel depends on strain caused by thermal effects, external loading and creep. Thermal strain reflects the percentage elongation attributed to the thermal expansion of steel with escalated temperature values. Steel expands in an almost linear fashion until approximately 700°C when phase difference begins to take place and a small shrinkage occurs, roughly around 15%, caused by the transformation of pearlite to austenite and accompanied by modification of the atomic structure of steel [58]. Most studies converge on the linear path while anomalies begin to surface around the phase difference temperature. Relevant studies [58], [59], [60] are compared to the Eurocode's suggested thermal expansion equation in the next figure.
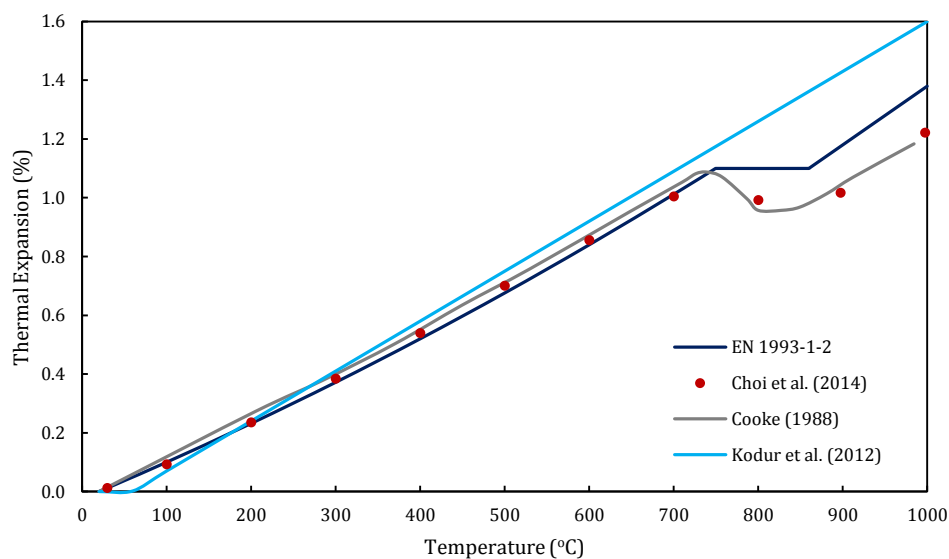


Figure 1-17: Steel thermal expansion models with respect to temperature

High temperature creep may be also evident in structural steel members when they are exposed to low heating rates. Creep deformations of steel are generally neglected at room temperature due to their small amplitude. However, at elevated temperatures, creep strains may emerge and develop into a decisive strength reduction factor. Overall, creep is considered important for temperatures higher than 400°C for ordinary steel and 250°C for cold-formed or prestressed steel [52]. Generally, high temperature creep is not explicitly accounted for in structural models. Creep cannot be expressed as a function of a distinct mechanical property or a combination of different properties as it is a function of chemical composition among others. An implicit process

is usually performed by modifying the virgin material's stress-strain law to an "effective" constitutive model that considers the effect of creep deformations. Steady-state experiments can reveal the effects of thermal creep which are then utilized to feed transient-state models.

Creep strains are distinguished into two paths, a primary phase expressed through a parabolic curve and a second phase represented by a linear path; the fundamental laws originate from Dorn's theory [61] . Harmathy [62] developed a close-formed solution in order to identify the boundaries of each path on the principal creep curve and the modified Dorn-Harmathy theory predicted creep strains as a function of time at constant temperature and stress levels with sufficient accuracy. The problem with this theory lies on the fact that assumes constant stress levels. Thus, when it comes to restrained members featuring thermal bowing that stresses vary with time and temperature, this model cannot capture the actual structural behavior.

Disregarding thermal creep is likely to lead to overestimated strength; an illustrative example advocating this opinion is demonstrated by Kodur et al. [54] by incorporating Harmathy's theory and creep models available on ANSYS [63] and checking their coincidence with test results. Two cases were considered; the first, assumed different but constant stress levels whereas the second utilized three stress stages. In the first stage, a stress of 80MPa was imposed varying by 0.22MPa/min increments for 250 minutes. The second stage reduced the induced stress with a rate of 0.22MPa/min until $t$=480min. The final stage kept the stress level constant at approximately 80MPa until the end of the test at $t$=600min. The temperature was held constant at 550°C and the corresponding results are depicted in the next figure. According to the authors, Eurocode's constitutive materials law incorporates partially high temperature creep effects, thus demonstrating higher prediction accuracy compared to the ASCE stress-strain relationships.



(a) $d\sigma/d\varepsilon$=0 ; T=550°C                                  (b) $d\sigma/d\varepsilon$≠0 ; T=550°C
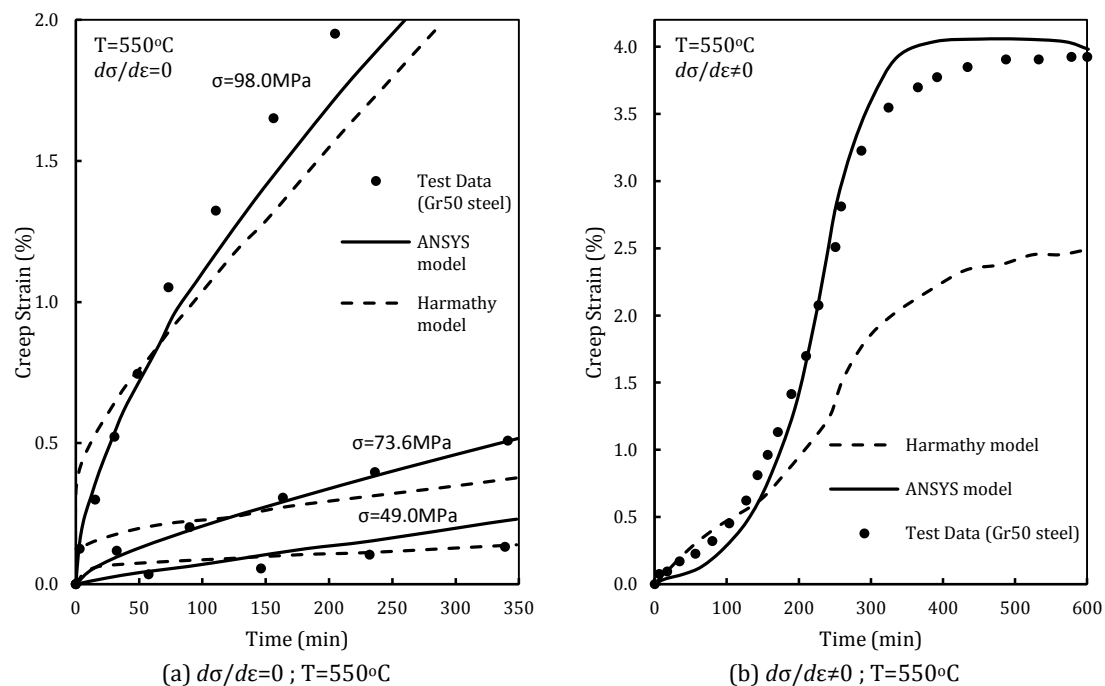
Figure 1-18: Creep strains predicted by ANSYS and Harmathy models compared to test data [54]

## 1.4   Structural Fire Safety

Fire safety deals with the potential of fire hazard in residential, industrial and commercial facilities. The importance of providing fire shielded constructions led into the founding of fire safety engineering. This engineering aspect handles the mitigation of fire risks through the utilization of preventive and suppressive measures in order to alleviate life loss and property damage. Three are the most common ways of assessing the ability of a structure to safely carry loads while exposed to fire conditions, each one associated with a specific domain, i.e. time, temperature and strength. Prescriptive methods usually incorporate time domain approaches, i.e. the failure time should be greater than the fire duration value adopted in the pertinent regulation [64].

Fire protection engineering interacts with every engineering discipline involved in constructions by intervening in relevant fields in order to assuage fire risk [65]. From an architectural perspective, fire engineers evaluate the conceptual design in terms of firefighter access and civilian evacuation exits. Structural engineers' standpoint involves tampering with material mechanical properties and sectional dimensions, sprinkler systems and wall openings. From a mechanical engineer's point of view, fire engineers calculate water pressure for sprinkler pipes, check the applicability of extinguishing agents and control air/gas flows through ventilation systems to avoid smoke aggregation. Fire engineers collaborate with electrical engineers to construct fire alarm systems, automated extinguishers and emergency power supply lines. Finally, fire engineers work on leaking possibilities, material flammability, potential ignition sources etc.; a field widely related to chemical engineering.

### 1.4.1   Fire safety engineering design concerns

On the way of identifying and limiting fire-related potential risks, fire safety engineering aspects can be summarized in five main design concerns [66]:

   i.   *Ignition control*
   ii.  *Appropriate escape means*
   iii. *Detection systems*
   iv.  *Control of fire spread*
   v.   *Structural collapse impeding*

Ignition control comprises three distinguished steps, i.e. flammability control, fire growth mitigation and fire safety management. Controlling the flammability is the first step towards limiting the spread of fire. This is done by meticulous selection of the materials used throughout the whole building, especially those used as linings and surface coatings. Secondly, using vertical or horizontal compartments impairs the growth of fire if smoke and flame transferring to adjacent rooms is impeded. Each compartment needs to be able to sustain certain amounts of heat to provide enough time to the fire brigade to arrive at the site. Furthermore, combustible rubbishes should frequently be removed from the building interior and new modifications should

be executed only if they meet specific design criteria. Finally, a plan regarding fire situation should be available. In crowded places like multistory residents or shopping centers performing fire management can be really hard. Therefore, ad hoc instructions are necessary along with maintenance records of the fire protecting mechanisms and a group of people trained to implement the corresponding fire safety plan at the hour of need.

Escape means cover a series of fireproof places that provide adequate safety to people. Regulations usually provide maximum distances from safe places depending on both the building type/usage and the escape route, e.g. corridor, staircase etc. Safe places include fire-protected stairwells, fire escape doors leading outside etc. Statutory requirements often involve a minimum amount of fire escapes accompanied by the necessary dimensions of the corresponding routes. Escape routes must be lined with non-combustible and anti-toxic materials except fire doors since they do not contribute to the structural stability of the escape route. It is equally important to ensure that escape routes are not blocked in order to utilize their maximum human movement capacity while fire doors are not locked and they do not display any type of malfunction.

Detection systems can be either manual or automatic and are used to detect fire. Manual systems, such as the traditional fragile glass, require the presence of a human to trigger the alarm. Although relatively simple in terms of installation and use they may prove inefficient if fire ignition occurs at isolated parts or during non-working hours. Automatic systems involve heat or smoke detectors that activate fire alarms and extinguish systems. Their problems lie on their inability to adjust to unique conditions pertained in specific rooms such as kitchens, garages etc., although this problem is dealt with using computer control. By the time fire is detected, it is essential to keep smoke spread at acceptable levels to allow clear visibility and not disorientation; normally smoke is not allowed to fall below 2.5-3.0m above floor level. Sensitive areas can be equipped with fire-fighting systems such as sprinklers that have proved to significantly reduce ceiling temperature and smoke volume accumulation [67].

Compartmentalization can be very effective in isolating critical areas exposed to high temperatures. This prevention of fire spread can advocate the evacuation process by allowing people to move near endangered zones during the start of the ignition process. It can also detain fire from destroying various building areas thus reducing property damage. Compartment zones are usually relatively small areas deriving from certain rules, e.g. represent a fraction of the floor area. Although the process of compartmentalizing is generally unclear [68], its efficiency should be ensured through maintenance and renovation procedures.

Last but not least, it is crucial that the building will maintain its structural integrity at some level for a specific duration. Even though evacuation is nominally a fast process, structures should be able to sustain certain amounts of imposed loading in order to provide enough time to the firefighters to extinguish the fire. Structural collapse prevention is achieved through active and/or passive approaches [66]. In the active approach, the fire/temperatures are contained to

within reasonable limits for a specific duration in order to avoid material property deterioration and prevent structural collapse. The passive approach suggests designing the structure in a way that when exposed to elevated temperatures its load-bearing capacity will be enough to sustain certain imposed loads. Actual structures usually incorporate both approaches; nevertheless, the difference between the two approaches has been recently clarified, even though a certain amount of trade off exists between them as they are interdependent.

### 1.4.2    Fire limit states

Composite members such as light gauge steel frame wall assemblies take advantage of a series of material properties attributed to the various materials that comprise the wall system in order to achieve stability during fire conditions. Steel studs utilize their bearing capacity and represent the structural members responsible for sustaining the walls during induced loading. Although incombustible, steel members' susceptibility to fire arises from the fast deterioration of their strength and stiffness. In order to secure the load-bearing elements against fire, gypsum plasterboards are usually employed as cladding members due to their high fire resistance. Furthermore, insulation materials are installed in the air cavities to provide additional thermal resistance and temperature rise hindering at the unexposed face of the wall. Considering the formation of such wall configurations, three fire limit states are identified:

i.   *Insulation* (*I*), based on this criterion the temperature on the unexposed face of the wall should be low enough in order to prevent combustion of the stored materials
ii.  *Integrity* (*E*), under no circumstances smoke or flames are allowed to penetrate the wall and present at the unexposed face. Excessive deformation and plasterboard cracking could lead to loss of integrity prior to complete fall off of the plasterboard linings.
iii. *Load-bearing capacity* (*R*), this criterion is deemed to have been satisfied when the wall cannot sustain the imposed loads over the ad hoc time duration. Since the bearing capacity of the wall is mainly attributed to the studs, when they reach fracture point or display excessive deformation the wall system is considered to have failed.

While the Integrity criterion needs large-scale physical experiments to evaluate structural members' integrity, the other two criterions can be examined using numerical investigations. The object of this study concerns the validation of the load-bearing capacity criterion of LSF wall systems which can be assessed according to the provisions of EN 1991-1-2 [69] in either the time, temperature or strength domain. During standard furnace tests, the Insulation criterion is violated if the temperature of the unexposed face reaches $140^{\circ}$C or any local temperature value exceeds $180^{\circ}$C.

### 1.4.3    Fire loads

Fire curves generally comprise three general types that also constitute the corresponding assessment models. The simplest model involves exposing individual elements or parts of the structure to standard temperature-time curves either by furnace tests or numerical studies and

the duration of the fire is determined by pertinent regulations provisions. A more complicated method incorporates standard fire curves but the duration of the fire exposure is derived after taking into account the actual fire characteristics of the compartment. For the estimation of the time duration required for the member to sustain its bearing capacity initially proposed equations included parameters such as equivalent fire load (kg), area of openings (m²) and total area (m²). Further refinements were made to improve the prediction accuracy by incorporating the compartment thermal boundaries (including ventilation systems and wall materials) and the relevant fire load per unit area (MJ/m²). Two methods are used, namely the temperature base [70] and the normalized heat load base [71]. Finally, the third and most complicated but also sophisticated method considers the actual fire characteristics of the compartment to derive the temperature-time curve using parametric equations and the first limit state criterion to be violated marks the fire resistance rating (duration).

The attempts to produce methods for the derivation of a unified fire safety factor for the whole structure are not developed in a way allowing for mass implementation [66]. Hence, prescriptive methods unfolded in order to alleviate the computational effort but maintaining a substantial accuracy. Prescriptive methods include the use of standardized temperature-time equations that unraveled after the interpretation of standard fire test. During standard fire tests, a member is loaded at the stress levels that expected to occur at its actual position in the real structure and it is then heated with a proper standardized curve. It is assumed that most fires are fed by cellulosic combustible materials resulting in temperature-time curves such as the most widely used curve provided by ISO 834:

$$\theta_g = \theta_o + 345 \log(8t + 1) \tag{1.1}$$

where $\theta_g$ is the furnace temperature (°C), $\theta_o$ is the ambient temperature (EN 1991-1-2 uses 20°C as ambient temperature in the above expression), and $t$ is the elapsed time (min).

This equation is not exemplary for describing analytical solutions of the Fourier equation of heat transfer when the standard furnace curve is imposed on one or more elements; thus alternative expressions began to surface some of which are presented hereafter by Williams-Leir and Fackler.

   i.   *Williams-Leir* [72]
        $$\theta_g = \theta_o + 532(1 - e^{-0.01t}) - 186(1 - e^{-0.05t}) + 820(1 - e^{-0.2t}) \tag{1.2}$$

   ii.  *Fackler* [73]
        $$\theta_g = \theta_o + 774\left(1 - e^{-0.49\sqrt{t}}\right) + 22.2\sqrt{t} \tag{1.3}$$

Furthermore, it was observed that fire curves for members placed in facades or members exposed to fires created by other combustible materials, such as petrochemicals, do not comply with the hereinabove expressions. Appropriate expressions that consider these features are

included in EN 1991-1-2. External fire curves are smoother than standard fire curves whereas hydrocarbon temperature-fire curves are more severe.

    i.   *External Fire Curve according to EN 1991-1-2*

$$\theta_g = 20 + 660(1 - 0.687e^{-0.32t} - 0.313e^{-3.8t}) \tag{1.4}$$

    ii.   *Hydrocarbon Curve according to EN 1991-1-2*

$$\theta_g = 20 + 1080(1 - 0.325e^{-0.167t} - 0.675e^{-2.5t}) \tag{1.5}$$

Natural fires (also called real or parametric) are characterized by different temperature-time curves compared to the standardized curves. They can be relatively simple by including only openings and combustible material type placed in the building interior or extremely complicated by incorporating specific heat release rates by material, ignition temperatures for each material, density distribution, energy flux through combustion and radiation etc [74]. Overall, natural fires consolidate fluid dynamics' extension on fire spread fed by the parameters dominating each facility under investigation. Natural fires can be broken down into three distinct phases: i) the pre-flashover or growth phase, ii) the post-flashover or fully developed phase, and iii) the decay or cooling phase. The term *flashover* refers to the transition from localized fires to entire conflagration of every combustible material available in the compartment area, initiating a rapid temperature increase over a short duration. In the next figure, the fire growing phases are graphically displayed [75] and a comparison between EN 1991-1-2 prescriptive curves and different fuel/ignition test types is performed [76].
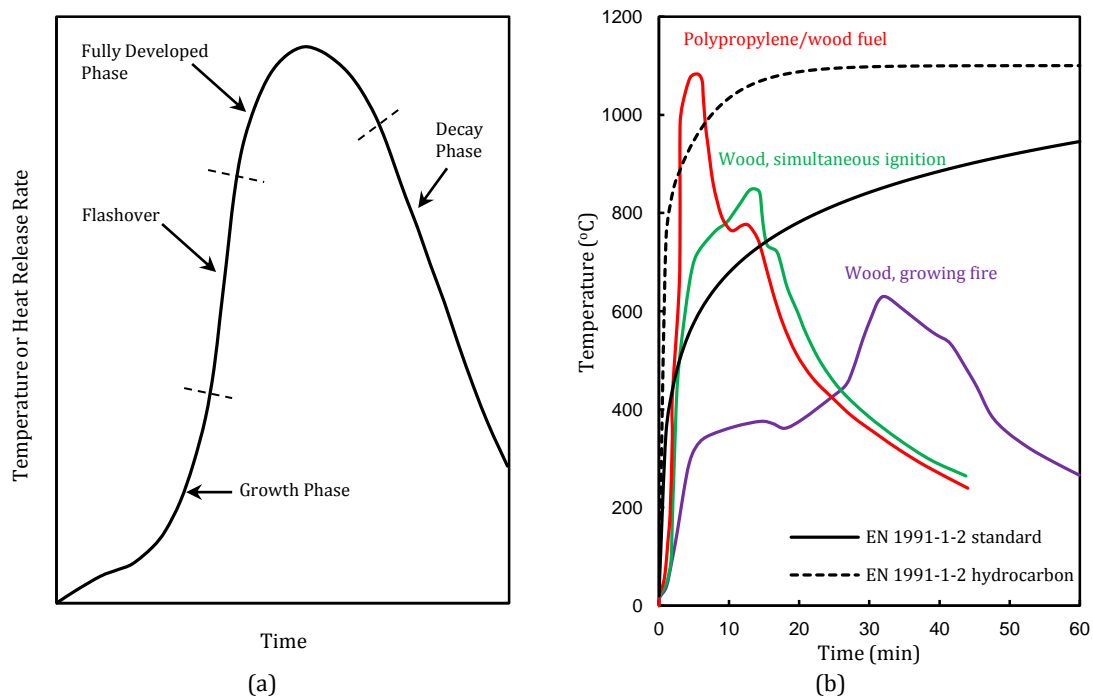


Figure 1-19: (a) Natural fire phases [75] (b) Prescriptive approaches and experimental tests [76]

## 1.5   Research Scope and Thesis Contents

This study investigates the structural behavior of load-bearing cold-formed steel members at elevated temperatures by utilizing numerical models. These lipped channel steel members represent the studs of four different drywall configurations. Typical drywall formations are considered with single or double plasterboard layers and with or without thermal insulation. Both the temperature profiles and the results of the structural analyses are obtained by commercial finite elements software, i.e. ANSYS and ADINA. The whole process incorporates state of the art models, proposed by various researchers, in order to simulate the temperature-related thermal, mechanical and deformation properties of the composite drywall-steel assemblies. The main object of this Thesis is to underline the variation of the numerical simulations with the provisions of the pertinent parts of Eurocode 3, with the hope of identifying the reasons behind the over-conservative regulation provisions. In particular, the outline of the chapters employed in order to introduce the theoretical background, state the research problem and carry out the computational process are explained hereinafter:

Chapter 1:   Introduces the research problem while stating the theoretical background behind the behavior of cold-formed steel sections at ambient temperatures. Provides relevant information on load-bearing drywall configurations, including the temperature variation of the physical properties of every material involved. Finally, it summarizes the uncertainties surrounding proper identification of property deterioration, reflecting the ambiguous behavior at fire situations. It aims at providing a thorough view of all the aspects involved, vital for comprehending the following chapters, so long as the reader has basic relevant knowledge.

Chapter 2:   Presents literature review findings based on the results of previous researches. It also describes previous experimental or numerical analyses performed at fire situations and the methodologies proposed/followed by others. Furthermore, it comprises the suggestions of Eurocode 3 regarding cold-formed members exposed to fire situations along with the solution process of the direct strength method.

Chapter 3:   States the ambient temperature investigation. It includes linearized buckling analyses using finite element and finite strip solution processes; provides geometric and material non-linear analyses with geometric imperfections along with analytical and semi-analytical estimations of the corresponding axial strength to validate the numerical results.

Chapter 4:   Contains the analysis at fire conditions. Describes the methodology followed and the corresponding results concerning both the thermal and, mainly, the structural performance of the steel studs under a concentric vertical compressive load with or without simultaneous external flexural loading.

Chapter 5:   Provides the summarizing of the prominent findings of this study and suggestions for future research.

# 2 Literature Review

## 2.1 Introduction

The differences in structural behavior of cold-formed and hot-formed members have led to the founding of specific design requirements regarding the application of cold-formed structural elements. The standard EN 1993-1-3 reflects the approach of the European perspective in dealing with the peculiarities of thin-walled members. The American Iron and Steel Institute (AISI) has provided a standalone specification, named S100 and lastly amended in 2007, for the design of cold-formed steel structural members which also includes the alternative direct strength method to the standard effective width approach. The Australian and New Zealand commissions have collaborated to produce guidance for the design of cold-formed sections, following the provisions of the AISI specification. The result was a new specification named AS/NZS 4600 lastly amended in 2005.

The above standards usually pertain to the structural behavior at ambient temperatures and do not contain information about structural fire design. This issue is dealt with separately by introducing new standards like EN 1993-1-2. However, there is not regulative guidance for load-bearing drywall assemblies in detail. Temperature profiles can be obtained using heat transfer equations offered by various specifications, which however lack detailed descriptions about non-uniform temperature profiles across the members. As a result, over-conservative solutions are usually employed to derive satisfying fire resistance ratings for the whole structure or for separate members, respectively.

Systematic research has been undertaken to determine the thermal, mechanical and deformation properties of structural steel. However, not much effort has been put on identifying the corresponding properties of gypsum plasterboard and thermal insulation. As a result, even though recent researchers conducted relevant studies and have concluded to meaningful results, there has not been any regulative constitution about load-bearing drywall assemblies. This fact can be attributed to the dispersion in the results of relevant studies as well as the overall low amount of numerical and experimental systematic work in the whole plasterboard-insulation-steel members system.

This chapter introduces a detailed description on the approach of Eurocode 3 to the structural fire design of cold-formed steel members as well as the approach of the direct strength method. Information about numerical and experimental studies pertinent to the design of load-bearing drywall assemblies at elevated temperatures is also presented along with the design methodologies proposed by other researchers. Moreover, an attempt to illustrate every aspect involved in the simulation of load-bearing drywalls is performed by emphasizing the evolution of the relevant models. Finally, the efficiencies and deficiencies of each study are demonstrated based on new evidence that unfolded from the findings of the most recent investigations.

## 2.2   Eurocode 3

Designing according to Eurocode 3 comprises the use of four different parts. EN 1993-1-1 includes the approach in dealing with global buckling effects and the interaction between axial compression and bending moment; EN 1993-1-3 states the methodology to derive the effective cross-section which is aligned with clauses from EN 1993-1-5; EN 1993-1-2 provides the reduction factors and the design equations at fire situations as well as reductions laws for the thermal, mechanical and deformation properties of steel.

### 2.2.1   Cold-formed thin gauge steel members

The structural analysis of thin-walled cold-formed members begins with estimating the effective cross-section. At first, a check on whether the effects of rounded corners can be omitted is performed. In order to assume that the cross-section is constituted by plane elements with sharp corners, the two following conditions shall be met:

$$r \leq 5t \tag{2.1}$$
$$r \leq 0.10b_\mathrm{p} \tag{2.2}$$

where $r$ the internal or external corner radius and $b_\mathrm{p}$ the notional flat width.

The incorporation of flange or web stiffeners shall be within specific geometric limits in order for the stiffener to provide sufficient stiffness to the adjacent part while avoiding primary buckling. Hence, in case of a flange stiffener with length $c$ or a lip stiffener with length $d$, the following limits apply:

$$0.2 \leq c/b \leq 0.6 \tag{2.3}$$
$$0.1 \leq d/b \leq 0.3 \tag{2.4}$$

where $b$ is the flange width.

Subsequently, a net width $\bar{b}_\mathrm{p}$ is selected for each plane element measured from the unbuckled junctures of the adjacent parts in order to calculate the plate slenderness $\bar{\lambda}_\mathrm{p}$ of each element from the following equation:

$$\bar{\lambda}_\mathrm{p} = \frac{\bar{b}_\mathrm{p}/t}{28.4\varepsilon\sqrt{k_\sigma}} \tag{2.5}$$

where $t$ the element's thickness, $\varepsilon$ the coefficient depending on the yield stress $f_\mathrm{yb}$ and $k_\sigma$ the buckling factor depending on the stress distribution $\psi = \sigma_2/\sigma_1$ for internal compression elements or has a value depending on the ratio of the lip's net width to the flange's net width.

The range of the relative slenderness of each subpanel addresses its susceptibility to local buckling. Therefore, a reduction coefficient $\rho \leq 1.0$ multiplies the net width of each subpanel to produce an effective width. Each subpanel is characterized as internally or outstandingly compressed while the unbuckled parts that form its limits are, i) web/flange juncture, ii) intermediate web stiffeners, iii) intermediate or edge flange stiffeners and iv) intermediate or

edge lip stiffener. The parts forming between the above locations determine the net width of the $i$ subpanel with effective width $b_{\text{eff}}$ resulting from:

$$b_{\text{eff}} = \rho \bar{b}_{\text{p}} \tag{2.6}$$

where the reduction coefficient $\rho$ is determined by:

Internal compression elements

$$\rho = 1.0 \qquad\qquad\qquad \text{for } \bar{\lambda}_{\text{p}} \leq 0.673 \tag{2.7}$$

$$\rho = \frac{\bar{\lambda}_{\text{p}} - 0.055(3 + \psi)}{\bar{\lambda}_{\text{p}}^2} \leq 1.0 \qquad\qquad \text{for } \bar{\lambda}_{\text{p}} > 0.673 \text{ ; where } (3 + \psi) \geq 0 \tag{2.8}$$

Outstand compression elements

$$\rho = 1.0 \qquad\qquad\qquad \text{for } \bar{\lambda}_{\text{p}} \leq 0.748 \tag{2.9}$$

$$\rho = \frac{\bar{\lambda}_{\text{p}} - 0.188}{\bar{\lambda}_{\text{p}}^2} \leq 1.0 \qquad\qquad \text{for } \bar{\lambda}_{\text{p}} > 0.748 \tag{2.10}$$

Next, the gross cross-sectional area $A_{\text{s}}$ and the second moment of area $I_{\text{s}}$ for each stiffener and the adjacent parts is calculated in order to determine the additional stiffness provided by each stiffener. These variables depend on the stiffness's type, i.e. intermediate or edge. The stiffness of an intermediate stiffener (the stiffener divides a plane element into two subpanels) after conservatively excluding the rotational stiffness is obtained from equation:

$$K = \frac{3(b_1 + b_2)Et^3}{b_1^2 \, b_2^2 \, 12(1 - v^2)} \tag{2.11}$$

where:

$b_1$        the distance between the stiffener and the left edge of the left subpanel

$b_2$        the distance between the stiffener and the right edge of the right subpanel

$E$        the elasticity modulus

$t$        the nominal thickness

$v$        Poisson ratio

The stiffness of an edge stiffener is determined by:

$$K = \frac{Et^3}{4(1 - v^2)} \times \frac{1}{b_1^2 h_{\text{w}} + b_1^3 + 0.5 b_1 b_2 h_{\text{w}} k_{\text{f}}} \tag{2.12}$$

where:

$b_1$        the distance between web/top flange juncture and the gravity center of the stiffener

$b_2$        the distance between web/bottom flange juncture and the gravity center of the stiffener

$h_{\text{w}}$        the web depth

$k_{\text{f}}$        has zero value if the other flange is under tension or has a value of $A_{\text{eff,2}}/A_{\text{eff,1}}$ if the other flange is compressed; where the index "2" corresponds to the other flange and the index "1" corresponds to the flange under investigation

$v$        Poisson ratio

The elastic critical buckling stress for each element is determined by:

$$\sigma_{\text{cr,s}} = \frac{2\sqrt{KEI_{\text{s}}}}{A_s} \qquad\qquad (2.13)$$

where:

$K$        the stiffness of the stiffener

$E$        the elasticity modulus

$I_{\text{s}}$        the second moment of area of the stiffened area

$A_{\text{s}}$        the effective cross-section of the stiffened area

The relative slenderness of each part is calculated by:

$$\bar{\lambda}_{\text{d}} = \sqrt{\frac{f_{\text{yb}}}{\sigma_{\text{cr,s}}}} \qquad\qquad (2.14)$$

Hence, the reduction factor $\chi_{\text{d}}$ reflecting the distortional buckling effects on the cross-section is:

$$\chi_{\text{d}} = 1.0 \qquad\qquad \text{if} \ \ \bar{\lambda}_{\text{d}} \leq 0.65 \qquad\qquad (2.15)$$

$$\chi_{\text{d}} = 1.47 - 0.723\bar{\lambda}_{\text{d}} \qquad \text{if} \ \ 0.65 < \bar{\lambda}_{\text{d}} < 1.38 \qquad\qquad (2.16)$$

$$\chi_{\text{d}} = 0.66/\bar{\lambda}_{\text{d}} \qquad\qquad \text{if} \ \ 1.38 \leq \bar{\lambda}_{\text{d}} \qquad\qquad (2.17)$$

An iteration process can take place by introducing an initial relative slenderness $\bar{\lambda}_{\text{p,red}}$ in order to calculate the reduction factor $\rho$ for the effective width of each subpanel and the effective area of the stiffener and the adjacent parts. The new relative slenderness is determined by:

$$\bar{\lambda}_{\text{p,red}} = \bar{\lambda}_{\text{p}}\sqrt{\chi_{\text{d}}} \qquad\qquad (2.18)$$

The hereinbefore procedure is repeated until the refined value of the reduction factor $\chi_{\text{d}}$ approaches the value of the previously executed iteration. The final value of $\chi_{\text{d}}$ is employed to reduce the thickness of each element according to the corresponding reduction factor. Hence, the effective area of each element deteriorates to account for the effects of local/distortional buckling and the axial compressive strength $N_{\text{c,Rd}}$ of the cross-section is calculated by:

$$N_{\text{c,Rd}} = A_{\text{eff}}f_{\text{yb}}/\gamma_{\text{M0}} \qquad\qquad (2.19)$$

The axial strength of a member under pure compression is determined using the strength of the cross-section reduced by a factor $\chi$ to account for the effects of global buckling. The bearing capacity of class 4 steel members under compression is determined by:

$$N_{\text{b,Rd}} = \chi A_{\text{eff}}f_{\text{yb}}/\gamma_{\text{M0}} \qquad\qquad (2.20)$$

where $\chi$ is the minimum of $\chi_y$ and $\chi_z$ corresponding to strong and minor axis flexural (Euler) buckling. The process of calculating the reduction factor $\chi$ is typically described in Eurocode 3, part 1.1 but the appropriate buckling curve derives from table 6.3 of EN 1993-1-3.

When axial compression coexists with bending moment or when the effects of neutral axis shift are considered, EN 1993-1-1 proposes the satisfaction of the following equations to ensure the stability of a member:

$$\frac{N_{\text{Ed}}}{\chi_{\text{y}} N_{\text{Rk}}/\gamma_{\text{M1}}} + k_{\text{yy}} \frac{M_{\text{y,Ed}} + \Delta M_{\text{y,Ed}}}{\chi_{\text{LT}} M_{\text{y,Rk}}/\gamma_{\text{M1}}} + k_{\text{yz}} \frac{M_{\text{z,Ed}} + \Delta M_{\text{z,Ed}}}{M_{\text{z,Rk}}/\gamma_{\text{M1}}} \leq 1.0 \tag{2.21}$$

$$\frac{N_{\text{Ed}}}{\chi_{\text{z}} N_{\text{Rk}}/\gamma_{\text{M1}}} + k_{\text{zy}} \frac{M_{\text{y,Ed}} + \Delta M_{\text{y,Ed}}}{\chi_{\text{LT}} M_{\text{y,Rk}}/\gamma_{\text{M1}}} + k_{\text{zz}} \frac{M_{\text{z,Ed}} + \Delta M_{\text{z,Ed}}}{M_{\text{z,Rk}}/\gamma_{\text{M1}}} \leq 1.0 \tag{2.22}$$

where:

| | |
|---|---|
| $N_{\text{Ed}}$, $M_{\text{y,Ed}}$ and $M_{\text{z,Ed}}$ | is the design compressive force and the maximum moments about the strong and minor axis, respectively |
| $N_{\text{Rk}}$, $M_{\text{y,Rk}}$ and $M_{\text{z,Rk}}$ | are the resistance values based on the properties of the effective cross-section |
| $\Delta M_{\text{y,Ed}}$ and $\Delta M_{\text{z,Ed}}$ | the additional moments duo to centroidal axis shift |
| $k_{\text{yy}}, k_{\text{yz}}, k_{\text{zy}}, k_{\text{zz}}$ | are the interaction factors |
| $\chi_{\text{y}}, \chi_{\text{z}}$ | the reduction factors due to flexural buckling |
| $\chi_{\text{LT}}$ | the reduction factor due to flexural-torsional buckling, takes a value of 1.0 for members not susceptible to torsional buckling |

An alternative interaction relationship is suggested by EN 1993-1-3 according to which:

$$\left(\frac{N_{\text{Ed}}}{N_{\text{b,Rd}}}\right)^{0.8} + \left(\frac{M_{\text{Ed}}}{M_{\text{b,Rd}}}\right)^{0.8} \leq 1.0 \tag{2.23}$$

where $N_{\text{b,Rd}}$ and $M_{\text{b,Rd}}$ are the design values of axial and flexural buckling resistance and $M_{\text{Ed}}$ contains the additional moment resulting from the shift of the centroidal axis.

### 2.2.2   Structural fire design

Eurocode 3, part 1.2 provides the temperature-related variation of the thermal properties of steel. According to EN 1993-1-2, thermal properties comprise thermal conductivity, thermal elongation and specific heat. Furthermore, the reduction laws applying to elasticity modulus and yield stress are also determined. The previous chapter has presented the corresponding figures that depict these reduction laws while EN 1993-1-2 states the equations that determine them assuming ambient temperature 20°C.

The relationships expressing the ability of a member to withstand external loading are now modified to reflect the behavior at elevated temperatures. Hence, for compression class 4 members, the design axial buckling resistance $N_{\text{b,fi,t,Rd}}$ shall be determined by:

$$N_{\text{b,fi,t,Rd}} = \frac{\chi_{\text{fi}} \, A_{\text{eff}} \, k_{\text{y,}\theta} \, f_{\text{yb}}}{\gamma_{\text{M,fi}}} \tag{2.24}$$

where $\chi_{\text{fi}}$ is the reduction factor for flexural buckling in the fire design situation and $k_{\text{y,}\theta}$ the reduction factor applying to the yield stress at temperature $\theta$. Note that in cases of non-uniform temperature distributions, the maximum cross-sectional temperature shall be used.

The reduction factor for flexural buckling $\chi_{\text{fi}}$ should be taken as the lesser of the values $\chi_{\text{y,fi}}$ and $\chi_{\text{z,fi}}$ and is now obtained by:

$$\chi_{\text{fi}} = \frac{1}{\varphi_\theta + \sqrt{\varphi_\theta^2 - \bar{\lambda}_\theta^2}} \tag{2.25}$$

with

$$\varphi_\theta = \frac{1}{2}\left[1 + \alpha\bar{\lambda}_\theta + \bar{\lambda}_\theta^2\right] \tag{2.26}$$

and

$$a = 0.65 \times \left(\frac{235}{f_y}\right)^{0.5} \tag{2.27}$$

The non-dimensional slenderness $\bar{\lambda}_\theta$ derives from the corresponding value at ambient temperatures multiplied by the fraction of the proportional reduction of the yield stress to the elasticity modulus and is given by:

$$\bar{\lambda}_\theta = \bar{\lambda}\left(\frac{k_{y,\theta}}{k_{E,\theta}}\right)^{0.5} \tag{2.28}$$

where $k_{y,\theta}$ and $k_{E,\theta}$ the reduction factors applying to the yield stress and modulus of elasticity and $\bar{\lambda}$ the non-dimensional slenderness at ambient temperature.

When compression interacts with bending, the design buckling resistance of class 4 steel members at temperature $\theta$ shall be verified by satisfying the following expressions:

$$\frac{N_{\text{fi,Ed}}}{\chi_{\text{min,fi}}A_{\text{eff}}\,k_{y,\theta}\,f_{yb}/\gamma_{\text{M,fi}}} + \frac{k_y M_{y,\text{fi,Ed}}}{W_{\text{eff,y}}k_{y,\theta}f_{yb}/\gamma_{\text{M,fi}}} + \frac{k_z M_{z,\text{fi,Ed}}}{W_{\text{eff,z}}k_{y,\theta}f_{yb}/\gamma_{\text{M,fi}}} \leq 1.0 \tag{2.29}$$

$$\frac{N_{\text{fi,Ed}}}{\chi_{\text{z,fi}}A_{\text{eff}}\,k_{y,\theta}\,f_{yb}/\gamma_{\text{M,fi}}} + \frac{k_{\text{LT}} M_{y,\text{fi,Ed}}}{\chi_{\text{LT,fi}}W_{\text{eff,y}}k_{y,\theta}f_{yb}/\gamma_{\text{M,fi}}} + \frac{k_z M_{z,\text{fi,Ed}}}{W_{\text{eff,z}}k_{y,\theta}f_{yb}/\gamma_{\text{M,fi}}} \leq 1.0 \tag{2.30}$$

where $\chi_{\text{LT,fi}}$ is determined with the same process as the one described in equations 2.25-2.28 but for the case of flexural-torsional buckling by using $\bar{\lambda}_{\text{LT}}$ instead of $\bar{\lambda}$ and the values $k_y$, $k_z$, $k_{\text{LT}}$ are given by:

$$k_{\text{LT}} = 1 - \frac{\mu_{\text{LT}}N_{\text{fi,Ed}}}{\chi_{\text{z,fi}}A_{\text{eff}}k_{y,\theta}f_y/\gamma_{\text{M,fi}}} \leq 1.0 \tag{2.31}$$

$$\text{with: } \mu_{\text{LT}} = 0.15\bar{\lambda}_{\text{z,}\theta}\beta_{\text{M,LT}} - 0.15 \leq 0.9 \tag{2.32}$$

$$k_y = 1 - \frac{\mu_y N_{\text{fi,Ed}}}{\chi_{\text{y,fi}}A_{\text{eff}}k_{y,\theta}f_y/\gamma_{\text{M,fi}}} \leq 1.0 \tag{2.33}$$

$$\text{with: } \mu_y = \left(1.2\beta_{\text{M,y}} - 3\right)\bar{\lambda}_{\text{y,}\theta} + 0.44\beta_{\text{M,y}} - 0.29 \leq 0.8 \tag{2.34}$$

$$k_z = 1 - \frac{\mu_y N_{\text{fi,Ed}}}{\chi_{\text{z,fi}}A_{\text{eff}}k_{y,\theta}f_y/\gamma_{\text{M,fi}}} \leq 1.0 \tag{2.35}$$

$$\text{with: } \mu_z = \left(2\beta_{\text{M,z}} - 5\right)\bar{\lambda}_{\text{z,}\theta} + 0.44\beta_{\text{M,z}} - 0.29 \leq 0.8 \text{ and } \bar{\lambda}_{\text{z,}\theta} \leq 1.1 \tag{2.36}$$

The equivalent uniform moment factors $\beta_{\text{M}}$ are obtained from the next figure.
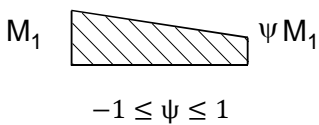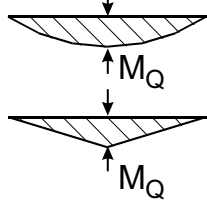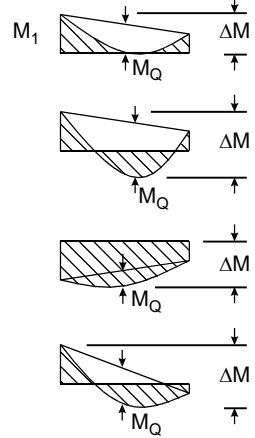
| Moment diagram | Equivalent uniform moment factor $\beta_M$ |
|---|---|
| End moments<br><br>$M_1$ [diagram] $\psi\,M_1$<br><br>$-1 \le \psi \le 1$ | $\beta_{M,\psi} = 1.8 - 0.7\psi$ |
| Moments due to in-plane lateral loads<br><br>[diagram] $M_Q$<br><br>[diagram] $M_Q$ | $\beta_{M,Q} = 1.3$<br><br><br>$\beta_{M,Q} = 1.4$ |
| Moments due to in-plane lateral loads plus end moments<br><br>$M_1$ [diagram] $\Delta M$ $M_Q$<br><br>[diagram] $\Delta M$ $M_Q$<br><br>[diagram] $\Delta M$ $M_Q$<br><br>[diagram] $\Delta M$ $M_Q$ | $\beta_M = \beta_{M,\psi} + \dfrac{M_Q}{\Delta M}\left(\beta_{M,Q} - \beta_{M,\psi}\right)$<br><br>where<br><br>$M_Q = \lvert \max M \rvert$ due to lateral load only<br><br>and<br><br>$\Delta M = \begin{cases} \lvert \max M \rvert,\ \text{for moment diagram} \\ \qquad\qquad \text{without change of sign} \\[2em] \lvert \max M \rvert + \lvert \min M \rvert,\ \text{for moment diagram} \\ \qquad\qquad \text{with change of sign} \end{cases}$ |

Figure 2-1: Equivalent uniform moment factors

The applied loads according to Eurocode 3 should be acquired by EN 1991-1-2 which contains appropriate fire actions. The equivalent fire load is prescribed either according to parametric fire curves, leading to more cumbersome - although more representative - solution processes, or reflects the effects of the standard ISO 834 fire curve with initial/ambient temperature $\theta_0$ = 20°C which provides a more easily implemented approach. The fundamental load-bearing expression of Eurocode 3 demonstrates that the design effects of actions for the fire design situation $E_{fi,d}$ should be lower than the corresponding design resistance of a steel member for the fire design situation at time $t$ $R_{fi,d,t}$. Clause 4.2.3.6 of EN 1993-1-2 states that this expressions is deemed to be automatically satisfied for members with class 4 cross-sections other than tension members, if at time $t$ the steel temperature $\theta_a$ at all cross-sections is less than $\theta_{crit}$ = 350°C.

## 2.3   Direct Strength Method

The Direct Strength Method (DSM) was developed as an alternative approach to the standard effective width method contained in the AISI specification for the design of cold-formed steel structural members. This semi-analytical method utilizes the elastic critical buckling loads corresponding to local, distortional and global buckling modes to produce an estimation of the bearing capacity of the investigated member.  It does not contain either iterations/refinements nor effective cross-sectional properties. However, a numerical linear buckling analysis has to be performed in order to feed the DSM solution process with the elastic buckling loads. In addition, the applicability of this method includes limitations regarding the geometric and mechanical properties of the cross-section which are explicitly stated in the pertinent AISI specification. This clause will describe the load-bearing estimation process for columns subjected to axial compression by estimating the nominal strength for each buckling type and then integrate the solutions to derive the final estimation of the method.

**Global buckling**
Given the yield load $P_y$ and the elastic critical buckling load $P_{cre}$ corresponding to global buckling, i.e. flexural, torsional, flexural-torsional, the nominal axial strength $P_{ne}$ is calculated by:

$$P_{ne} = \left(0.658^{\lambda_C^2}\right) P_y \qquad\qquad \text{for } \lambda_C \leq 1.5 \qquad\qquad (2.37)$$

$$P_{ne} = \left(\frac{0.877}{\lambda_C^2}\right) P_y \qquad\qquad \text{for } \lambda_C > 1.5 \qquad\qquad (2.38)$$

where

$$\lambda_C = \sqrt{\frac{P_y}{P_{cre}}} \qquad\qquad\qquad\qquad\qquad\qquad (2.39)$$

**Local Buckling**
Given the elastic critical buckling load $P_{cr\ell}$ corresponding to local buckling and the previously calculated nominal axial strength $P_{ne}$, the nominal axial strength $P_{n\ell}$ for local buckling is obtained from:

$$P_{n\ell} = P_{ne} \qquad\qquad\qquad\qquad \text{for } \lambda_\ell \leq 0.776 \qquad\qquad (2.40)$$

$$P_{n\ell} = \left[1 - 0.15\left(\frac{P_{cr\ell}}{P_{ne}}\right)^{0.4}\right]\left(\frac{P_{cr\ell}}{P_{ne}}\right)^{0.4} P_{ne} \qquad\qquad \text{for } \lambda_\ell > 0.776 \qquad\qquad (2.41)$$

where

$$\lambda_\ell = \sqrt{\frac{P_{ne}}{P_{cr\ell}}} \qquad\qquad\qquad\qquad\qquad\qquad (2.42)$$

**Distortional Buckling**
Given the elastic critical buckling load $P_{crd}$ and the yield load $P_y$, the nominal strength for distortional buckling $P_{nd}$ is determined by:

$$P_{nd} = P_y \qquad\qquad \text{for } \lambda_d \leq 0.561 \qquad\qquad (2.43)$$

$$P_{nd} = \left[1 - 0.25\left(\frac{P_{crd}}{P_y}\right)^{0.6}\right]\left(\frac{P_{crd}}{P_y}\right)^{0.6} P_y \qquad\qquad \text{for } \lambda_d > 0.561 \qquad\qquad (2.44)$$

where

$$\lambda_d = \sqrt{\frac{P_y}{P_{crd}}} \qquad\qquad (2.45)$$

The design strength of the cold-formed steel column corresponds to the minimum nominal axial strength $P_{ne}$, $P_{n\ell}$ and $P_{nd}$ multiplied by the resistance factor $\varphi_C < 1$.

$$P_u = \varphi_C \min(P_{ne}; P_{n\ell}; P_{nd}) \qquad\qquad (2.46)$$

## 2.4 Previous Studies

This clause aims at presenting independent inquiries conducted by other researchers; thermal and structural modeling, failure locations, test specimens etc. are presented along with significant findings extrapolated by each pertinent study.

**Alfawakhiri and Sultan**

This study [77] presents an analytical approach to fire tests conducted by the National Research Council of Canada in collaboration with the North American steel industry. The analytical methodology focuses on reflecting the temperature and deformation results of the corresponding experimental investigation. Furnace tests are performed using six light-weight steel frame wall assemblies by imposing the standard ISO 834 fire curve. The examined formations were 3048mm high by 3658mm long comprising channel sections with flange stiffening lips and web perforations as load-bearing studs. Block and strap bridging type, optional resilient channels and ambient side cross-bracing are also used to provide additional stability (Figure 2-2). The steel members are sheathed in double-layered type X plasterboards from both sides while the air cavities are filled with thermal insulation in four out of six configurations.
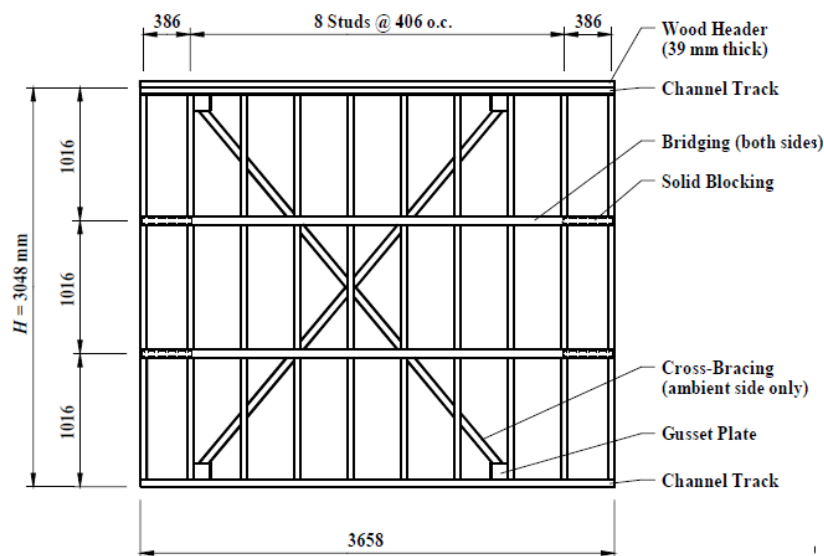


Figure 2-2: Typical steel frame fabrication layout for wall specimens [77]

Table 2-1: Summary of fire resistance tests on load bearing LSF walls

| Specimen number | Stud spacing (mm) | Insulation type (fiber) | Resilient channels on exposed side | Load including self-weight (kN/m) | Fall-off time of gypsum on exposed side (min) | | Structural failure time (mm) | Temperature rise on unexposed side, under pads, at failure time (°C) | |
|---|---|---|---|---|---|---|---|---|---|
| | | | | | Face layer | Base layer | | Maximum | Average |
| W1 | 406 | Glass | Yes | 21.5 | 50 | in place | 55 | 52 | 36 |
| W2 | 610 | Rock | Yes | 14.3 | 57 | 67 | 73 | 50 | 42 |
| W3 | 406 | Cellulose | Yes | 21.5 | 57 | in place | 70 | 42 | 37 |
| W4 | 406 | - | Yes | 21.5 | 58 | in place | 76 | 64 | 60 |
| W5 | 406 | Rock | Yes | 21.5 | 53 | in place | 59 | 37 | 26 |
| W6 | 406 | - | No | 21.5 | in place | in place | 83 | 76 | 69 |

All specimens failed due to structural inadequacy and neither heat penetration nor high ambient side temperatures took place. This study concludes that the use of thermal insulation has a negative effect on bearing capacity. Cavity insulation hinders heat transfer thus temperature differential across the member is increased while non-insulated layouts demonstrated much more uniform-type temperature gradients. The uninsulated formations failed at mid-height cold flange as a result of bending towards the furnace and the development of high compressive force on the ambient side. The insulated formations were characterized by near the support hot-flange failure, i.e. at the location of the first web perforation at 0.2*H*, while they exhibited bending away from the furnace. Furthermore, it is concluded that wider stud spacing increases the fire resistance rating of load-bearing drywall assemblies while resilient channels impair the structural performance because they do not allow the gypsum boards to stay in place.

**Chen and Young**

This study [78] investigates the behavior of cold-formed steel lipped channel columns at elevated temperatures. A numerical investigation is carried out using the finite element software ABAQUS [79] and is compared to the test results of Young and Rasmussen [80] at ambient conditions and to Feng et al. [81] at elevated temperatures. For each case, tensile coupon tests were performed by the corresponding experimental investigations to derive the 0.2% proof stress, the ultimate stress and the elasticity modulus. The simulation considered fix-end boundary conditions except for allowing axial translation of the end at which the load was applied and assumed imperfections after the 1st buckling mode, i.e. local buckling, with amplitudes equal to the cross-sectional thickness.
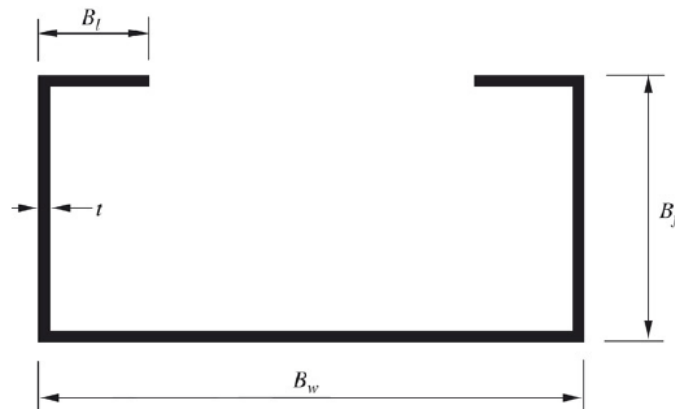


Figure 2-3: Section overview and symbol definition [78]

Table 2-2: Nominal cross-sectional dimensions for columns series

| Series | $B_\ell$ (mm) | $B_f$ (mm) | $B_w$ (mm) | $t$ (mm) |
|--------|-----------|-----------|-----------|---------|
| L36 | 12 | 36 | 96 | 1.5 |
| L48 | 12 | 48 | 96 | 1.5 |
| L50 | 15 | 50 | 130 | 1.5 |
| Lip12 | 15 | 54 | 100 | 1.2 |
| Lip2 | 15 | 56 | 100 | 2.0 |

Specimens with various lengths and flange widths were examined and compared to the relevant experiments. At ambient conditions, an average error of 3% was observed between numerical and experimental results for lower flange widths, whereas an average error of 7% occurred for higher flange widths. At elevated temperatures the average error was around 2% for every case, respectively.

After evaluating the test results, a parametric numerical study is demonstrated with column lengths starting from 280mm to 3000mm and flange widths of 36, 48 and 50mm, at different temperatures. Local imperfections amplitudes equal to the nominal thickness were considered and global buckling imperfection values equal to 1/1000 of the member's length. The parametric study is accompanied by analytical and semi-analytical methodologies based on the effective width (EWM) and the direct strength method (DSM) of the AISI specification. Both methods were modified to include the diminished material properties at elevated temperatures in order to be compared to the numerical model output. For the 36mm flange width series, both methods presented an average error of 7% with the direct strength method having slightly more dispersion. For the 48mm flange width series, the effective width approach deviated on average 27% whereas the DSM 22%. For the 50mm flange width case, the EWM had an average error of 14% whereas the DSM had 20%, respectively. In the next two figures, a graphical display of the coincidence between the finite element results and the effective width and direct strength method for the 48mm flange width series is presented.
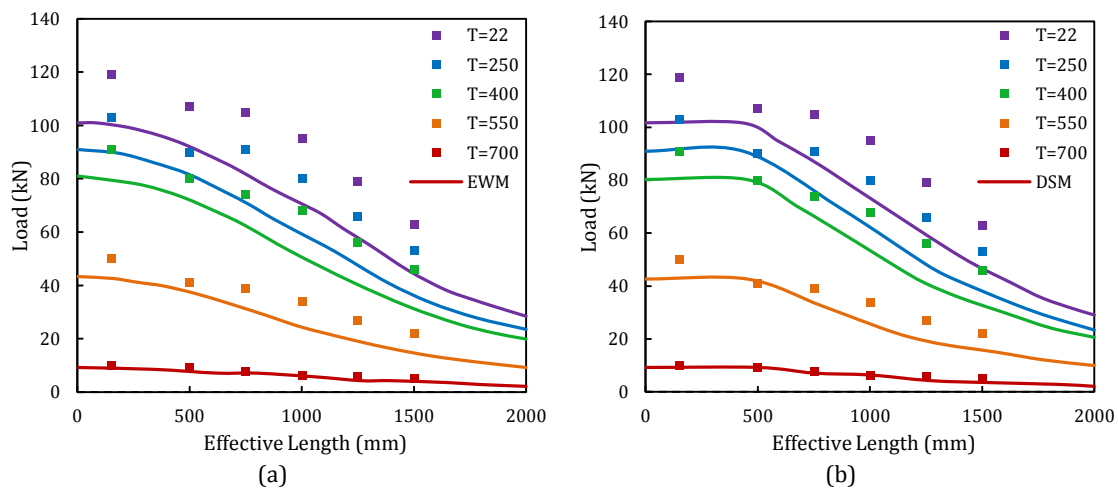


Figure 2-4: Numerical results compared to (a) EWM and (b) DSM predictions, for 48mm flange width [78]

**Ranawaka and Mahendran**

This investigation [82], [83] focuses on the distortional buckling behavior of short cold-formed steel columns at uniform elevated temperatures. More than 150 compression tests were carried out at channel sections with lip stiffeners (Type B) or without (Type A) and then compared to pertinent regulations. Three nominal thicknesses were considered for the examined cross-sections, namely 0.60, 0.80 and 0.95mm while flexural residual stresses following Schafer & Pekoz's findings [26] were adopted. Both low (G250) and high (G550) strength steels are examined with fixed-end boundaries and lengths in the range of 180 to 280mm. The column length was decided in order for global buckling not to take place whereas the cross-sectional dimensions are chosen to impede local buckling. These assumptions were validated via numerical calculations using both finite strip and finite element methods before the actual tests were undertaken. The reductions laws regarding mechanical property deterioration used in the numerical simulations were determined by a previous work of the authors [84]. The cross-sectional dimensions and the corresponding nomenclature are presented in Figure 2-5 and Table 2-3. Note that the third and fourth table columns denote the mean base metal thicknesses while the last column represents the specimen's net length, i.e. the length between the end plates.
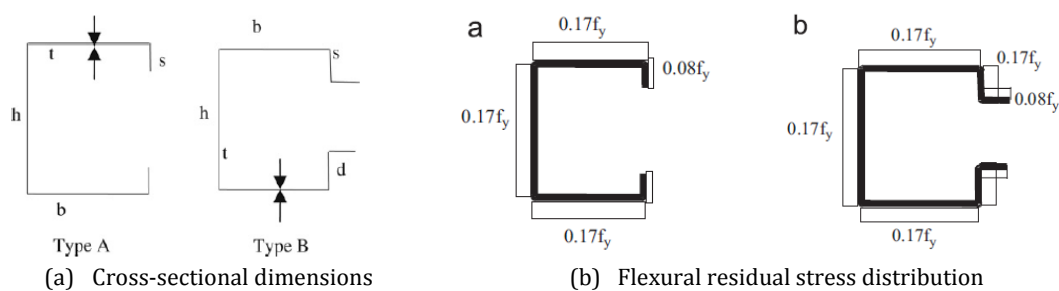


(a)  Cross-sectional dimensions                    (b)  Flexural residual stress distribution
Figure 2-5: (a) Dimensions of the cross-sections and (b) residual stress distribution

Table 2-3: Nomenclature of dimensions

| Section | Thickness (mm) | | | Section sizes (mm) | | | | Length (mm) |
|---------|---------|-----------|-----------|----|----|----|----|-------------|
|         | Nominal | BMT-G250  | BMT-G550  | h  | b  | d  | s  |             |
| Type A  | 0.60    | 0.54      | 0.60      | 30 | 30 | 5  | -  | 200         |
|         | 0.80    | 0.75      | 0.80      | 30 | 30 | 5  | -  | 180         |
|         | 0.95    | 0.94      | 0.95      | 30 | 35 | 5  | -  | 180         |
| Type B  | 0.60    | 0.54      | 0.60      | 40 | 30 | 5  | 10 | 280         |
|         | 0.80    | 0.75      | 0.80      | 40 | 30 | 5  | 10 | 240         |
|         | 0.95    | 0.94      | 0.95      | 40 | 30 | 5  | 10 | 220         |

To properly implement fixed-end conditions throughout the whole process, the end plates have a 5mm cavity filled with Pyrocrete 165 coil grout to provide enough lateral and rotational resistance. The furnace was heated at a rate of 10 to 20°C/min and its temperature was maintained constant for 20min so that each specimen could reach the same temperature. The specimens were allowed to expand freely during the heating process since no external loading was applied. Subsequently, a concentric compressive load was imposed using displacement control at a rate of 0.3mm/min. The total loading time was about an hour and thermal creep effects are assumed to be negligible for that duration.

Two main distortional buckling failure types were observed at ambient temperature, namely both flanges moving outwards or both flanges moving inwards. An additional failure type

unfolded at high temperatures where one flange would move outwards and the other inwards. Even though the failure modes of identical members at the same temperature occurred at the same ultimate loads, their failure type differentiated as a result of different initial imperfections. The use of members with relatively low non-dimensional slenderness, i.e. the square root of yield stress divided by the distortional buckling strength, provided infinitesimal post-buckling capacity, i.e. the ratio of the ultimate load to the elastic distortional buckling load. Specifically, for non-dimensional slenderness values between 1.0 and 1.5 the test results displayed a post-buckling capacity of 1.09 and 1.04 at ambient and elevated temperature conditions, respectively.



(a) Ambient temperature                                       (b) Elevated temperatures
Figure 2-6: Failure modes at different temperature conditions
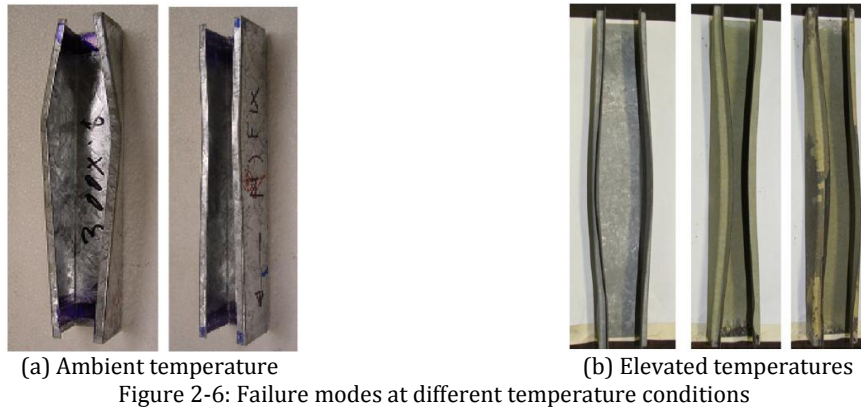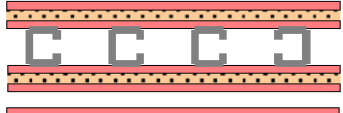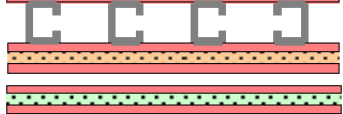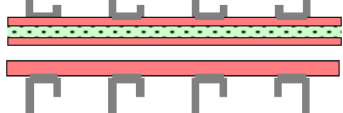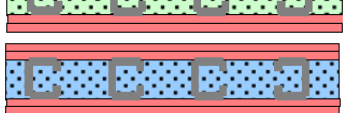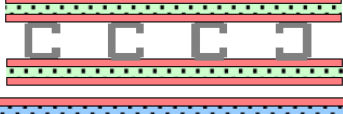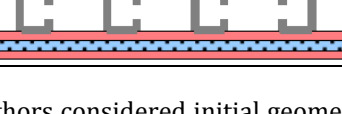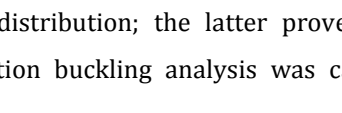
Another interesting trend was found regarding yield stress and elasticity modulus deterioration. Nominally identical specimens exhibited different reduction patterns regarding their mechanical properties. Furthermore, while it is assumed that low strength steels display higher ductility than high strength steels, this study revealed the exact opposite. The ductility was measured as the ratio of the displacement $\delta_u$, corresponding to 85% of the ultimate load in the descending path, to the yield displacement $\delta_y$, corresponding to the shifting point between the initial linear response path and the following non-linear path. The observed ductility fall in the range of 1.23-1.48 and 1.64-6.80 for G250 and G550 steel specimens, respectively. Load bearing capacity reduction with respect to temperature for both steels, thicknesses and lips stiffeners (Type B) or without (Type A) are plotted in the next figure.



(a)   Type A                                      (b)   Type B
Figure 2-7: Ultimate loads versus temperature curves
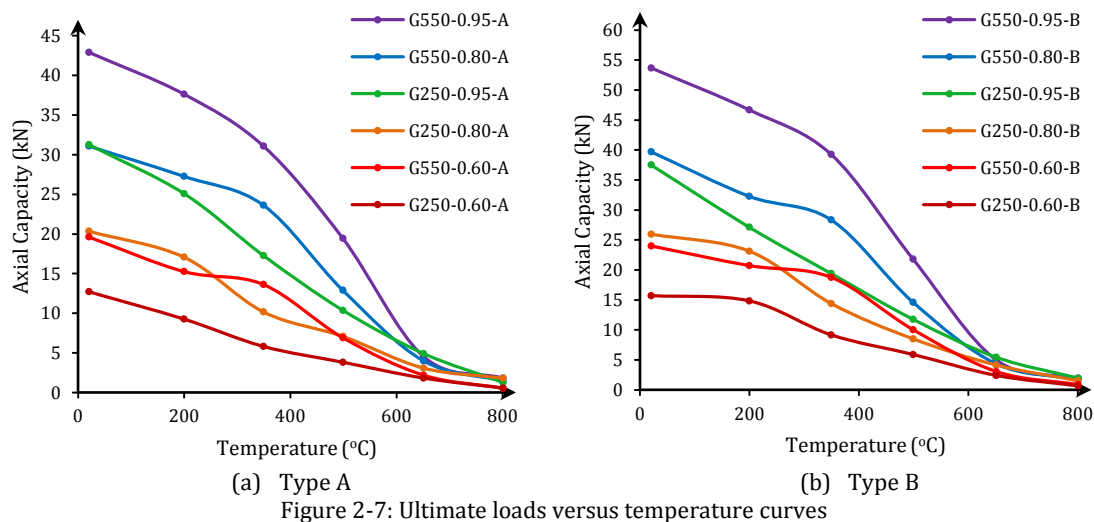
**Gunalan, Kolarkar and Mahendran**

This research is based on the work performed at the Ph.D theses of Dr. Gunalan S. [44] and Dr. Kolarkar P. [85] at Queensland university of Technology in Australia under the supervision of Professor Mahendran M. The findings of these inquiries resulted in several publications [1], [86], [87], [88], [89]. The authors examined in general seven load-bearing wall assemblies comprising cold-formed lipped channel sections and plasterboard layers as cladding. The investigation includes experiments on all test specimens accompanied by numerical evaluation using the commercial finite element software ABAQUS. The results of the linearized buckling analysis were also cross-checked by CUFSM. The provisions of Eurocode 3, AISI's direct strength method and AS/NZS 4600 are also used in most cases to validate the numerical and experimental solutions. The specimens contain the standard cladding with one gypsum plasterboard layer and in some cases cavity insulation, whereas a new approach, based on double plasterboard layers and thermal insulation sandwiched between them, is proposed.

Table 2-4: LSF wall specimens

| Test | Configuration | Insulation | Load Ratio | Test failure time (min) |
|------|---------------|------------|------------|-------------------------|
| 1 |  | Glass fiber | 0.2 | 118 |
| 2 |  | Glass fiber | 0.4 | 108 |
| 3 |  | Rock fiber | 0.4 | 134 |
| 4 |  | None | 0.2 | 53 |
| 5 |  | None | 0.2 | 111 |
| 6 |  | Glass fiber | 0.2 | 101 |
| 7 |  | Rock fiber | 0.2 | 107 |
| 8 |  | Cellulose fiber | 0.2 | 110 |
| 9 |  | Rock fiber | 0.2 | 136 |
| 10 |  | Cellulose fiber | 0.2 | 124 |

The authors considered initial geometric imperfections after various sources along with residual stress distribution; the latter proved to have negligible effects on the final behavior. The bifurcation buckling analysis was carried out using different flange restraints to check the

prevention of minor axis flexural buckling and flexural-torsional buckling of the load-bearing studs. The corresponding tests concluded that the plasterboards were able to provide sufficient resistance against those two buckling types even at very high temperatures, while the bifurcation buckling analysis provided identical elastic critical buckling loads for the cases of: i) continuous restraining against the lateral movement of the middle node of each flange, ii) repeated lateral restraints at regular intervals. Each stud was modeled as pin-supported at the remote end while axial displacement was allowed at the end were the axial load was imposed. The furnace operated in order to generate the standard ISO 834 fire curve.

Aiming at comparing the numerical and experimental findings to analytical estimations, an idealized non-uniform temperature profile is considered. Constant temperature value is assumed at each flange and lip while a linear temperature variation is assumed at the section's web. The dimensions of the cold-formed studs comprise 90mm depth, 40mm width and 15mm lip length. Three modes are adopted to input initial geometric imperfections during the non linear analyses. The first one is the critical mode resulting from the bifurcation buckling analysis which in this case reflects local web buckling. The second mode corresponds to analyzing the stud with the deteriorated material properties based on the temperature of the hot flange. Finally, the third mode was determined by considering the temperature-related mechanical properties across the section following the idealized temperature profile. Nevertheless, at elevated temperatures each imperfection input resulted in the same maximum load as a result of the predominant effect of thermal bowing, neutral axis shift and their magnification effects.

In the temperature domain, axial strength reduction curves displayed almost identical paths when plotted as a function of the maximum cross-sectional temperature. This fact advocates the use of the maximum member temperature as the most proper temperature aspect to evaluate the structural performance at elevated temperatures. Furthermore, the use of cavity insulation seems to have a negative impact on the structural performance as it does not provide protection to the hot flange whose failure dominates the response at temperatures higher than approximately 500°C; externally insulated wall panels presented the best performance. It is also observed that lining formations does not affect the structural response but mostly delay the temperature rise. Failure is likely to occur either at the ambient side of the section at mid-height or at the fire side near the support.

The application of a vertical compressive load causes a shift of the centroidal axis of the cross-section as the steel panels begin to exhibit local buckling phenomena. The major axis shifts towards the ambient side and a bending moment is created generating additional compression at the hot flange and tension at the cold flange. At the same time, the temperature gradient deforms the member causing it to globally buckle towards the fire; hence, creates compression at the cold-flange and tension at the hot-flange. Considering the reduced mechanical properties at the fire side as a result of higher temperature escalation, the authors conclude that the hereinbefore mentioned failure locations are likely to occur.

In another investigation performed by Gunalan et al. [90], the use of AS/NZS 4600 and Eurocode 3, part 1.3 is validated when predicting the behavior of lipped channel sections undergoing flexural-torsional buckling. The examination considered both ambient and uniform elevated temperature conditions as well as simple and rigid boundary conditions. Finite element analyses and test results are utilized to evaluate the consistency of the pertinent regulations. The details of the investigated members are displayed in Table 2-5.

Table 2-5: Test specimen details

| Steel Grade | $f_y$ (MPa) | $E$ (GPa) | Nominal thickness (mm) | Measured BMT (mm) | Section dimensions (mm) | | | Specimen length (mm) | |
|---|---|---|---|---|---|---|---|---|---|
| | | | | | Web | Flange | Lip | Series 1 | Series 2 |
| G550 | 615 | 205 | 0.95 | 0.95 | 55 | 35 | 9 | 1800 | 2800 |
| G250 | 271 | 188 | 1.95 | 1.95 | 75 | 50 | 15 | 1800 | 2800 |
| G450 | 515 | 206 | 1.90 | 1.88 | 75 | 50 | 15 | 1800 | 2800 |

The authors discovered that the warping fixity, conservatively neglected during calculations, enhanced significantly the ultimate bearing capacity. However, it is not considered in the corresponding specifications. Hence, Gunalan & Mahendran [91] proposed a new set of equations to fix the experimental results to a matching formula. These proposed equations are also compared to the finite element results along with the EN 1993-1-2, the modified EN 1993-1-3 and the AS/NZS 4600 predictions regarding fix-ended columns.

At ambient temperature (20°C), the proposed equations demonstrated the best coincidence compared to the specification provisions; Eurocode methods provided the highest deviation from the FEA. It appeared that the use of buckling curve "b" regarding lipped channel section is too conservative and the test results matched with curve "a$_o$". The mean offset and the coefficient of variation at each temperature for every approach are summarized in the next table.

Table 2-6: FEA results compared to various approaches

| Temperature | FEA/AS 4600 | | FEA/proposed eq. | | FEA/EN 1993-1-3 | | FEA/EN 1993-1-2 | |
|---|---|---|---|---|---|---|---|---|
| | Mean | COV | Mean | COV | Mean | COV | Mean | COV |
| 20 °C | 1.225 | 0.152 | 1.009 | 0.046 | 1.338 | 0.105 | 1.388 | 0.171 |
| 100 °C | 1.237 | 0.153 | 1.007 | 0.046 | 1.344 | 0.107 | 1.503 | 0.068 |
| 200 °C | 1.258 | 0.156 | 1.008 | 0.045 | 1.360 | 0.111 | 1.514 | 0.069 |
| 300 °C | 1.268 | 0.169 | 1.014 | 0.046 | 1.363 | 0.121 | 1.531 | 0.067 |
| 400 °C | 1.148 | 0.245 | 0.926 | 0.094 | 1.238 | 0.203 | 1.388 | 0.118 |
| 500 °C | 1.113 | 0.194 | 0.940 | 0.064 | 1.213 | 0.156 | 1.390 | 0.084 |
| 600 °C | 1.033 | 0.027 | 0.974 | 0.040 | 1.139 | 0.041 | 1.397 | 0.044 |
| 700 °C | 1.032 | 0.037 | 0.965 | 0.024 | 1.146 | 0.054 | 1.386 | 0.051 |

The same authors proceeded in an investigation [92] on failure due to local buckling of lipped and un-lipped channel sections (see Table 2-5 regarding steel grade and thickness) at ambient and uniform elevated temperatures. Test results were accompanied by finite element analysis and analytical and semi-analytical calculations according to relevant regulations. Specifically, the following methods are utilized to evaluate the experimental and numerical results: i) Direct strength method, ii) official Eurocode 3 part 1.2 method, iii) modified Eurocode 3 part 1.3 method, iii) AS/NZS 4600 methodology (identical to AISI S100), and iv) BS 5950 part 5. The results are summarized in the next figures.
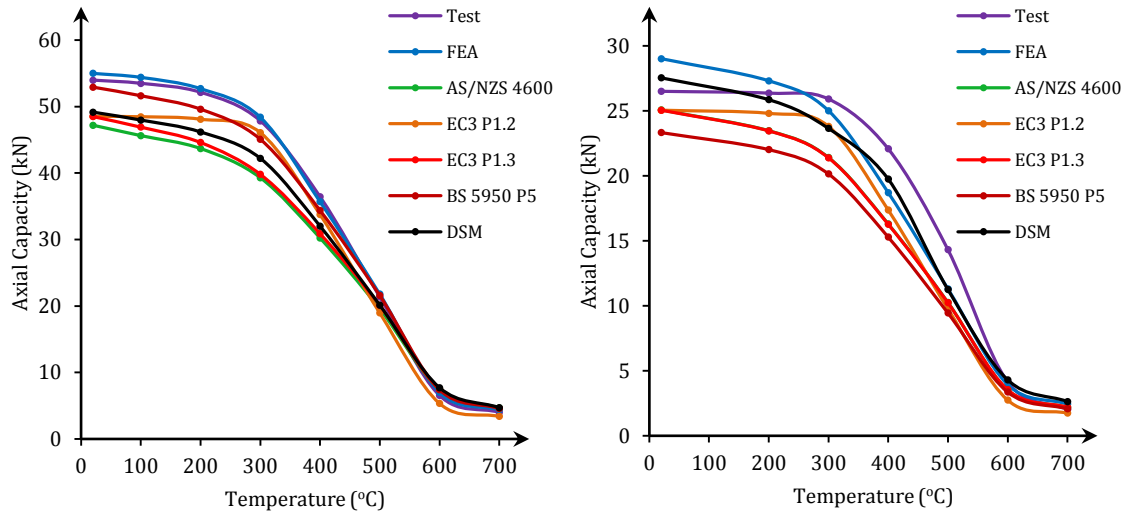
(a) G550/t=0.95mm/Lipped  (b) G550/t=0.95mm/Unlipped
Figure 2-8: Axial capacity deterioration for G550 steel at uniform temperature profiles
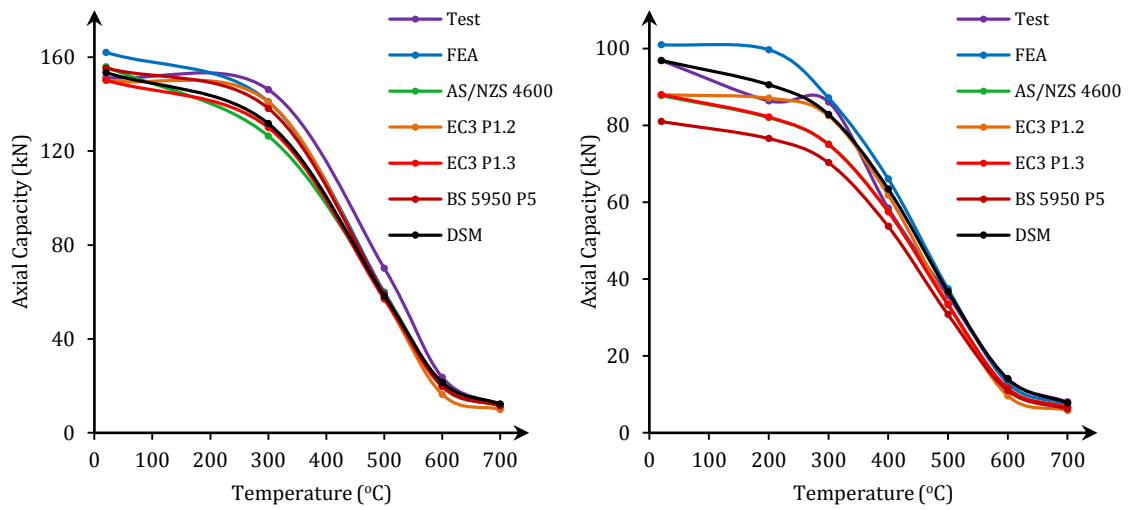


(a) G450/t=1.90mm/Lipped  (b) G450/t=1.90mm/Unlipped
Figure 2-9: Axial capacity deterioration for G450 steel at uniform temperature profiles
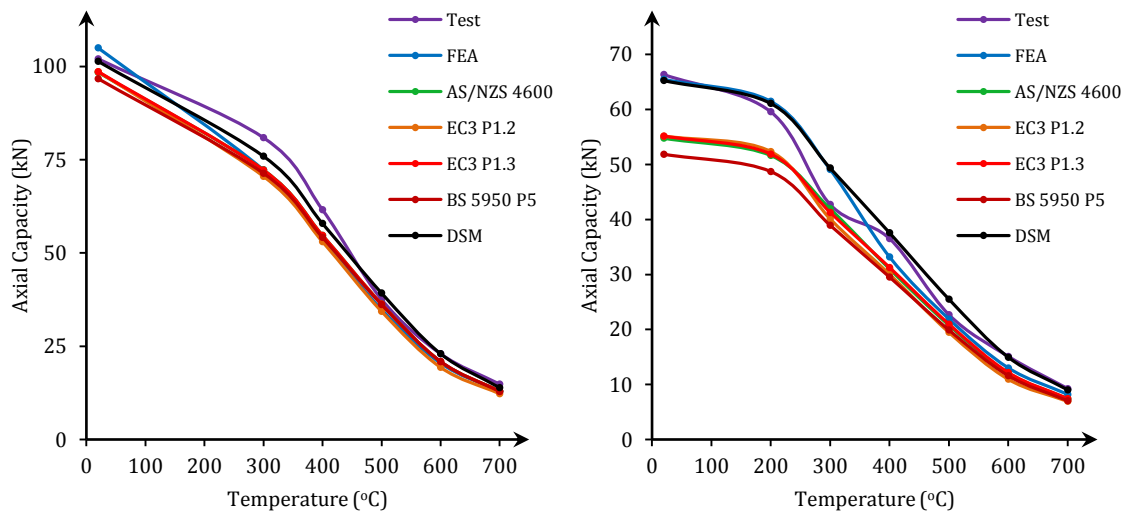


(a) G250/t=1.95mm/Lipped  (b) G250/t=1.95mm/Unlipped
Figure 2-10: Axial capacity deterioration for G250 steel at uniform temperature profiles

**Ariyanayagam and Mahendran**

The use of thermoplastic materials in modern structures led into the necessity to develop realistic fire curves. The phases of such fires differ substantially from the standard ISO 834 fire curve that is widely employed during furnace tests (see also §1.4.3). This publication [93] aims at revealing the strength reduction patterns unraveling after exposing load bearing drywall systems to realistic design fire curves. Both full scale fire tests and numerical studies using ABAQUS are carried out under transient and steady state conditions. Temperature to time curves are determined by Eurocode 1 part 1.2 [69] and Barnett C. R. (BFD) [94] and are graphically displayed in Figure 2-11; the dimensions of the lipped channel sections used as load bearing members are 90×40×15×1.15mm fabricated by G500 steel.
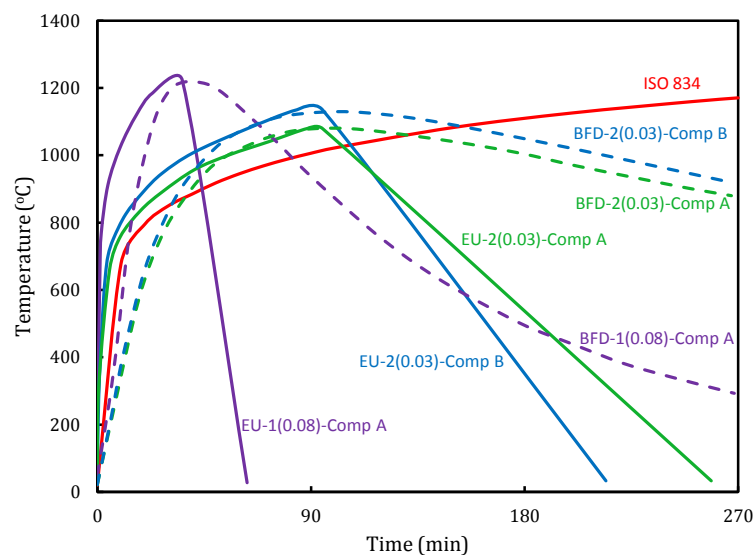


Figure 2-11: Employed fire curves [93]

Test specimens consisted of cold-formed studs sheathed in single gypsum plasterboard layers or double plasterboard layers. The new design regarding externally insulated drywalls is also considered using Rock fibers as thermal insulation material; no simulation of cavity insulated formation took place. In the numerical model, uniform temperature is assumed at each steel panel of the section except for the web where a linear variation is considered. Each drywall specimen consists of four steel studs which are fixed to the top and bottom tracks though screws placed on the flange mid-width. This connection type is conservatively assumed as pin. Screws are centered at 300mm restraining the out-of-plane deflection of each stud. The mechanical properties of the steel members derived from tensile coupon tests while their deterioration at elevated temperatures is estimated by the equations of Dolamune Kankanamge & Mahendran [57] while the thermal elongation is determined by the equations of Eurocode 3 part 1.2. The constitutive stress-strain laws follow the Ramberg-Osgood model with modified parameters suggested by Ranawaka & Mahendran [95]. The shape of the first eigenmode was employed to input the initial geometric imperfections. Depending on the buckling type of the first mode, imperfection amplitude of $0.006b$ was used for critical mode corresponding to local buckling,

with *b* being the panel width and a value $L/1000$ was used for critical global buckling mode, with *L* being the stud length; residual stresses are not considered.

Overall, the finite element results agreed well with the fire test results regarding axial and lateral displacements. A discrepancy was observed in the mid-height deflections near failure, attributed to potential loading eccentricity resulting from thermal bowing that caused different wall failure directions. Furthermore, some cases displayed different failure locations. Due to thermal bowing in the fire tests, the central part of the stud approaches the furnace wall thus increasing its temperature disproportionally compared to the other areas of the member. As a result, the hot-flange mid-height becomes more susceptible to failure and can display earlier failure than the hot-flange near the support which reflects the expected failure location at high elevated temperatures. On the other hand, this fact is not modeled in the finite element analysis whose results predicted a failure of the hot-flange near the end supports.

In addition, some single walled panels experienced an unexpected fall-off of a plasterboard strip and became vulnerable to flexural-torsional buckling which inevitably was their failure pattern. During transient finite element analysis, plasterboards provided continuous lateral restraints against flexural-torsional and minor-axis buckling resulting in a lack of coincidence between the two methods. However, when the same stud was modeled in steady-state FEA excluding the lateral restraints the output matched the test results. To check whether plasterboard fall-off occurred before stud failure, steady-state simulations were performed for all the above test cases concluding that local crushing of some studs caused the plasterboard failure. Therefore it is reasonable to assume that plasterboards provide adequate lateral restraints during the whole duration of the fire.

The maximum temperature of the cross-section, i.e. the temperature of the exposed flange, can be accurately used to predict the axial strength reduction. Hot-flange temperatures at failure agreed reasonably well for different load ratios and also coincided with standard furnace tests that were performed at [88]. The use of realistic fire design curves and different wall formations only affects the fire resistance rating of each assembly. Time domain reflects the resulting FRR for each case, but it is the temperature domain that provides the substantial information regarding the thermal performance of each configuration.

**Landesmann and Camotim**
This study [96] presents a thorough numerical investigation in order to assess the prediction accuracy of the current direct strength method distortional buckling curve. The authors performed compression tests on fix-ended cold-formed lipped channel (L) and rack sections [R] at ambient and uniform elevated temperatures. Aiming at identifying the importance of temperature-dependence in mechanical property deterioration, six different steel constitutive laws are employed to feed the finite element software ANSYS [63] which was used to perform linear and non-linear buckling analyses with initial geometric imperfections. Imperfections are inserted using the critical distortional mode using 10% of the nominal thickness as amplitude.

Initial bifurcation buckling analyses were performed to ensure distortional buckling susceptibility against local/global buckling of the selected columns using GBTUL [97]; residual stress distribution is not considered. The six constitutive material laws and mechanical properties erosion patterns included are: i) Eurocode 3 Part 1.2 regarding hot-rolled sections (HR), ii) Eurocode 3 Part 1.2 regarding cold-formed sections (CF), iii) Lee et al. (LMM) [98], iv) Chen and Young (CY) [99], v) Ranawaka and Mahendran (RM) [95] and vi) Wei and Jihong (WJ) [100]. The deterioration of yield stress and elasticity modulus along with the corresponding constitutive stress-strain relationships are addressed in detail in the original publication of each author; a graphical display of the reduction patterns for the mechanical properties is depicted in the next figure.
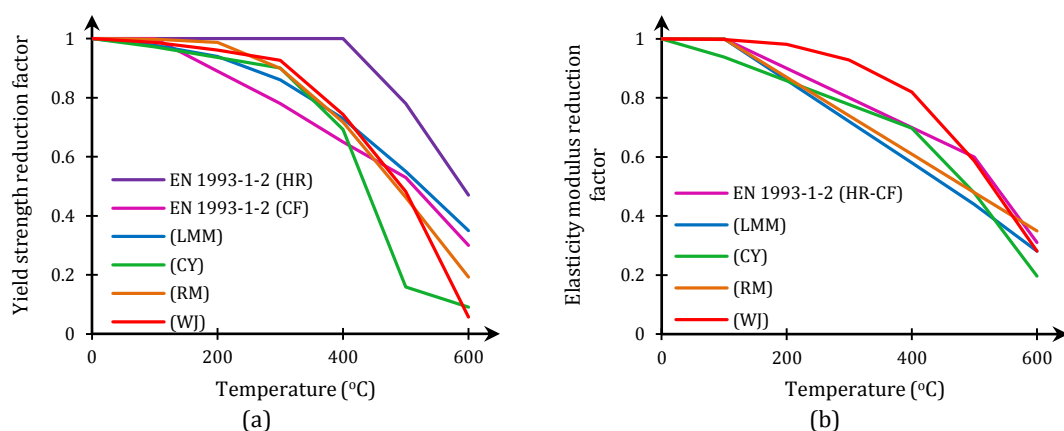


Figure 2-12: Employed temperature-variation models for (a) yield stress and (b) elasticity modulus [96]

The constitutive stress-strain laws demonstrate gradual yielding type except for the classical EN 1993-1-2 curve regarding hot-rolled sections. Most of the other experimental studies incorporate Ramberg-Osgood type models with modified parameters $\beta$ and $n_T$. Additionally, each model utilizes the reduction laws of yield stress and Young's modulus proposed by each researcher. Each inquiry considers different strain level corresponding to the nominal yield point. Thus, no explicit comparison is available in terms of discrete stress-strain points and the graphical representation of each curve is needed. For example, Eurocode 3 uses the 2% absolute strain to mark the yielding point of hot-rolled sections whereas considers the 0.2% residual strain for cold-formed sections. Hence, most experimental studies conservatively consider the 0.2% proof stress as the yielding point to which the reduction factors at elevated temperature apply.

For each case considered, various non-linear analyses were carried out for different distortional slenderness values. The results are plotted along with the predictions of the official direct strength method curve and a modified DSM curve (Figure 2-13) that increases the prediction accuracy regarding the current numerical solutions. The authors proposed the use of a modified official distortional buckling curve of the DSM differentiating for temperatures above or below 300°C. The DSM distortional buckling curve is represented by equations (2.43) and (2.44) while the modified relationship is presented in the next equations.

$$P_{n,D,T} = P_{y,T} \qquad\qquad\qquad\qquad\qquad\qquad\text{for } \bar{\lambda}_{D,T} \leq c \qquad\qquad (2.47)$$

$$P_{n,D,T} = P_{y,T}\left[a - 0.15\left(P_{cr,D,T}/P_{y,T}\right)^b\right]\left(P_{cr,D,T}/P_{y,T}\right)^b \qquad \text{for } \bar{\lambda}_{D,T} > c \qquad (2.48)$$

where $P_{n,D,T}$ is the prediction value of the method regarding the distortional axial strength at temperature $T$, $P_{y,T}$ is the yield load at temperature $T$, $P_{cr,D,T}$ is the elastic critical distortional buckling load and $a$, $b$ and $c$ are parameters whose values are displayed in the next table.

Table 2-7: Values for the parameters $a$, $b$, $c$ of the modified DSM distortional prediction curve

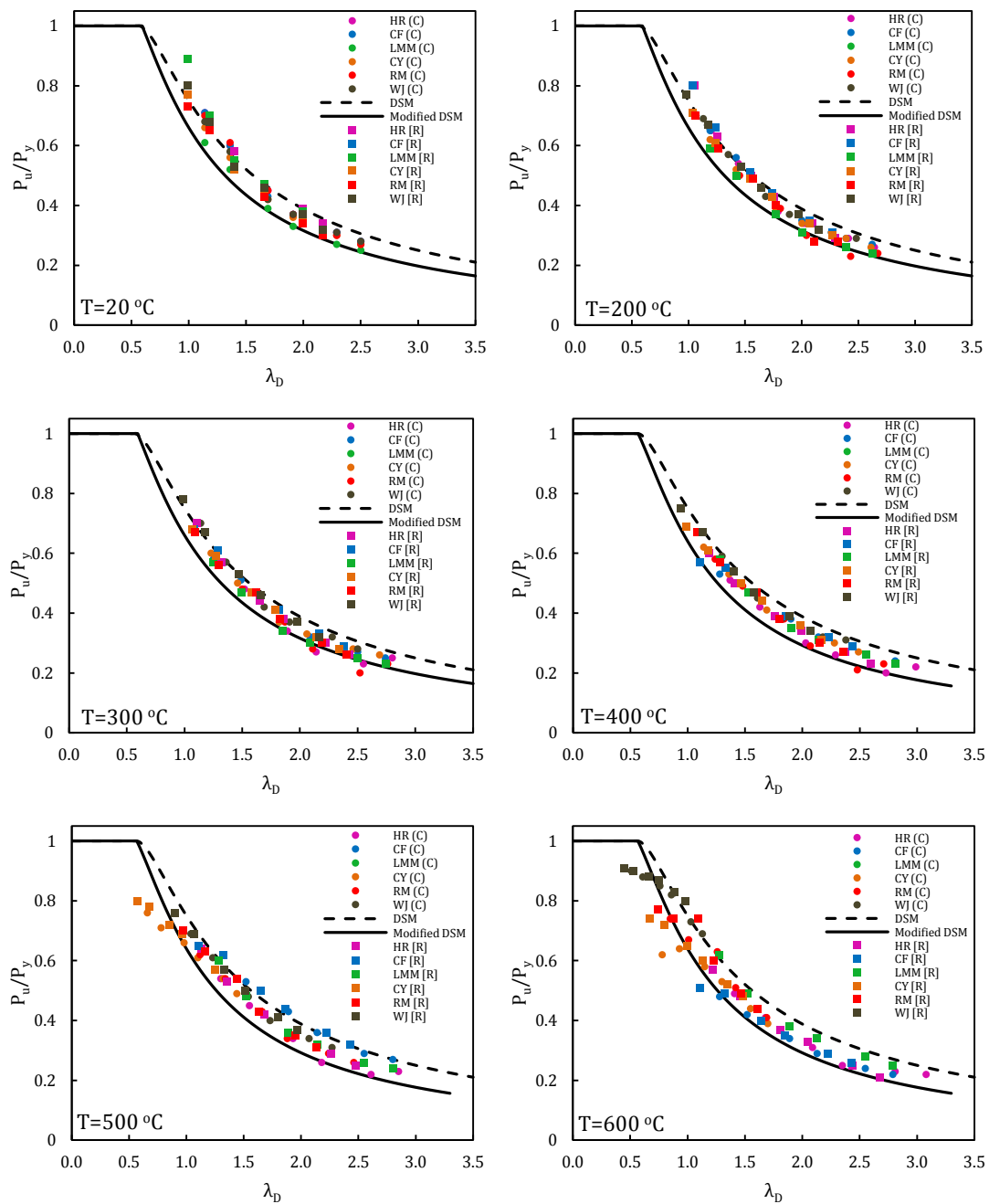| Variable | Temperature | |
|---|---|---|
| | ≤300°C | >300°C |
| $a$ | 0.810 | 0.790 |
| $b$ | 0.660 | 0.660 |
| $c$ | 0.594 | 0.567 |



Figure 2-13: Comparison between current/proposed DSM predictions and numerical results [96]

It is clear that the vertical dispersion of the plotted points in the previous graphs is quite consistent, considering the use of different material constitutive laws and reduction models while all points display a similar reduction trend. Two exceptions are sorted out from the previous statement: i) the stocky columns analyzed with the Chen & Young model at $T$=500-600 ℃ and ii) the stocky columns analyzed with the Wei & Jihong method at $T$=600 ℃. As a result, the main objective of the current study, to identify the importance of selecting different constitutive stress-strain models, was deemed satisfied after observing that no matter what method was chosen the results displayed relatively low dispersion and similar trends.

In general, the current DSM distortional buckling curve displayed similar reduction pattern with the numerical data for increasing slenderness values. The accuracy of the method demonstrated incremental decrease for higher slenderness values and higher elevated temperatures. To be more specific, the DSM predictions were slightly unsafe for $\bar{\lambda}_{D,T} < 1.5$ and $T < 400℃$ and became progressively more unsafe for higher slenderness and temperature values while they were too unsafe for the exceptions mentioned in the previous paragraph. The modified DSM curve incorporates a more steep initial reduction path to better fit the numerical output at low slenderness and its parameters differentiate for temperatures above 300℃ to match the previous dispersion at higher temperatures. The predicted to numerical ultimate loads for the current DSM curve had a 1.04-1.13 mean and 0.08-0.10 standard deviation whereas the corresponding results of the modified DSM curve demonstrated 0.86-0.93 and 0.05-0.11 values, respectively.

**Feng and Wang**
Feng and Wang [101] utilized the energy theorem to determine an analytical solution for the prediction of the lateral deflection and failure times of cold-formed thin-walled steel channel columns at non-uniform elevated temperatures. The close-formed solutions are then compared to the results of six full-scale furnace tests of cold-formed thin-walled structural steel panels under a concentric axial load and fire conditions from one side. The publication emphasizes the importance of properly capturing thermal bowing-related deflections and investigates the necessity to additionally consider neutral axes shift and corresponding magnifications. Overall, a comparison between EN 1993-1-2 method and a modified EN 1993-1-3 method is performed in order to evaluate the consistency of each method.

When a steel member is exposed to non-uniform temperature distributions across its length, transverse extensions force the member to bend towards the fire side; this temperature-related bending is call thermal bowing. This lateral deflection combined with the axial compressive load will generate a bending moment mainly about the major axis. The reduced stiffness at elevated temperatures resulting from the deteriorated elasticity modulus along with the axial load will amplify the lateral deflections even more causing the so-called magnified thermal bowing. On top of that, the initiation of buckling at the middle parts of some panels of the cross-section will reduce the available stiffness even more causing a shift of the neutral axes. This shift is highly affiliated with the non-uniform temperature distribution as the temperature gradient tampers

with the Young's modulus. The authors examined both major and minor axis shifting to account for bi-axial bending conditions. Identification of these phenomena prompted the authors to examine whether pure thermal bowing deflections should be considered, risking unsafe solutions, or the time-consuming calculations of the magnified thermal bowing deflections should be included as well.

Two lipped channel sections with nominal length 2000mm are considered and cross-sectional dimensions 100×54×15×1.2 or 100×56×15×2mm. During the fire tests, each panel comprised three studs centered at 750mm with two web perforations, one near the top end and one near the bottom support; the studs are simply supported at both ends, sheathed in gypsum plasterboards. The plasterboards and the stud are fixed using screws centered at 300mm. The mechanical properties of the two sections were determined by tensile coupon tests performed at ambient temperatures and the results are presented in the next table.

Table 2-8: Mechanical properties obtained from tensile coupon rests

| Stud Section | Mean yield strength $f_y$ (N/mm²) | Mean tensile strength $f_u$ (N/mm²) | Mean elastic modulus $E$ (N/mm²) |
|---|---|---|---|
| Lipped 100×54×15×1.2 | 393.4 | 507.9 | 184.4 |
| Lipped 100×56×15×2.0 | 353.4 | 497.4 | 203.1 |

The infinitesimal temperature variation taking place at the flanges combined with the repeated screws every 300mm establishes a weak regime regarding thermal bowing deflections in the plane of the flanges; hence, thermal bowing deflections are considered only in the plane of the web (major bending axis).

The maximum (mid-height) lateral deflection of a simply supported column exposed at non-uniform temperature distributions is:

$$\delta_{max} = \frac{\alpha \Delta T L^2}{8 b_w} \tag{2.49}$$

where $a$ is the coefficient of thermal expansion; $\Delta T$ is the temperature difference across the section; $L$ is the member length; $b_w$ is the depth of the cross-section.

The corresponding deflection curve is given by:

$$v_o = -\frac{\alpha \Delta T}{2 b_w} z^2 + \frac{\alpha \Delta T L}{2 b_w} z \tag{2.50}$$

where $z$ stands for the longitudinal axis of the stud.

Assuming that the additional lateral deflection due to the magnified thermal bowing $v_1$ follows a parabolic trend in the form of $v_1 = az^2 + bz + c$ and that the total lateral deflection, considering the shift of the major axis $e_y$, is determined as: $y = v_o + v_1 - e_y$, after taking into account the boundary conditions and the axial load $P$ the total lateral deflection curve becomes:

$$y = -\frac{\frac{2\alpha\Delta T}{3b_{\mathrm{w}}}PL}{\frac{16}{L^3}EI - \frac{4}{3L}P}\left(\frac{z^2}{L^2} - \frac{z}{L}\right) - \frac{\alpha\Delta T}{2b_{\mathrm{w}}}z^2 + \frac{\alpha\Delta TL}{2b_{\mathrm{w}}}z - e_{\mathrm{y}} \tag{2.51}$$

The maximum deflection at mid-height $z$=L/2 equals:

$$y_{\mathrm{max}} = -\frac{\frac{2\alpha\Delta T}{3b_{\mathrm{w}}}PL}{\frac{64}{L^3}EI - \frac{16}{3L}P} + \frac{\alpha\Delta TL^2}{8b_{\mathrm{w}}} - e_{\mathrm{y}} \tag{2.52}$$

where $E$ is the average reduced elasticity modulus across the section and $I$ is the weighted average second moment of area given by:

$$I = \sum_{i=1}^{q} n_{\mathrm{i}}[I_{\mathrm{i}} + A_{\mathrm{i}}x_{\mathrm{i}}^2] \tag{2.53}$$

where the cross-section is divided into $q$ segments and each one has an area of $A$, a distance $x$ from the centroidal axis under the non-uniform temperature distribution considered and a value $n_{\mathrm{i}}$ determined from:

$$n_{\mathrm{i}} = \frac{\text{The reduced elastic modulus at temperature } T_{\mathrm{i}}}{\text{Weighted average elastic modulus of the section}} \tag{2.54}$$

While Eurocode 3, part 1.2 suggests the use of the effective cross-section calculated at ambient temperatures, the authors proposed a "modified" Eurocode 3, part 1.3 methodology where an effective cross-section is calculated for each temperature profile. Even though, this process is cumbersome and requires heavy computational effort, the finally proposed equations take the form:

$$\frac{P}{\chi_{\mathrm{min}}N_{\mathrm{eff}}} + \frac{k_{\mathrm{x}}(M_{\mathrm{x}} + \Delta M_{\mathrm{x}})}{M_{\mathrm{x,eff}}} + \frac{k_{\mathrm{y}}(M_{\mathrm{y}} + \Delta M_{\mathrm{y}})}{M_{\mathrm{y,eff}}} \leq 1.0 \tag{2.55}$$

$$\frac{P}{\chi_{\mathrm{lat}}N_{\mathrm{eff}}} + \frac{k_{\mathrm{LT}}(M_{\mathrm{x}} + \Delta M_{\mathrm{x}})}{\chi_{\mathrm{LT}}M_{\mathrm{x,eff}}} + \frac{k_{\mathrm{y}}(M_{\mathrm{y}} + \Delta M_{\mathrm{y}})}{M_{\mathrm{y,eff}}} \leq 1.0 \tag{2.56}$$

where $N_{\mathrm{eff}}$ is the axial bearing capacity at elevated temperatures; $M_{\mathrm{x,eff}}$ and $M_{\mathrm{y,eff}}$ are the bending moment capacities at non-uniform elevated temperatures about the major and minor axis, respectively.

After comparing the proposed equations with the test results it was concluded that the consideration of thermal bowing deflection is substantial for the accurate prediction of the corresponding fire effects; however, the magnification effects need not be considered. Furthermore, EN 1993-1-2 method gives slightly less accurate results than EN 1993-1-3 modified method, but its solution process is much easier to implement. The minor axis shift can be completely ignored. Including the major axis shift can change the failure location from mid-height cold flange to support hot-flange, but incorporating this shift seemed to cause further deviation from the test results. Finally, the authors state the need to develop alternative elevated temperature approaches because the current methods are extremely complex.

# 3 Evaluation of Structural Response at Ambient Temperature

## 3.1 Introduction

The methodology of estimating the fire-resistance of any steel member starts by understanding the behavior during pre-fire conditions. An axially compressed steel member can barely reach its maximum axial resistance ($A \times f_y$) since global buckling is likely to occur. However, in thin-walled members, axial compressive strength diminishes even more rapidly due to development of local/distortional buckling. Evaluating the buckling performance of such a member by exploring its inherent buckling tendencies and identifying the post-buckling regime is the scope of this chapter.

A finite element model is developed in ADINA software [102] to simulate the member under investigation. Various mesh densities are tested in order to conclude to the most efficient in terms of both precision and computational effort. In each case, the member is subjected to a concentric vertical compressive load, imposed at the gravity center of the gross cross-section. On the way of obtaining the elastic critical buckling loads of different modes, a linearized buckling analysis is performed. A selection is made among those modes in order to target the ones that seem to have the most unfavorable effect on the member's response. Since these critical modes cannot be identified directly and there is no specific rule to aid in this selection, assumptions and tests have to be made to determine them. To validate the results obtained from the finite element model, a finite strip analysis is carried out using the freely available software CUFSM [103].

Next, a series of analyses is performed using various geometric imperfection values. Residual stresses are not considered since recent researchers [43], [104], [56], [44] found their contribution to be rather insignificant. Imperfections are used as input in the finite element model to reflect the initial deformed shape. The magnitude of these imperfections may significantly influence the strength of the stud under consideration. Moreover, different strength reduction patterns may unravel by increasing imperfection values in different modes. Choosing imperfection values for local, distortional and global buckling is usually consistent with scientific experiments and proposed formulas from credible sources. Nevertheless, mode susceptibility to imperfection increments varies, depending on buckling type. Past inquiries have revealed that distortional buckling modes are more prone to higher strength reduction patterns with increasing imperfection values as opposed to local buckling modes.

Finally, analytical calculations are executed to validate the consistency of the output of the numerical model. These hand-made calculations are based on the Direct Strength Method and the effective width method. The elastic buckling loads corresponding to local, distortional and global modes used in the DSM are obtained from CUFSM. The effective width methodology is carried out based on the provisions of EN 1993-1-3 concerning cold-formed sections and EN 1993-1-5 regarding plated structural elements.

## 3.2 Model Features

Our model consists of a light-gauge cold formed stud with a length of 2,316mm and a lipped C cross-section with two web stiffeners. The cross-section, code-named COCOON Transformer C-Profile 147/50/1.5, has 147mm web height, 50mm flange width, 10mm lip length and a uniform thickness of 1.5mm. The center part of the web has circular holes of 30mm diameter centered every 300mm. The next figure presents the cross-sectional dimensions; the material used to carry out the analyses is a plastic bilinear, simulative of steel S320GD+Z, and its properties are illustrated in the next table.
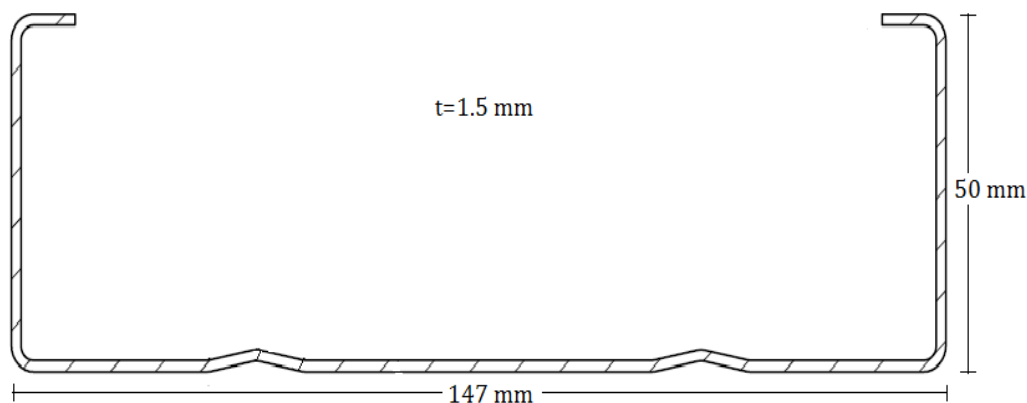


Figure 3-1: Cross-sectional dimensions

Table 3-1: Properties of steel S320GD+Z

| S320GD+Z | |
|---|---|
| Elasticity Modulus $E_e$ | 210 GPa |
| Poisson's ratio $v$ | 0.3 |
| Yield Stress $f_y$ | 320 MPa |
| Yield Strain $\varepsilon_y$ | 0.0015 |
| Strain Hardening Modulus $E_p$ | 415 MPa |
| Ultimate Stress $f_u$ | 390 MPa |
| Ultimate Strain $\varepsilon_u$ | 0.17 |

## 3.3 Numerical Analysis

### 3.3.1 Finite element modeling

The stud is modeled in ADINA using shell elements. The effect of rounded corners is neglected and thus the cross-section is considered to be constituted by 1.5mm thick plane elements. The end boundary conditions include a roller at the top and a pin at the bottom. In addition, minor axis bending is hindered by restraining the lateral movement at the flange's middle node every 60mm in height, to account for the constraints induced by the ballistic nails that connect the flanges with the plasterboards. The boundary conditions at the edges are modeled by utilizing rigid links in order to connect the top and bottom nodes of the cross-section with new nodes which are placed at the gravity center of the cross-section, in the way shown in Figure 3-3.
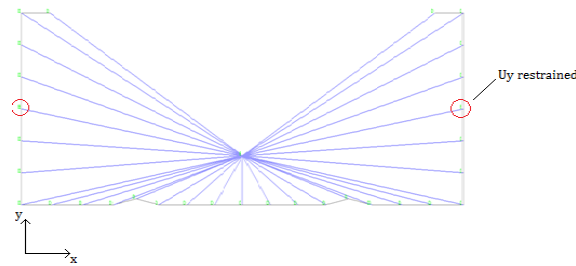
Figure 3-2: Computational cross-section and rigid links at ADINA

Creating the appropriate finite element mesh is the next step towards developing our model. Analyses are performed with various mesh densities in order to approach an efficient solution. Efficiency does not only represent mere precision but computational time, too. The goal is to create a mesh that provides accurate results and in the meantime reduces the computational cost and the necessary memory required for storing the output files at a reasonable level. The density is not uniformly applied to every part of the member. Generally, square elements with edge length around 10mm are used in the flanges and the subpanels of the web, whereas slightly smaller elements are used in the lips and the stiffeners and even denser mesh is used around the hollow parts of the web.

This "loose" mesh assembly represents the one used to carry out our analyses, while another mesh with increased density is exploited to verify the validity of the results at ad-hoc stages of the analysis. This "dense" mesh has twice the elements of the loose one. The dense mesh results are compared to the ones obtained from the loose mesh in two stages: a) to check the elastic critical buckling loads of each mode after acquiring the results of the linearized buckling analysis, b) to check the coincidence of the bearing capacity of the stud after imposing imperfections according to the most unfavorable mode combination. The density of the two for-mentioned meshes is depicted in the next figure for the bottom segment of the section.
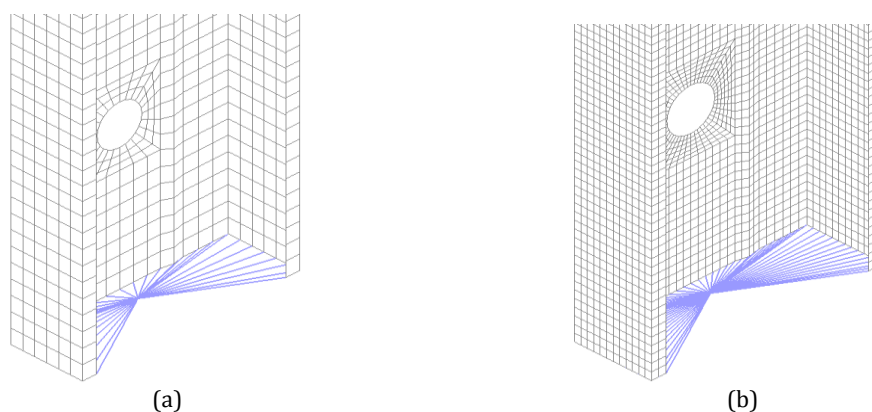


(a)                                                    (b)
Figure 3-3: Mesh density of (a) loose mesh (b) dense mesh

A vertical compressive load is imposed at the gravity center at the top edge of the stud in an attempt to alleviate the member from tensile stresses. This operation is performed by imposing either load-controlled or displacement-controlled compression. In any case, both loading types are examined in several cases to check the coincidence of the resultant equilibrium paths along with either arc-length or newton-raphson solution processes.

### 3.3.2    Linearized buckling analysis using finite elements

The Linearized buckling analysis (LBA) is performed in order to obtain the elastic critical buckling loads of each buckling mode. Our goal is to identify the modes with the critical load related to local, distortional and global buckling. The deformed cross-sectional shape was observed along with the half-wave lengths and the relationship of the eigenvectors corresponding to web versus flange buckling. The LBA is performed in ADINA using the finite element method and in CUFSM using the finite strip method to verify the results.



(a)                                                              (b)

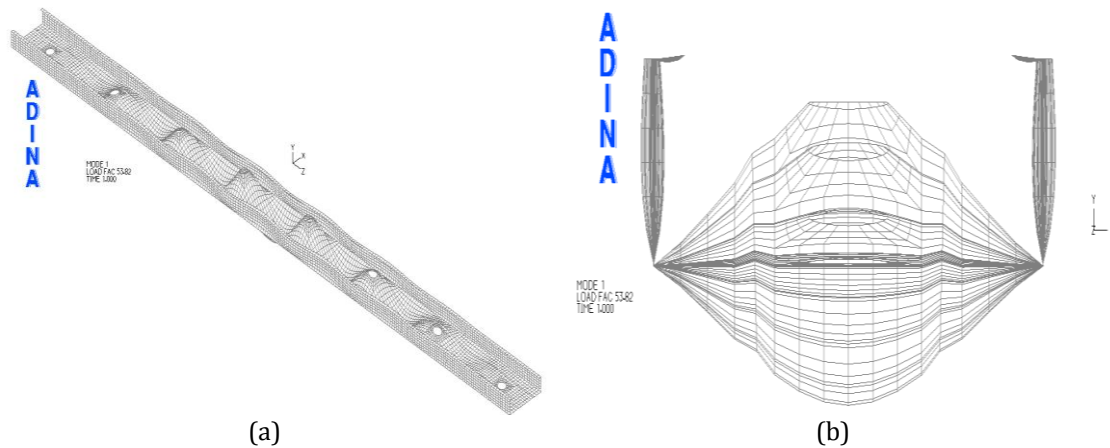Figure 3-4: 1st buckling mode - local buckling (a) general view (b) cross-sectional view



(a)                                                              (b)

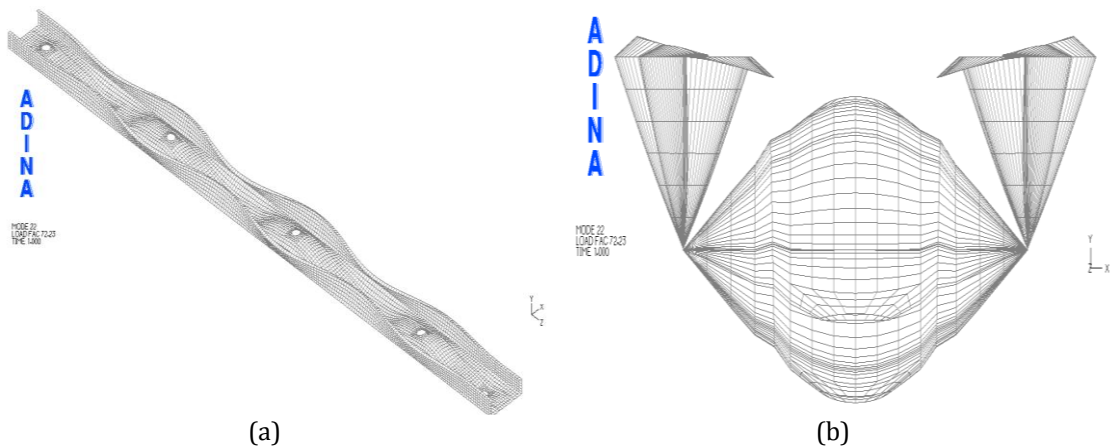Figure 3-5: 22nd buckling mode - distortional buckling (a) general view (b) cross-sectional view



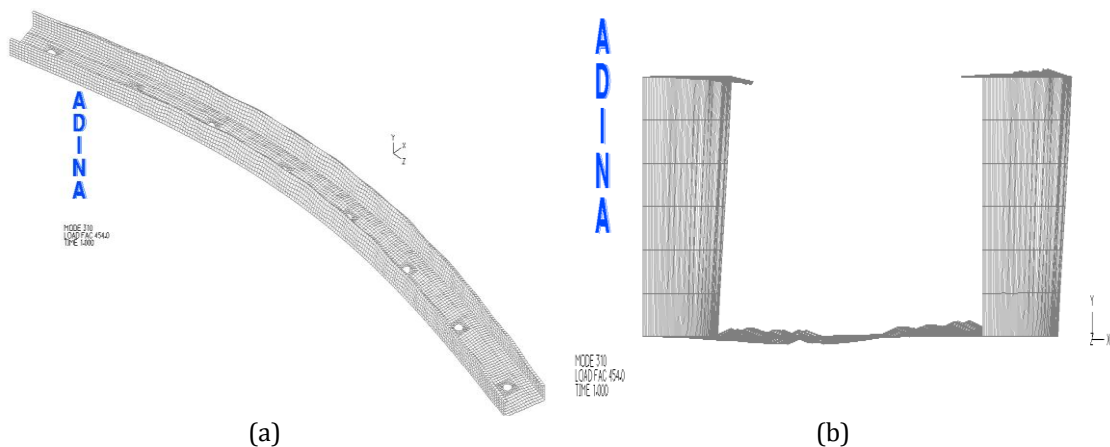(a)                                                              (b)

Figure 3-6: 310th buckling mode - global buckling (a) general view (b) cross-sectional view

Mode 1 exhibits the first local buckling and has a critical load $P_{cr}$=53.82kN. Its half-wavelength is estimated close to 140mm, slightly less than the height of the web. In addition, the maximum eigenvector corresponding to local web buckling is one order of magnitude greater than the maximum eigenvector corresponding to flange buckling. Mode 22 represents the first distortional buckling and has a critical load $P_{cr}$=72.23kN. Its half-wavelength is estimated close to 330mm and the maximum eigenvectors are similar in the *xy* plane. Mode 310 introduces the global buckling mode about the member's strong axis at a critical load $P_{cr}$=454.0kN and has a half-wavelength equal to the stud's total length.

### 3.3.3 Linearized buckling analysis using finite strips

The results stated in the previous paragraph are evaluated by performing a finite strip analysis at CUFSM. It should be noted, however, that finite strip analysis is valid only for continuous solid members. As a result, minor inconsistencies might be observed through directly comparing the finite strip results with those obtained from the finite element model. The three critical modes presented in the next figure match perfectly the results obtained from the LBA at ADINA to sufficiently complete our investigation regarding the elastic buckling loads. The respective loads of each mode are reported in Table 3-2 and Figure 3-8.



|      (a)      |      (b)      |      (c)      |
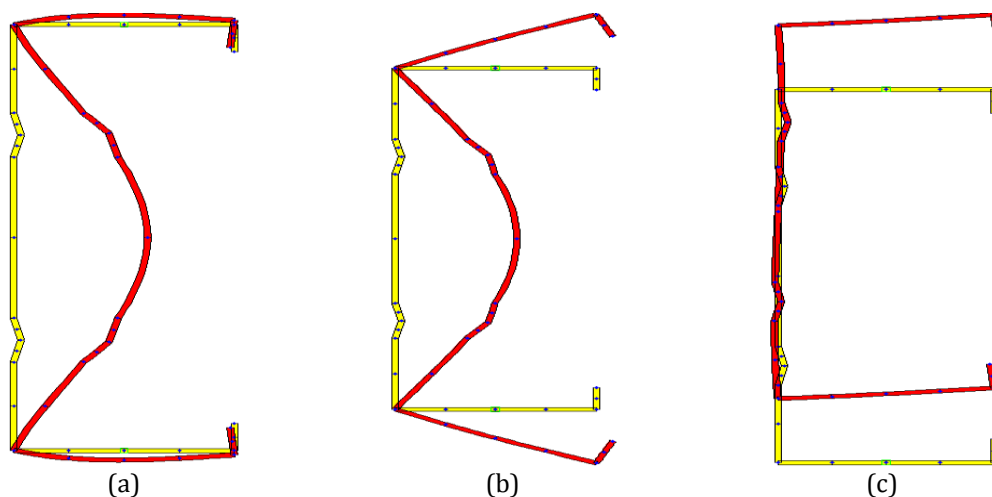
Figure 3-7: CUFSM results on critical modal buckled shape (a) local (b) distortional (c) global

CUFSM can also produce the signature curve, i.e. plotting the load factor against the half-wavelength. In the solution algorithm incorporated in CUFSM to solve the buckling eigenproblem, it is assumed that a specific half-wavelength has infinite modes that satisfy the inputs related to that half-wavelength. Nevertheless, the mode with the lesser critical load is likely to occur for that specific half-wavelength. Therefore, at each half-wavelength only the first mode of the eigenproblem is presented in order to plot the signature curve. The load factor which is presented in the *y* axis is the ratio of the elastic critical buckling load of the first mode of each half-wavelength to the yield load. The yield load is defined as the product of the gross cross-sectional area and the yield stress.

Figure 3-8: Signature curve

An illustrative presentation of the comparison between the results of ADINA and CUFSM related to the linearized buckling analysis is 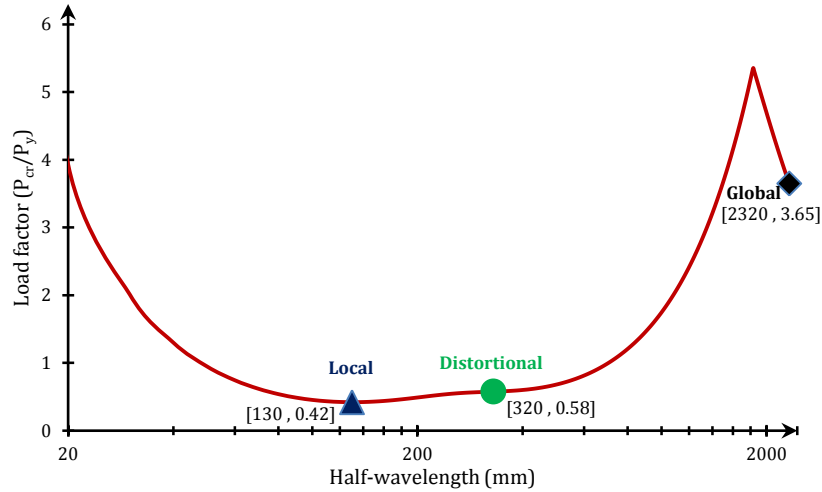shown in the next table. It shall be noted that the half-wavelengths taken from ADINA are graphically estimated whereas the half-wavelengths taken from CUFSM are numerically calculated. CUFSM validated the results obtained from ADINA as the variation between the outputs of the two programs is minimal. To determine the critical buckling loads of CUFSM, each load factor stated in Figure 3-8 is multiplied by the gross cross-sectional area $A$=391.04mm² and the yield stress $f_y$=0.320kN/mm².

Table 3-2: Linearized buckling analysis results of ADINA and CUFSM

|                   | ADINA | | CUFSM | |
|-------------------|------------------------|------------------|------------------------|------------------|
|                   | Half-wavelength (mm) | $P_{cr}$ (kN) | Half-wavelength (mm) | $P_{cr}$ (kN) |
| Local Mode        | 140   | 53.8 | 130   | 52.6 |
| Distortional Mode | 330   | 72.2 | 320   | 72.6 |
| Global Mode       | 2,316 | 454.0 | 2,320 | 456.7 |

Apart from the three buckling modes mentioned earlier, other modes will be considered in pre-fire conditions to explore their effect on the behavior of the stud. Although the critical modes corresponding to local, distortional and global buckling are expected to have higher contribution than the rest, one cannot completely ignore the possibility that the remaining modes contribute significantly in the overall behavior.

### 3.3.4    Initial geometric imperfections

Various researches have tried to explore the effect of geometric imperfections on the behavior of thin cold-formed members. Light-gauge cold-formed steel members are presumed to have significant geometric imperfections due to induced deformations during fabrication and handling. These imperfections are numerically imposed according to the shape of buckling modes as it has been observed [105] that cold-formed members are very sensitive to this type of input imperfections.

Geometric imperfections amplitude depends on the type of buckling mode, e.g. different values are used as input for local compared to global buckling modes. An independent inquiry has been executed to identify a realistic range of proper amplitudes for geometric imperfections as suggested by other researchers and Eurocode provisions. The amplitude value is usually expressed as a function of the plate width or the element thickness for local imperfections. For global modes, the amplitude represents the lateral mid-height deflection according to a deformed bow shape and is usually expressed as a fraction of the member's length.

In order to determine the proper range of imperfection amplitudes we took under consideration the formulas used/proposed by others and modified them according to the dimensions of the member under investigation. The next table summarizes the results we have found after looking into previous researches and regulations.

Table 3-3: Literature review findings on imperfection values

| Author | Local imperfection (mm) | Global imperfection (mm) |
|---|---|---|
| EN 1993-1-5 [106]& EN 1993-1-1 [107] | min($a/200$ ; $b/200$)=0.74 | L/200=11.6 |
| EN 1090-2: 2008 [33] | b/100=1.5 | L/750=3.1 |
| [43] | b/100=1.5 | L/1000÷L/400=2.3÷5.8 |
| [104] | t=1.5 | L/1000÷L/200=2.3÷11.6 |
| [105] | 0.006b=0.9 ; $6te^{-2t}$=0.5 | - |
| [56] | 1.0 | L/1000=2.3 |

*$a$ and $b$ are the panel's dimensions, $t$ is the nominal thickness of the panel and $L$ is the stud length

To meet this range of imperfection values listed in the previous table we considered values for local/distortional buckling imperfection from 0.5mm to 1.5mm and for global buckling from 1.0 to 20.0mm. Furthermore, various interaction attempts were made between different modes with different imperfection amplitudes to estimate the most unfavorable combination within reasonable limits. The results of these attempts are demonstrated in a later part of this thesis after performing geometric and material non-linear analyses with initial imperfections (GMNIA).

### 3.3.5 Geometric and material non-linear analyses with initial geometric imperfections

Determining the bearing capacity of the stud in terms of a vertically compressive action was the last step before proceeding with the fire situation. The outputs of different attempts using various imperfection amplitudes according to different buckling modes are presented in the next figures on the way of identifying the ultimate strength of the stud. Modes 1 and 22, corresponding to critical local and distortional buckling, seem to contribute utmost in the final behavior of the stud while mode 310 (flexural major axis buckling) is not observed in the shape of structural failure when a non-linear analysis without imperfections is carried out (GMNA).

Besides checking the structural behavior with imperfections according to individual modes, we examined the equilibrium paths for several combinations between different modes and imperfection amplitudes. The combination of initial geometric imperfection amplitudes of different modes was carried out according to §C.5 of EN 1993-1-5. This solution methodology

suggests that a leading imperfection has to be taken into account with its nominal amplitude and accompanying imperfections shall be combined with a reduced value to 70% of their nominal one. Any type of imperfection can be taken as the leading and the others as the accompanying in order to determine the most unfavorable combination.

Initially, in order to be consistent with the provisions of Eurocode 3 and EN 1090-2:2008, we performed combinations using modes 1, 22 and 310 with the nominal imperfections that are stated in Table 3-3. Those three modes were combined both pairwise and all together. The combination methodology was introduced in the previous paragraph according to §C.5 of EN 1993-1-5 with the leading imperfection varying at each analysis. Furthermore, a combination of every mode that has an elastic buckling load less than 100kN was performed by imposing 0.6 to 1.0mm imperfection amplitudes on every one of them, sequentially. Finally, an attempt to identify modal shapes similar to the collapse shape was made, and GMNI analyses incorporating these modes were executed.
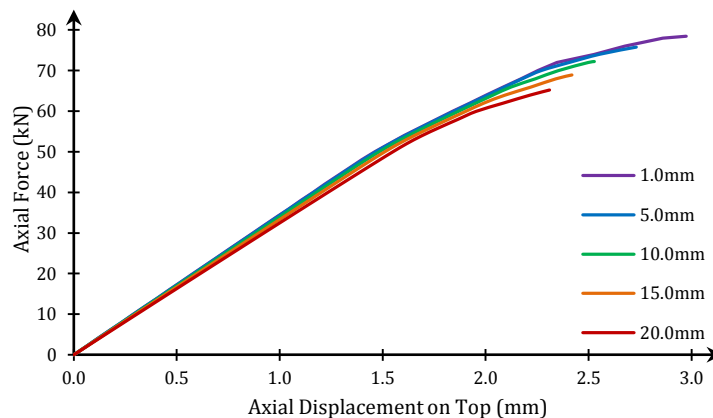


Figure 3-9: Equilibrium paths for various imperfections according to critical global Mode 310
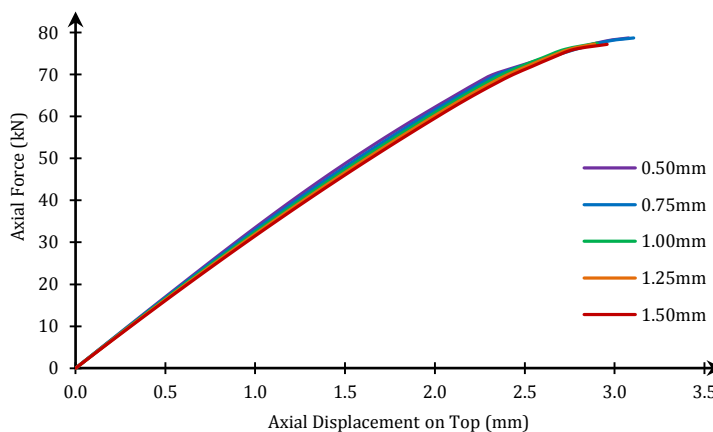


Figure 3-10: Equilibrium paths for various imperfections according to critical local Mode 1
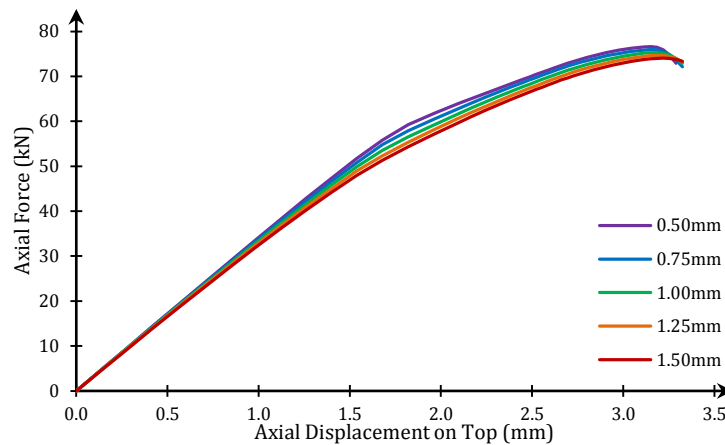
Figure 3-11: Equilibrium paths for various imperfections according to critical distortional Mode 22
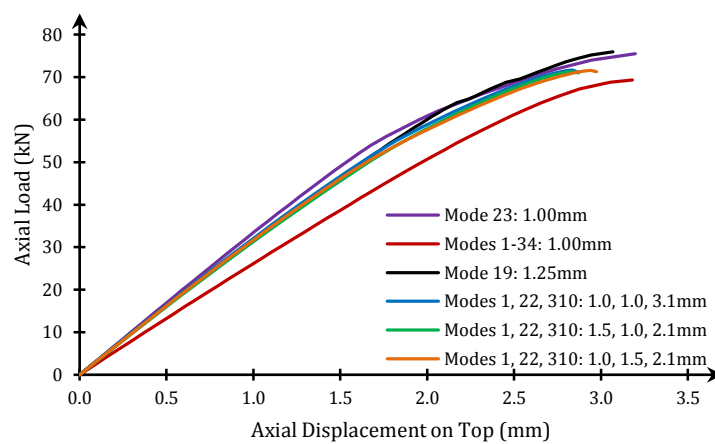


Figure 3-12: Equilibrium paths for various modes-imperfections
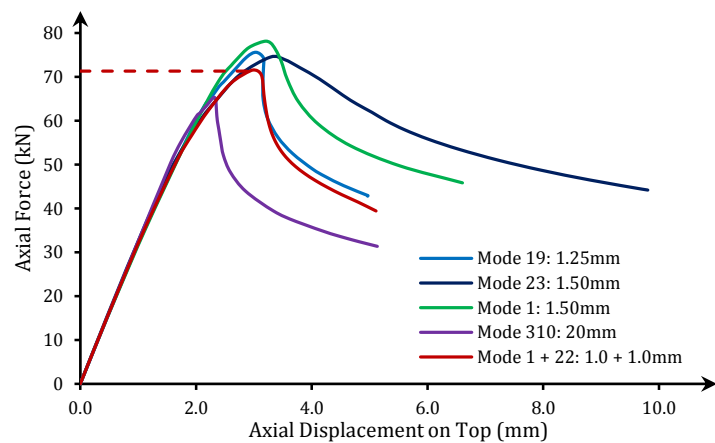


Figure 3-13: Equilibrium paths using Arc-Length method for various modes-imperfections

Figure 3-9 to Figure 3-12 present the results of the non-linear buckling analysis using the Newton-Raphson iteration method. This process allows the estimation of the primary path until the reach of the bifurcation point. In order to evaluate the consistency of this method we additionally performed non-linear analyses utilizing the Arc-Length method that allows the calculation of the secondary path. Figure 3-13 shows some of the results of the GMNIA depicting an unsteady secondary path. Such paths were obtained for every examined mode-imperfection

combination while the primary paths derived from Newton-Raphson and Arc-Length processes were totally identical.

The ultimate bearing capacity of the stud in terms of a vertical compressive load was found to receive values in the range of 78kN to 67kN, depending on the initial imperfection amplitudes. The most unfavorable combinations were those that included large global imperfections ($e_o$ > 5.0mm) and the ones comprising large values of both local and distortional imperfections ($e_o$ > 1.0mm). The most severe combination was conducted according to EN 1993-1-5 & EN 1993-1-1 lead by global imperfection and accompanied by local and distortional imperfections. The maximum load was estimated at $P_{max}$=67.6kN. However, the global imperfection has a very high value, thus probably producing over conservative results. A more reasonable/accurate solution might be according to EN 1090-2:2008 lead by distortional and accompanied by local and global buckling for a maximum load of $P_{max}$=71.3kN.
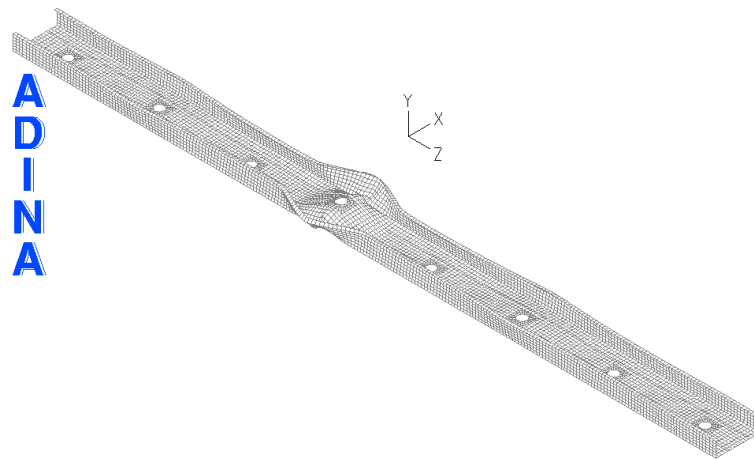


Figure 3-14: Failure mode corresponding to 1.0mm imperfection of the 1st buckling mode and 1.0mm imperfection of the 22nd buckling mode (Arc - Length last step)

The mode combination adopted as initial input during the fire situation comprises 1.0mm imperfection of the 1st mode and 1.0mm imperfection of the 22nd mode yielding an axial strength of 71.7kN (Figure 3-13 red curve). In any case, the effect of initial imperfections on the structural response during fire conditions is expected to be negligible because the behavior is governed by thermal bowing; a fact also verified by our parametric analyses with different initial imperfection shapes and amplitudes.

## 3.4  Direct Strength Method

The *Direct Strength Method* estimates a member's buckling resistance in terms of a vertical compressive force, after taking into consideration the critical buckling load of each type of buckling, i.e. local, distortional and global.

First, the yield load $P_y$ is calculated by:

$$P_y = Af_y = 391 \times 0.320 = 125 kN$$

where:

*A* is the gross cross-sectional area

$f_y$ is the yield stress

## Global buckling

The nominal axial strength, $P_{ne}$, corresponding to global buckling is based on the slenderness factor $\lambda_C$ which is determined by equation 1.2.1-3 of Appendix 1 of AISI, 2004:

$$\lambda_C = \sqrt{\frac{P_y}{P_{cre}}} = \sqrt{\frac{125}{454}} = 0.525 < 1.5$$

where:

$P_{cre}$ is the elastic critical buckling load of the global buckling mode, obtained from the results of CUFSM

For $\lambda_C < 1.5$, the nominal axial strength is given by eq. 1.2.1-1:

$$P_{ne} = \left(0.658^{\lambda_C^2}\right) P_y = \left(0.658^{0.525^2}\right) \times 125 = 111.5 kN$$

## Local buckling

The slenderness factor $\lambda_\ell$ is calculated first using equation:

$$\lambda_\ell = \sqrt{\frac{P_{ne}}{P_{cr\ell}}} = \sqrt{\frac{111}{54}} = 1.434 > 0.776$$

where:

$P_{cr\ell}$ is the elastic critical buckling load of the local buckling mode, obtained from the results of CUFSM

The nominal axial resistance $P_{n\ell}$ is obtained by:

$$P_{n\ell} = \left[1 - 0.15 \left(\frac{P_{cr\ell}}{P_{ne}}\right)^{0.4}\right] \left(\frac{P_{cr\ell}}{P_{ne}}\right)^{0.4} P_{ne} = 74.0 kN$$

## Distortional buckling

The slenderness factor $\lambda_d$ is determined by:

$$\lambda_d = \sqrt{\frac{P_y}{P_{crd}}} = \sqrt{\frac{125}{72.23}} = 1.316 > 0.561$$

where:

$P_{\text{crd}}$ is the elastic critical buckling load of the distortional buckling mode, obtained from the results of CUFSM

The nominal axial resistance $P_{\text{nd}}$ is obtained from:

$$P_{\text{nd}} = \left[1 - 0.25\left(\frac{P_{\text{crd}}}{P_{\text{y}}}\right)^{0.6}\right]\left(\frac{P_{\text{crd}}}{P_{\text{y}}}\right)^{0.6} P_{\text{y}} = 73.8 kN$$

Hence, the minimum nominal axial resistance corresponds to the distortional mode and the axial strength $P_{\text{u}}$ of the member after applying the resistance factor $\varphi$=0.85 equals to:

$$P_{\text{u}} = \varphi \min(P_{\text{ne}}; P_{\text{n}\ell}; P_{\text{nd}}) = \varphi P_{\text{nd}} = 62.7 kN$$

## 3.5  Effective Width Method

The calculations are executed based on the provisions of EN 1993-1-3 and EN 1993-1-5. Our scope is to determine the axial compressive strength and compare this value with the one obtained from the DSM and the finite element model.

### 3.5.1  Influence of rounded corners

According to §5.1 of EN 1993-1-3, the influence of rounded corners in the properties of the cross-section may be neglected, and the cross-section is assumed to be constituted by plane elements with sharp corners, if the two following conditions are met:

  i.    r ≤ 5t
  ii.   r ≤ 0.10b$_p$

where:

$r$ is the internal radius of the corners, equal to 2 or 2.5 mm

$b_p$ is the net width of each flange, equal to 48 mm

$t$ is the plate thickness, equal to 1.5 mm

Hence, for the unfavorable $r/t$ and $r/b_p$ combinations the results are:

$$\frac{r}{t} = \frac{2.5}{1.5} = 1.67 < 5 \quad ✓$$

$$\frac{r}{b_{\text{p}}} = \frac{2.5}{48} = 0.05 < 0.10 \quad ✓$$

Therefore we neglect the influence of rounded corners and the cross section under investigation is depicted in the next figure.
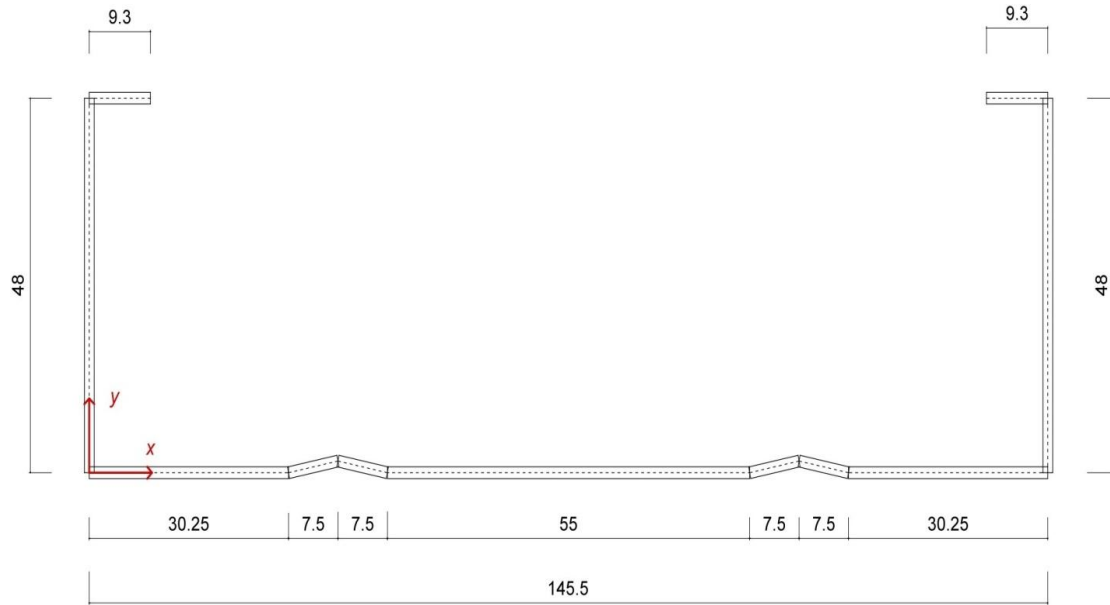
Figure 3-15: Computational cross-section

## 3.5.2 Effective web area

We consider the web to be supported at its intersection with the flanges and therefore it is doubly supported under uniform compression stress. Tables 4.1 and 4.2 of EN 1993-1-5 present the values of the buckling factor $k_\sigma$ after taking into consideration the stress ratio $\psi$ and the boundary conditions. Table 4.1 corresponding to internal compression elements is presented in the next figure.

Table 3-4: Internal compression elements [106]

| Stress distribution (compression positive) | | | Effective width $b_{eff}$ | | | |
|---|---|---|---|---|---|---|
|  | | | $\underline{\psi = 1}$: <br> $b_{eff} = \rho\ \bar{b}$ <br><br> $b_{e1} = 0{,}5\ b_{eff}$ $\qquad$ $b_{e2} = 0{,}5\ b_{eff}$ | | | |
|  | | | $\underline{1 > \psi \geq 0}$: <br> $b_{eff} = \rho\ \bar{b}$ <br><br> $b_{e1} = \dfrac{2}{5-\psi} b_{eff}$ $\qquad$ $b_{e2} = b_{eff} - b_{e1}$ | | | |
|  | | | $\underline{\psi < 0}$: <br> $b_{eff} = \rho\ b_c = \rho\ \bar{b} / (1-\psi)$ <br> $b_{e1} = 0{,}4\ b_{eff}$ $\qquad$ $b_{e2} = 0{,}6\ b_{eff}$ | | | |
| $\psi = \sigma_2/\sigma_1$ | 1 | $1 > \psi > 0$ | 0 | $0 > \psi > -1$ | -1 | $-1 > \psi > -3$ |
| Buckling factor $k_\sigma$ | 4.0 | $8.2/(1.05+\psi)$ | 7.81 | $7.81 - 6.29\psi + 9.78\psi^2$ | 23.9 | $5{,}98 \times (1-\psi)^2$ |

In our case, $\sigma_1 = \sigma_2 \rightarrow \psi = 1 \rightarrow k_\sigma = 4$

The coefficient $\varepsilon$ depending on the yield stress $f_y$ is determined by:

$$\varepsilon = \sqrt{\frac{235}{f_{yb}}} = \sqrt{\frac{235}{320}} = 0.857$$

For the determination of the reduction factor $\rho$ we divide the web into three subpanels where the intermediate longitudinal stiffeners define the boundaries of each subpanel according to the next figure.
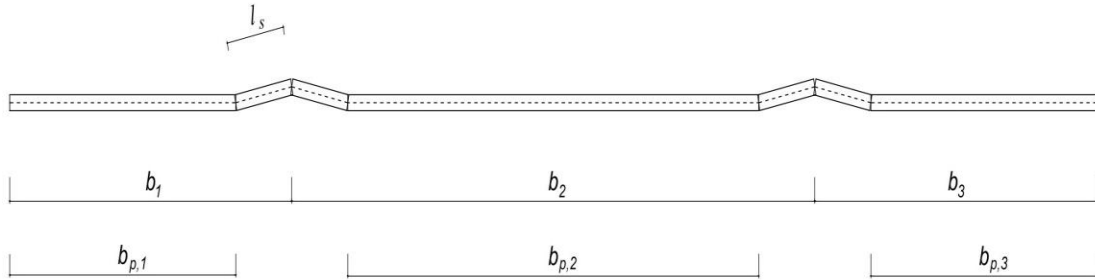


Figure 3-16: Notations on subpanel widths

$b_1 = b_3 = 37.75$ mm $\rightarrow b_{p,1} = b_{p,3} = 30.25$ mm

$b_2 = 70.00$ mm $\rightarrow b_{p,2} = 55.00$ mm

$l_s = 7.65$ mm

To determine the starting effective widths we use the maximum cross-sectional resistance during a compressive induced load $\sigma_{com,Ed}$. During the beginning of the calculations, this value is considered to be equal to the yield stress $f_{yb}$, and it is refined as the iteration procedure unfolds (usually it diminishes as the compressive resistance of a light-gauge cold formed steel cross-section depends mostly on the local buckling resistance of the member rather than its material's yield strength).

The plate slenderness $\bar{\lambda}_p$ of the $i$ subpanel ($i$=1, 2, 3) is calculated according to §4.4 of EN 1993-1-5 using the equation:

$$\bar{\lambda}_{p,i} = \frac{\bar{b}_{p,i}/t}{28.4\varepsilon\sqrt{k_\sigma}}$$

where:

$\bar{b}_{p,i}$ is the net width of the $i$ subpanel

$t$ is the element thickness

Hence,

$$\bar{\lambda}_{p,1} = \bar{\lambda}_{p,3} = 0.414 < 0.673 \;\; \rightarrow \rho_{1,3} = 1$$

$$\bar{\lambda}_{p,2} = 0.753 > 0.673 \quad \rightarrow \rho_2 = \frac{\bar{\lambda}_{p,2} - 0.055(3 + \psi)}{\bar{\lambda}_{p,2}^2} = 0.940$$

The effective widths of each subpanel are illustrated in the following figure.
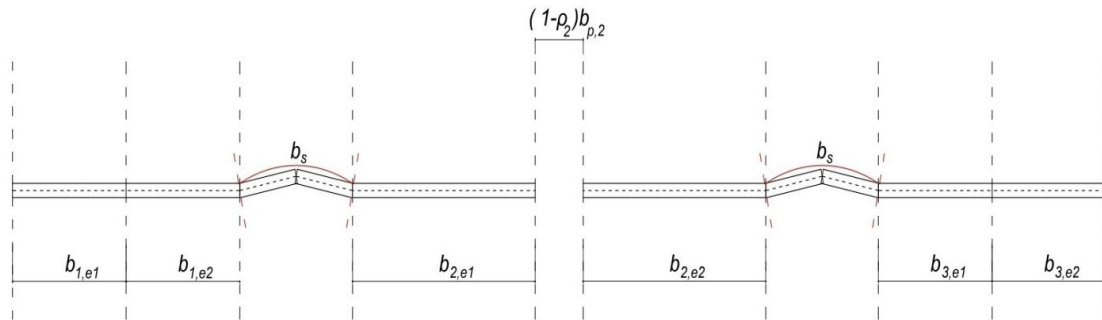


Figure 3-17: Subpanel effective width

To calculate the critical buckling load of a web with two longitudinal stiffeners we consider two possible buckling situations according to §A.2 of EN 1993-1-5. First, we assume that only one stiffener buckles while the other one acts as a rigid support. Second, we assume that both stiffeners buckle by substituting them with a new single lumped stiffener. The new stiffener should have:

i.    Same cross sectional area $A_{sl}$ and second moment of area $I_{sl}$ as the sum of the two individual stiffeners

ii.    Proper position, i.e. at the resultant of the respective forces of the individual stiffeners



| | Stiffener I | Stiffener II | Lumped stiffener |
|---|---|---|---|
| Cross-sectional area | $A_{s\ell,1}$ | $A_{s\ell,2}$ | $A_{s\ell,1} + A_{s\ell,2}$ |
| Second moment of area | $I_{s\ell,1}$ | $I_{s\ell,2}$ | $I_{s\ell,1} + I_{s\ell,2}$ |

Figure 3-18: Notations for plate with two stiffeners in the compression zone [106]

### 3.5.2.1    Buckling of a single stiffener

In our cross section, the stiffeners are symmetrically placed and have similar geometric properties. As a result the buckling of each individual stiffener has the same effects on the behavior of the web.

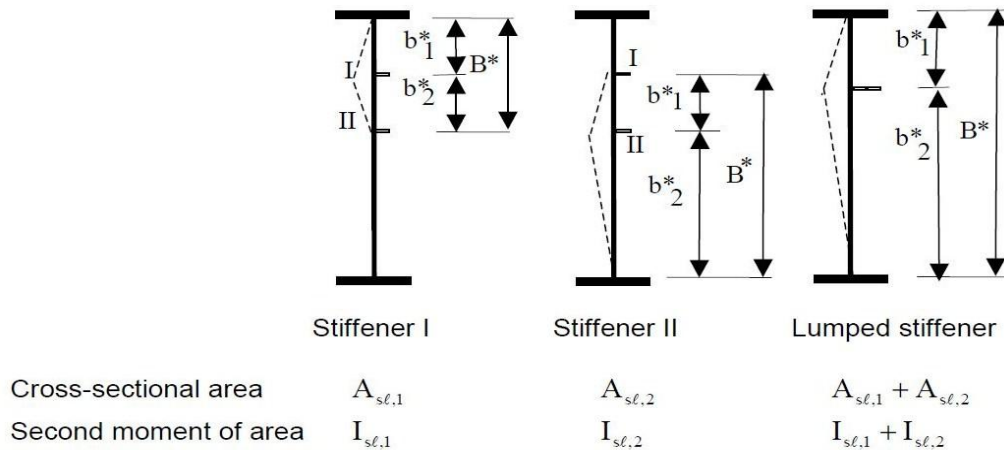The gross cross sectional area of the stiffener and the adjacent parts of the plate $A_{s,I}$ is calculated by:

$$A_{s,I} = 2A_{s,eff} + t \times (b_{1,e2} + b_{2,e1}) = 1.5 \times 2 \times 7.65 + 1.5 \times (15.125 + 24.31) \rightarrow$$

$$A_{s,I} = 82.103 \ mm^2$$

where:

$A_{s,eff}$ is the effective area of the stiffener

The $y$ coordinate of the gravity center of the stiffened area is determined by:

$$y_{CM} = \frac{2A_{s,eff} \times y_{s,eff} + A_{w,eff} \times y_{w,eff}}{A_{s,I}} = \frac{2 \times 1.5 \times 7.65 \times 0.75 + 59.153 \times 0}{82.103} \rightarrow$$

$$y_{CM} = 0.210 \ mm$$

The second moments of area $I_x$ and $I_y$ for the part of the stiffener about the two perpendicular axes passing through its center of gravity are calculated by:

$$I_x = \frac{l_s t^3}{12} = \frac{7.65 \times 1.5^3}{12} = 2.15 \ mm^4$$

$$I_y = \frac{t l_s^3}{12} = \frac{1.5 \times 7.65^3}{12} = 55.96 \ mm^4$$

By rotating the two axes by $\theta = \tan^{-1}(\frac{1.5}{7.5}) = 11.3$ degrees counter-clockwise we get the area moment of inertia about the axis which is parallel to the out-of-plane buckling axis of the stiffened area $a$-$a'$ passing through the previously calculated $y_{CM}$.
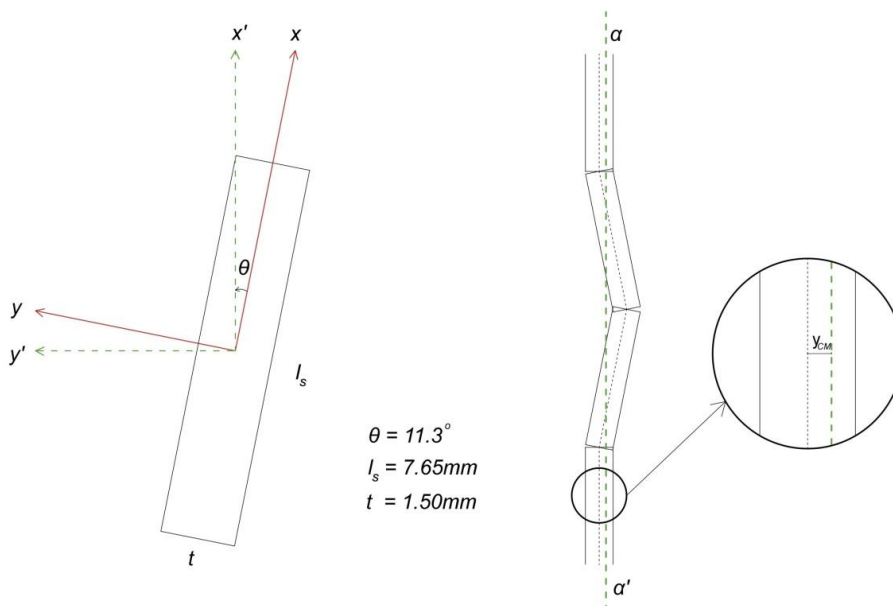


Figure 3-19: Notations on calculating stiffener's second moment of area

$$I_{s,x'} = \frac{I_x + I_y}{2} + \frac{I_x - I_y}{2}\cos(2\theta) = 29.055 - 24.825 = 4.23 \ mm^4$$

Finally, the out-of-plane second moment of area $I_{s,I}$ of the stiffened area about the *a-a'* axis after utilizing both plane members of the stiffener and the adjacent subpanels effective width is:

$$I_{s,I} = \left[I_{s,x'} + A_{s,eff}\left(y_{s,eff} - y_{CM}\right)^2\right] \times 2 + \frac{(b_{1,e2} + b_{2,e1})t^3}{12} + A_{w,eff}y_{CM}^2 \ \rightarrow$$

$$I_{s,I} = [4.23 + 11.475 \times (0.75 - 0.210)^2] \times 2 + \frac{39.435 \times 1.5^3}{12} + 59.153 * 0.210^2$$

$$I_{s,I} = 7.58 \times 2 + 11.091 + 2.61 = 28.86 \ mm^4$$

According to figure A.3 of EN1993-1-5 the appropriate values for $b_1$ and $b_2$ are:

$$b_1 = b_1^* = 37.75 \ mm \quad \& \quad b_2 = b_2^* = 70.00 \ mm$$

The corresponding spring stiffness $K$ is calculated using equation 5.11 of EN 1993-1-3, after conservatively neglecting the rotational spring stiffness.

$$K = \frac{3(b_1 + b_2)Et^3}{b_1^2 \ b_2^2 \ 12(1 - v^2)} = \frac{3 \times 107.75 \times 210{,}000 \times 1.5^3}{37.75^2 \times 70.00^2 \times 12 \times (1 - 0.3^2)} = 3.005 \ ^N/_{mm^2}$$

The critical buckling stress $\sigma_{cr,s}$ of an intermediate stiffener derives from equation 5.19 of EN 1993-1-3:

$$\sigma_{cr,s} = \frac{2\sqrt{KEI_{s,I}}}{A_{sl}} = \frac{2 \times \sqrt{3.005 \times 210{,}000 \times 28.86}}{82.103} = 103.96 \ ^N/_{mm^2}$$

We will compare this critical buckling stress to the one we will obtain from the buckling of both stiffeners and we will proceed with the solution process using the lesser of them.

### 3.5.2.2    Buckling of both stiffeners

The gross cross sectional area of the stiffener and the adjacent parts of the plate $A_{sl,II}$ is calculated using:

$$A_{s,II} = 2A_{s,I} = 164.206 \ mm^2$$

The *y* coordinate of the gravity center of the stiffened area is determined by:

$$y_{CM} = \frac{A_{s,eff} \times y_{s,eff} + A_{w,eff} \times y_{w,eff}}{A_{s,I}} = 0.210 \ mm$$

The new second moment of area $I_{s,II}$ is twice the previously calculated $I_{s,I}$:

$$I_{s,II} = 2 \times I_{s,I} = 57.72 \ mm^4$$

Assuming the new lumped stiffener is positioned at web mid-height, we derive the values $b_1 = b_2$ = 72.75 mm

The corresponding spring stiffness after neglecting the rotational spring stiffness is obtained from:

$$K = \frac{3(b_1 + b_2)Et^3}{b_1^2\, b_2^2\, 12(1 - v^2)} = \frac{3 \times 145.5 \times 210,000 \times 1.5^3}{72.75^2 \times 72.75^2 \times 12 \times (1 - 0.3^2)} = 1.011\ ^N/_{mm^2}$$

To evaluate this result, a linear elastic analysis was performed at ADINA with a distributed line load of 1 $N/mm$ in the middle of the web. The respective maximum displacement was 0.9986mm; hence, K= 1/0.9986=1.001 $N/mm^2$.

Hence, the critical buckling stress $\sigma_{cr,s}$ is:

$$\sigma_{cr,s} = \frac{2\sqrt{KEI_{s,II}}}{A_s} = \frac{2 \times \sqrt{1.011 \times 210,000 \times 57.72}}{164.206} = 42.64\ ^N/_{mm^2}$$

Observing that the critical buckling stress value corresponding to buckling of both stiffeners is less than the one obtained for the buckling of one stiffener, we now use this value to derive the relative slenderness of the web from equation:

$$\bar{\lambda}_d = \sqrt{\frac{f_{yb}}{\sigma_{cr,s}}} = \sqrt{\frac{320}{42.64}} = 2.74\ > 1.38\ \rightarrow \chi_d = \frac{0.66}{2.74} = 0.24$$

We will now start the first iteration to refine the value of $\chi_d$.

The new relative slenderness for each subpanel of the web $\bar{\lambda}_{p,red}$ is obtained from the relative slenderness of the previous step using the formula:

$$\bar{\lambda}_{p,red} = \bar{\lambda}_p\sqrt{\chi_d}$$

Therefore, for each subpanel the respective plate slenderness becomes:

$$\bar{\lambda}_{p,1} = \bar{\lambda}_{p,3} = 0.414 \times \sqrt{0.24} = 0.203 < 0.673\ \rightarrow \rho = 1$$

$$\bar{\lambda}_{p,2} = 0.832 \times \sqrt{0.24} = 0.408 < 0.673\ \rightarrow \rho = 1$$

Hence, the whole web length is effective.

The new effective cross sectional area, excluding the effective lengths near the flange supports is:

$$A_s = \left(b_{1,e2} + b_{p,2} + b_{3,e1} + \sum_{i=1}^{4} l_{s,i}\right)t = (85.25 + 30.6) \times 1.5 = 173.8\ mm^2$$

The new gravity center of the stiffened web area is:

$$y_{\text{CM}} = \frac{85.25 \times 0 + 30.6 \times 0.75}{85.25 + 30.6} = 0.198 \; mm$$

The second moment of area $I_s$ is obtained from:

$$I_{\text{s}} = 4\left[I_{\text{s,x'}} + A_{\text{s,eff}}\left(y_{\text{s,eff}} - y_{\text{CM}}\right)^2\right] + \frac{\left(b_{1,\text{e2}} + b_{\text{p,2}} + b_{3,\text{e1}}\right)t^3}{12} + A_{\text{w,eff}}y_{\text{CM}}^2 \;\rightarrow$$

$$I_{\text{s}} = 4 \times \left[4.23 + 11.475 \times (0.75 - 0.198)^2\right] + \frac{85.25 \times 1.5^3}{12} + 127.875 \times 0.198^2$$

$$I_{\text{s}} = 30.91 + 23.98 + 5.01 = 59.9 \; mm^2$$

The spring stiffness is unchanged and has a value of $K = 1.011$ N/mm$^2$

The elastic critical buckling stress now changes to:

$$\sigma_{\text{cr,s}} = \frac{2\sqrt{KEI_{\text{s}}}}{A_s} = \frac{2 \times \sqrt{1.011 \times 210{,}000 \times 59.9}}{173.8} = 41.04 \; {N}/{mm^2}$$

The new relative slenderness is:

$$\bar{\lambda}_{\text{d}} = \sqrt{\frac{f_{\text{yb}}}{\sigma_{\text{cr,s}}}} = \sqrt{\frac{320}{41.04}} = 2.79 \; > 1.38 \;\; \rightarrow \chi_{\text{d}} = \frac{0.66}{2.79} = 0.23 \; \approx 0.24$$

The new value of the reduction factor $\chi_{\text{d}}$ is almost similar to the value of the previous step and therefore the iteration procedure stops. The effective area of the web is:

$$A_{\text{w,eff}} = \chi_{\text{d}}A_{\text{s}} + 2A_{\text{edge,eff}} = 0.23 \times 173.8 + 30.25 \times 1.5 = 85.35 \; mm^2$$

The stiffened area $A_s$ is assumed to have uniformly less thickness according to equation:

$$t_{\text{red}} = \chi_{\text{d}}t = 0.23 \times 1.5 = 0.345 mm$$

### 3.5.3    Effective flange area

In order to provide sufficient buckling stiffness to the flanges, the size of the stiffeners (lips) should be within the following ranges:
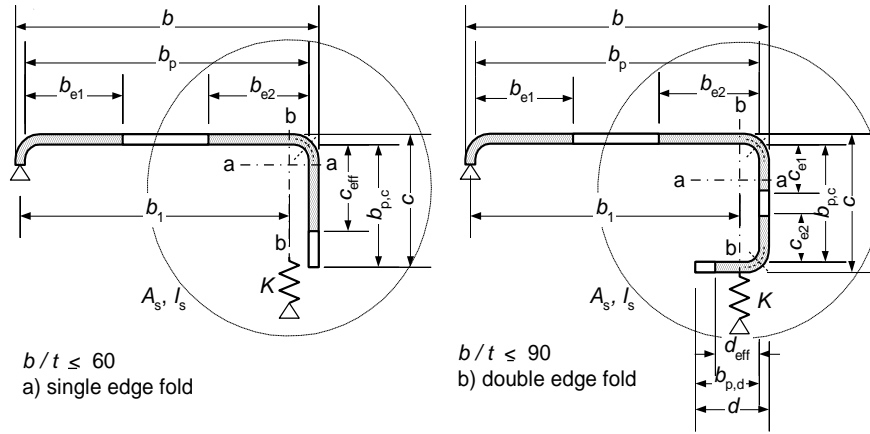
$$0.2 \leq c/b \leq 0.6$$

Figure 3-20: Notations on edge stiffeners [108]

In the cross section under investigation $c$ = 10.0 mm and $b$ = 49.5 mm. Therefore, c/b = 0.202 > 0.20 and we consider the flange as a doubly supported compression element.

Furthermore, the angle between the flange and the lip should be within the range of 45° and 135°. In our case, this criterion is also satisfied as the angle is 90°.

As the cross section is uniformly compressed, from table 4.1 of EN 1993-1-5 we get $\psi = 1 \to k_\sigma = 4$

The plate slenderness $\bar{\lambda}_p$ of the flange is determined by:

$$\bar{\lambda}_p = \frac{\bar{b}_p/t}{28.4\varepsilon\sqrt{k_\sigma}} = \frac{48/1.5}{28.4 \times 0.857 \times 2} = 0.657 < 0.673 \to \rho = 1$$

The whole flange is considered to be effective $\to b_{e1} = b_{e2} = 0.5b_p = 24$ mm

For a single edge fold stiffener we obtain the value $b_{p,c}/b_p$ from:

$$\frac{b_{p,c}}{b_p} = \frac{9.3}{48} = 0.194 < 0.35 \to k_\sigma = 0.5$$

The plate slenderness $\bar{\lambda}_p$ for the stiffener (lip) is determined by:

$$\bar{\lambda}_p = \frac{\bar{b}_p/t}{28.4\varepsilon\sqrt{k_\sigma}} = \frac{9.3/1.5}{28.4 \times 0.857 \times 0.707} = 0.360 < 0.673 \to \rho = 1 \to c_{eff} = c$$

The effective area of the stiffener is calculated by:

$$A_s = t(b_{e2} + c_{eff}) = 49.95 \ mm^2$$

The *x* coordinate of the gravity center of the stiffener is obtained from:

$$x_{CM} = \frac{24 \times 0 + 9.3 \times \frac{9.3}{2}}{24 + 9.3} = 1.30 \ mm$$

The second moment of area $I_s$ corresponding to the out-of-plane buckling axis of the flange is given by the equation:

$$I_s = \frac{b_{e2}t^3}{12} + A_{e2} \times 1.30^2 + \frac{tc_{eff}^3}{12} + A_{lip}(x_{CM,lip} - x_{CM})^2 \rightarrow$$

$$I_s = \frac{24 \times 1.5^3}{12} + 36 \times 1.30^2 + \frac{1.5 \times 9.3^3}{12} + 13.95 \times (4.65 - 1.30)^2 \rightarrow$$

$$I_s = 6.75 + 60.84 + 100.55 + 156.55 = 324.69 \ mm^4$$

The spring stiffness is determined by equation 5.10b of EN 1993-1-3:

$$K = \frac{Et^3}{4(1 - v^2)} \times \frac{1}{b_1^2 h_w + b_1^3 + 0.5 b_1 b_2 h_w k_f}$$

where:

$b_1$ is the distance between the junction of the web with the flange and the gravity center of the stiffener $\rightarrow b_1 = y_{CM} = \frac{24 \times 36 + 9.3 \times 48}{24 + 9.3} = 39.35 \ mm$

$b_2 = b_1 = 39.35$ mm

$h_w$ is the web height = 145.5 mm

$k_f = 1.0$ for symmetrical cross section under uniform compression load

Hence,

$$K = \frac{210,000 \times 1.5^3}{4 \times (1 - 0.3^2)} \times \frac{1}{39.35^2 \times 145.5 + 39.35^3 + 0.5 \times 39.35 \times 39.35 \times 145.5 \times 1.0}$$

$$\rightarrow K = 0.488 \ {}^N\!/_{mm^2}$$

The elastic critical buckling stress is derived from equation:

$$\sigma_{cr,s} = \frac{2\sqrt{KEI_s}}{A_s} = \frac{2 \times \sqrt{0.488 \times 210,000 \times 324.69}}{49.45} = 233.3 \ {}^N\!/_{mm^2}$$

Comparing the elastic critical buckling stress of the flanges with the respective stress of the web, we must note that the flanges seem to have almost one order of magnitude higher buckling stress; a fact consistent with the eigenvectors obtained during the linearized buckling analysis which was performed at ADINA.

The relative slenderness is determined by:

$$\bar{\lambda}_{\mathrm{d}} = \sqrt{\frac{f_{\mathrm{yb}}}{\sigma_{\mathrm{cr,s}}}} = \sqrt{\frac{320}{233.3}} = 1.17 \ > 0.65 \ \rightarrow \chi_{\mathrm{d}} = 1.47 - 0.723\bar{\lambda}_{\mathrm{d}} = 0.62$$

We will now start the iteration procedure to refine the value of the effective area of the flange and the stiffener.

The new relative slenderness $\bar{\lambda}_{\mathrm{p,red}}$ is determined by:

$$\bar{\lambda}_{\mathrm{p,red}} = \bar{\lambda}_{\mathrm{p}}\sqrt{\chi_{\mathrm{d}}} = 0.32\sqrt{0.62} = 0.252 \ < 0.673 \ \rightarrow \rho = 1$$

Hence, the whole area of the flange and the lip is considered to be effective and the previous calculations would yield the same result for the reduction factor χ if they were to be performed.

The effective thickness of the stiffener which is constituted by half of the flange and the lip is considered to be:

$$t_{\mathrm{red}} = \chi_{\mathrm{d}}t = 0.62 \times 1.5 = 0.93 \ mm$$

The effective area of the flanges and the lips is:

$$A_{\mathrm{f,l,eff}} = 2t\big[\chi_{\mathrm{d}}\big(b_{\mathrm{e2}} + b_{\mathrm{p,c}}\big) + b_{\mathrm{e1}}\big] = 2 \times 1.5 \times [0.62 \times (24 + 9.3) + 24] \rightarrow$$

$$A_{\mathrm{f,l,eff}} = 133.94 \ mm^2$$

### 3.5.4    Buckling resistance of the cross-section

The overall effective area of the cross section $A_{\mathrm{eff}}$ is:

$$A_{\mathrm{eff}} = A_{\mathrm{f,l,eff}} + A_{\mathrm{w,eff}} = 133.94 + 85.35 = 219.29 \ mm^2$$

The maximum cross-sectional uniform compressive resistance is:

$$N_{\mathrm{Rd}} = A_{\mathrm{eff}}f_{\mathrm{yb}} = 70.17 \ kN$$

### 3.5.5    Buckling resistance of the stud

Apart from considering the local buckling effects we must also consider the global buckling effects and further reduce the above stated buckling load. The gross and the effective cross section are depicted in the next figures.
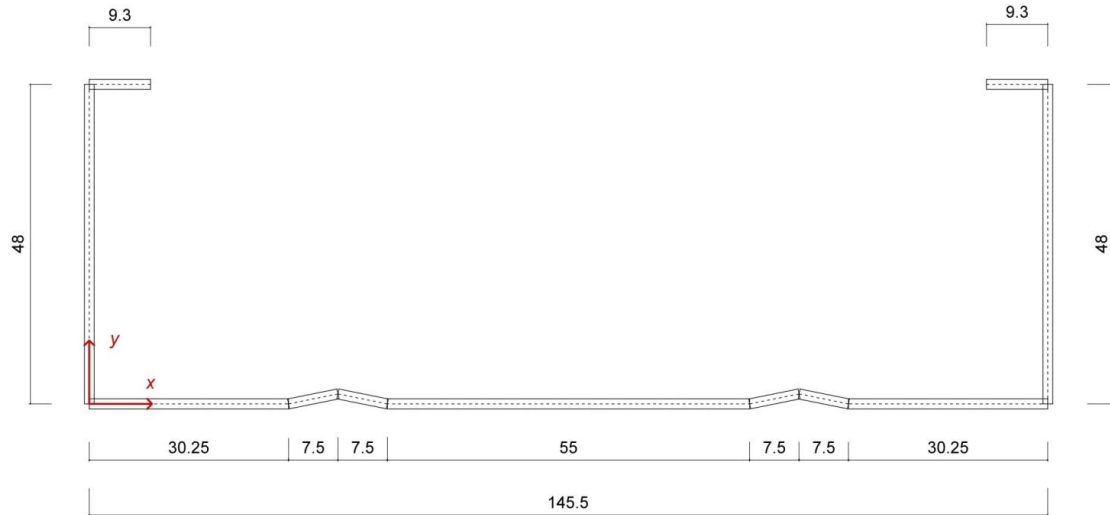
Figure 3-21: Gross cross-section
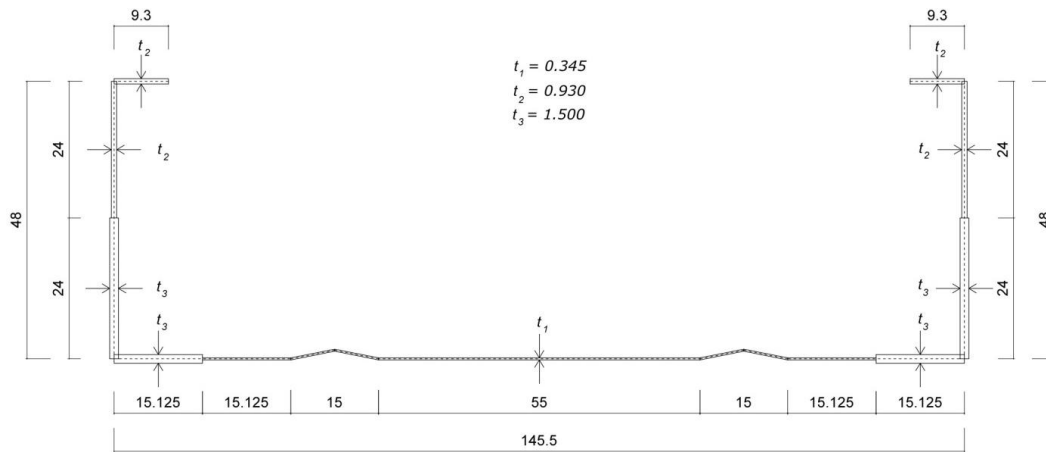

Figure 3-22: Effective cross-section

The gross cross sectional area is: $A$ = 391.05 mm²

The effective cross sectional area is: $A_{eff}$ = 219.29 mm²

The coordinates of the gravity center of the gross cross section are:

$y_{CM}$ = 12.350 mm and $x_{CM}$ = 72.750 mm

The second moment of area of the gross cross section about its strong axis is: $I_{y-y'}$ = 1,276,780 mm⁴

The elastic critical buckling load based on the properties of the gross cross section is determined by:

$$N_{cr} = \frac{\pi^2 E I_{y-y'}}{l_{cr}^2} = \frac{\pi^2 \times 210,000 \times 1,276,780}{2,316^2} = 493 \, kN$$

The non dimensional slendernese based on the properties of the effective cross section derives from:

$$\bar{\lambda} = \sqrt{\frac{A_{\text{eff}}f_{\text{yb}}}{N_{\text{cr}}}} = \sqrt{\frac{219.29 \times 320}{493,000}} = 0.377$$

From table 6.3 of EN 1993-1-3, the buckling curve *b* is obtained to represent the buckling behavior of our member based on its respective imperfections.

The imperfection factor $\alpha$ receives a value of: $\alpha$ = 0.34

The coefficient Φ is given by:

$$\Phi = \frac{1}{2}\left[1 + \alpha(\bar{\lambda} - 0.2) + \bar{\lambda}^2\right] = 0.601$$

Finally, the reduction factor $\chi$ is obtained from the equation:

$$\chi = \frac{1}{\Phi + \sqrt{\Phi^2 - \bar{\lambda}^2}} = 0.935$$

Therefore, the critical buckling load of the stud after taking into account both the effects of local and global buckling is:

$$N_{\text{b,rd}} = \chi A_{\text{eff}}f_{\text{yb}} = 0.935 \times 219.29 \times 320 = 65.6\ kN$$

## 3.6  Conclusions

This chapter has presented the methodology towards estimating the bearing capacity of a cold-formed thin-walled member. Finite element and finite strip models were considered in order to determine the elastic buckling modes and their corresponding loads using ADINA and CUFSM, respectively. Geometric and material non-linear analyses with initial geometric imperfections were executed for various imperfections' combinations to estimate the bearing capacity of the stud, in terms of concentric vertical compressive loading. Furthermore, analytical estimations of the axial strength were carried out according to the Direct Strength Method and Eurocode 3.

The finite element and finite strip models demonstrated sufficient coincidence regarding the elastic buckling loads and modes, even though CUFSM does not account for the hollow web parts and each program utilizes different theory to produce the results. This fact clarifies the efficiency of using small repeated perforations in the webs of channel sections as a means for electrical conduits etc. since their contribution to the hindering of overall strength is minimal. However, the analytical calculation of the elastic global buckling load overestimated the final result leading to a value of 493kN for the critical global buckling mode, instead of 454kN which was numerically estimated. Moreover, it is evident that bearing capacity reduction is dominated mainly by local buckling, accounting for 44% reduction based on the ratio of the effective area to the gross cross-sectional area, instead of global buckling which contributes nearly up to 7%.

Irrespective of the imperfection amplitude and the mode according to which this amplitude is introduced in the model, a linear path seems to govern responses up to the vicinity of the elastic buckling load of the 1st mode. Moreover, the axial strength based on the critical local buckling mode seems uncorrelated with respect to different imperfection amplitudes. On the other hand, distortional buckling proves to be more susceptible to imperfection values and global buckling displays even more significant strength reduction with increased imperfections. Imperfection combinations based on the critical modes corresponding to local, distortional and global buckling seem to produce the most unfavorable results on the structural response, since no other mode explicitly presents an eigenshape similar to the failure deformation pattern.

The analytical calculations provide a decent way of estimating the axial compressive strength of the member under investigation. The DSM provided a solution with 12.5% divergence from the numerical model, whereas the EN 1993-1-3 effective width method diverged 8.5%. Even though the effective width method proved to be more accurate, its solution process still remains cumbersome. On the other hand, obtaining the elastic buckling loads from a finite strip analysis and utilize them as input to feed the DSM yields an instant estimation of the axial strength with sufficient prediction precision.

# 4 Evaluation of Structural Adequacy at Elevated Temperatures

## 4.1 Introduction

Fire safety design ensures the ability of a member to withstand specific fire safety requirements. These requirements may be reflected in the domains of time, temperature or strength. Most often the fire safety factor expresses the duration required for a total loss of strength, which shall exceed a critical duration specified at relevant regulations. The failure criteria for a composite wall are expressed in terms of insulation, integrity and structural adequacy; identifying the latter is the object of this chapter.

Fire exposure tampers with the thermal, mechanical and deformation properties of a steel member. The fire behavior is mostly governed by increased deformations and reduced strength and stiffness. These factors vary with time as the temperature increases, while they also vary across the member since non-uniform temperature is applied. Additional insulation layers may affect the thermal performance of the drywall though not only in a positive way. In this study, the time-temperature profile of the cross-section is determined using ANSYS CFX, after applying the standard ISO 834 time-temperature curve [109], whereas the structural integrity is investigated at ADINA.

Both steady state and transient state conditions are considered in order to determine the load ratio to temperature relationship. In steady state modeling, temperature gradually increases to reach a target value and then an incremental load is applied until failure. Transient state modeling represents the actual conditions where the load is input first and then the temperature profile is applied until failure. Both methods are supposed to produce similar results for specific load ratios to temperature profiles, but steady state analysis can additionally provide equilibrium paths in order to explicitly illustrate the structural response.

The results obtained from the finite element model are compared to analytical calculations; not only to verify the prediction accuracy of the numerical analysis, but additionally to examine the compatibility of the specification provisions with our estimations. The EN 1993-1-2 method is examined using the effective area results presented in the previous chapter according to EN 1993-1-3 for cold-formed members. Furthermore, a modified EN 1993-1-3 method is presented incorporating reduced material properties and compared to the EN 1993-1-2. Moreover, a modified DSM method is utilized after performing finite strip analysis at CUFSM using the reduced material properties at elevated temperatures, to obtain another interesting angle.

Finally, an investigation of the thermal performance under a uniform temperature profile is demonstrated. EN 1993-1-2 conservatively suggests that if non-uniform temperature is applied, then the maximum cross-sectional temperature shall be used in the analytical calculations. For this reason, we examine the response under uniform temperature by comparing it with the non-uniform FEM case and both the DSM and Eurocode 3-based analytical methodologies.

## 4.2   Light Gauge Steel Frame Model

### 4.2.1    Formations

The light gauge steel frame (LSF) under investigation is considered sheathed in four different plasterboard-insulation formations. Single or double layered, type A, 12.5mm thick plasterboards are employed to clad the load bearing members C 147/50/1.5 from both sides. The air cavities created by the structural elements and the plasterboards can be either empty or filled with mineral wool as insulation material. In order to attach the plasterboards to the structural elements ballistic nails are used; however, their existence is neglected in the heat transfer model since their contribution is expected to be infinitesimal. The four alternative drywall configurations are depicted in the following figure with a width of 625mm corresponding to the mean distance between the steel studs.
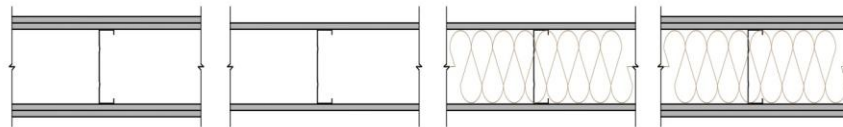
Figure 4-1: LSF wall configurations

### 4.2.2    Heat transfer model

The four possible formations are input in ANSYS CFX in order to determine the temperature profiles across the member. Temperature-related values for the thermal conductivity $\lambda$ and specific heat $C$ are employed to increase the prediction accuracy of the model; an inquiry through the various relationships proposed by other researches was performed and the literature sources used to derive these values are shown in Table 4-1. Material density is considered constant for all materials during temperature escalation. The corresponding values for the thermal properties are depicted in Figure 4-2.

Table 4-1: Literature sources for the acquisition of thermal properties

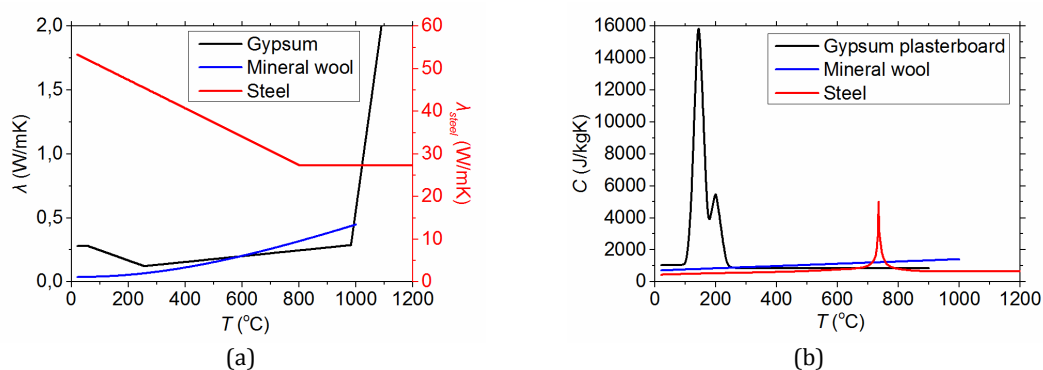| Material | $\rho$ (kg/m³) | $\lambda$ (W/mK) | $C$ (J/kgK) |
|---|---|---|---|
| Gypsum Plasterboard | 742 | [110] | [110] |
| Steel | 7850 | [111] | [111] |
| Mineral Wool | 18 | [46] | [46] |
| Air cavity | 1.2 | [112] | [112] |

Figure 4-2: Thermal properties' variation with temperature, (a) Thermal conductivity and (b) Specific heat

ISO 834 provides a proper time-temperature curve to be imposed on the fire side. This temperature increasing rate is input in ANSYS along with each sheathing formation of the drywall and an ambient temperature of $20^{\circ}$C at the unexposed side in order to obtain the temperature distribution along the cross-section as a function of the elapsed time for each case. In the finite element model created at ADINA, each lip is considered to have constant temperature while linear distribution is assumed on each flange and web. The temperature is exported by ANSYS in five points of the cross-section (Figure 4-3a), namely:

 i.   Exposed flange tip, i.e. flange-lip juncture on fire side
 ii.  Exposed flange web, i.e. flange-web juncture on fire side
 iii. Middle web, i.e. web mid-height
 iv.  Unexposed flange web, i.e. flange-web juncture on ambient side
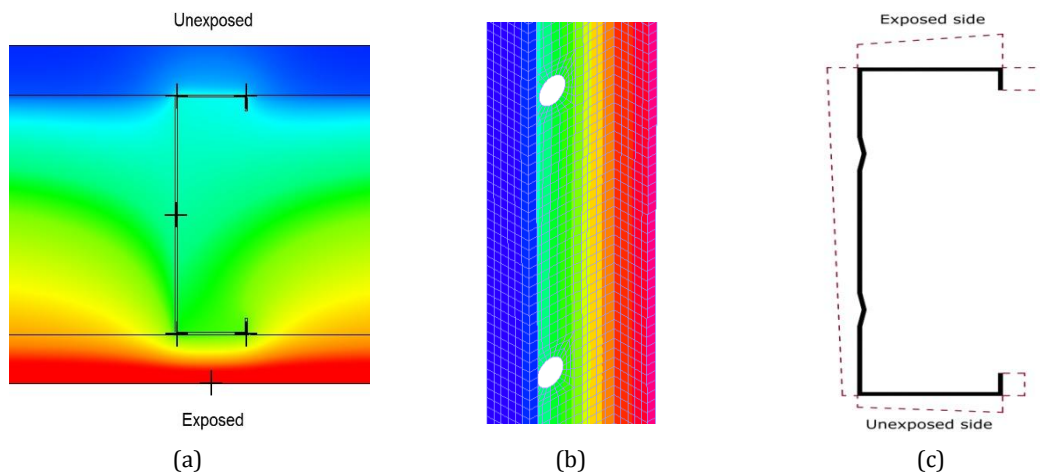 v.   Unexposed flange tip, i.e. flange-lip juncture on ambient side



Figure 4-3: (a) Temperature variation exported by ANSYS (b) temperature distribution input at ADINA deriving from (c) cross-sectional idealized temperature profile

### 4.2.3    Structural model

A thermo-plastic material is chosen to represent the actual material's behavior during fire conditions at ADINA. The initial material S320GD+Z is modified to simulate the real behavior of steel at elevated temperatures by having reduced characteristic mechanical properties. The reduction laws applied to the yield stress, elasticity modulus, thermal expansion and strain hardening modulus derive from EN 1993-1-2, for Class 4 members, while the ultimate strain remains constant at 17%. Specifically for the strain hardening modulus, the same reduction law with the elasticity modulus is applied; thermal creep is not included in the model. The mesh density is the same one used at ambient temperature conditions. Stress-strain curves at various temperatures in degrees Celsius are depicted in the next figure for the material of our model.
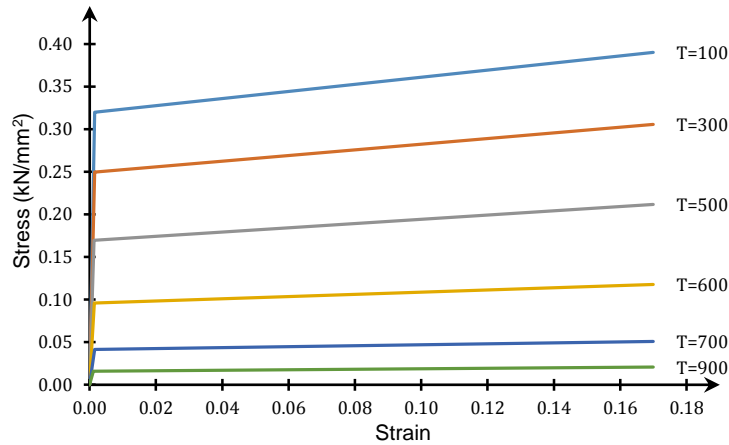
Figure 4-4: Constitutive stress-strain laws at various temperatures

To evaluate the consistency of the results obtained from ADINA, both steady state and transient state analysis are performed. In steady state conditions, a temperature profile is applied across the member to reach a specific value and then an incremental compressive load is imposed until failure. In transient state analysis, a load is input with constant value and then temperature gradually increases until failure. In either case, our goal is to export the values of maximum load, temperature distribution and elapsed time at failure. An advantage of steady state analysis is the fact that we can additionally output equilibrium paths.

## 4.3   Analytical Calculation Process

Checking the results of the finite element model along with the estimations resulting from different regulations' methodologies is attempted in this section. Since the preciseness of steel behavior at elevated temperatures remains clouded by uncertainties and lack of systematic research, regulations usually provide conservative methods to counterbalance clarity deficiency. We hope that by defining the magnitude of this error we can enhance future research with useful information regarding the amendment of the current practices involved in estimating the fire resistance of thin-walled steel members.

### 4.3.1   EN 1993-1-2 method

EN 1993-1-2 suggests that when non-uniform temperature is applied at the cross-section, the highest temperature should be used in the calculations. Furthermore, while ambient temperature calculations incorporate relative slenderness values higher than 0.2, the reduction factor $\chi_{fi}$ in fire conditions is determined by a different formula. This method is based on the effective cross-sectional area calculated using EN 1993-1-3 provisions at ambient conditions (for class 4 members), which was presented in the previous chapter in order to consider local buckling effects. In addition, flexural buckling impacts are incorporated with the use of the reduction factor $\chi_{fi}$, standing for global buckling effects at elevated temperatures. Finally, yield stress and elastic modulus deterioration is taken into account by applying the reduction factors $k_{y,\theta}$ and $k_{E,\theta}$ to the initial yield stress and elastic modulus values as the temperature increases.

*4.3.1.1 Performing the official EN solution process according to EN 1993-1-2*

After imposing an initial load of 56kN≈0.8$P_{max}$ in the numerical model, the final step of the analysis provided us with a maximum temperature of $T_{max}$=388.3℃ at the exposed flange and a $T_{min}$=131.6℃ at the ambient side of the stud. We will use this temperature values to estimate the bearing capacity of the stud in terms of a vertical compressive load using the EN 1993-1-2 process.

The class of the cross section is derived from Table 5.2 of EN 1993-1-1 for sections with outstanding flanges:

$$\frac{c}{t} = \frac{49.5 - 1.5}{1.5} = 32 > 14\varepsilon = 14 \times 0.85 \times \sqrt{\frac{235}{f_{yb}}} = 10.2 \quad \rightarrow class\ 4$$

where:

$c$ is the net flange width

$t$ is the flange thickness

$\varepsilon$ is calculated using an additional reduction factor of 0.85 as described in equation 4.2 of EN 1993-1-2 due to fire conditions.

The result classifies our cross-section in *class 4* where local buckling is expected to occur long before the member reaches its yield strength in one or more parts of the cross-section.

The ultimate compressive load of a steel member under fire conditions is determined by:

$$N_{b,fi,t,Rd} = \frac{\chi_{fi}\ A_{eff}\ k_{y,\theta}\ f_y}{\gamma_{M,fi}}$$

where:

$A_{eff}$ is the effective area of the cross-section

$\chi_{fi}$ is the reduction factor for flexural buckling in the fire design situation

$k_{y,\theta}$ is the reduction factor for the yield strength of steel at the maximum cross sectional temperature (388.3 ℃ in our case) given at table E.1 for cold formed class 4 sections

$\gamma_{M,fi}$ is the partial factor for material properties during fire conditions and has a value of 1.00

The value of $\chi_{fi}$ describes the unfavorable buckling axis, which is the strong axis in our case. The standard value of $\chi_{fi}$ is calculated using the provisions of clause 6.3.1.3 of EN 1993-1-1 and clause 4.2.3.2 of EN 1993-1-2.

The effective cross-sectional area, estimated in the previous chapter, is:

$$A_{\text{eff}} = 219.29\ mm^2$$

The non-dimensional slenderness $\bar{\lambda}$ for class 4 sections has already been calculated and has a value of:

$$\bar{\lambda} = 0.377$$

The reduction factor for the yield strength $k_{y,\theta}$ at a temperature of 388.3 °C derives from table E.1 of EN 1993-1-2 and the reduction factor of the Young's Modulus $k_{E,\theta}$ derives from table 3.1. Their values are:

$$k_{y,\theta} = 0.66521\ \ ;\ \ k_{E,\theta} = 0.7117$$

The non-dimensional slenderness $\bar{\lambda}_\theta$ for the temperature $T_{\text{max}}$=388.3 °C is given by:

$$\bar{\lambda}_\theta = \bar{\lambda}\left(\frac{k_{y,\theta}}{k_{E,\theta}}\right)^{0.5} = 0.967\bar{\lambda} = 0.365$$

Next, the factors $a$ and $\varphi_\theta$ are determined in order to formulate equation 4.6 of EN 1993-1-2 and specify the reduction factor $\chi_{fi}$.

$$a = 0.65 \times \left(\frac{235}{f_y}\right)^{0.5} = 0.557$$

$$\varphi_\theta = \frac{1}{2}\left[1 + \alpha\bar{\lambda}_\theta + \bar{\lambda}_\theta^2\right] = \frac{1}{2} \times [1 + 0.203 + 0.133] = 0.668$$

Therefore:

$$\chi_{y,fi} = \frac{1}{\varphi_\theta + \sqrt{\varphi_\theta^2 - \bar{\lambda}_\theta^2}} = 0.815$$

Finally, the maximum bearing capacity of the stud expressed in terms of an axial compressive load at a maximum temperature of 388.3 °C is given by:

$$N_{\text{b,fi,t,Rd}} = \frac{\chi_{y,fi}\ A_{\text{eff}}\ k_{y,\theta}\ f_y}{\gamma_{\text{M,fi}}} = \frac{0.815 \times 219.29 \times 0.66521 \times 320}{1.00} = 38.17\ KN$$

Alternatively, we will estimate the bearing capacity of the cold flange at the temperature of 131.6 °C using the same procedure as the one described in the case of the hot flange.

The reduction factors for the yield strength and the Young's modulus are:

$$k_{y,\theta} = 0.965\ \ ;\ \ k_{E,\theta} = 0.968$$

The non-dimensional slenderness $\bar{\lambda}_\theta$ for the temperature $T_{\text{min}}$=131.6 °C is given by:

$$\bar{\lambda}_\theta = \bar{\lambda} \left(\frac{k_{y,\theta}}{k_{E,\theta}}\right)^{0.5} = 0.998\bar{\lambda} = 0.376$$

The factor $\varphi_\theta$ is obtained from:

$$\varphi_\theta = \frac{1}{2}\left[1 + \alpha\bar{\lambda}_\theta + \bar{\lambda}_\theta^2\right] = 0.675$$

Therefore:

$$\chi_{y,fi} = \frac{1}{\varphi_\theta + \sqrt{\varphi_\theta^2 - \bar{\lambda}_\theta^2}} = 0.809$$

Finally, the maximum bearing capacity of the stud expressed in terms of vertical compressive load at a temperature of 131.6 $^\circ$C is given by:

$$N_{b,fi,t,Rd} = \frac{\chi_{y,fi}\, A_{eff}\, k_{y,\theta}\, f_y}{\gamma_{M,fi}} = \frac{0.809 \times 219.29 \times 0.965 \times 320}{1.00} = 54.78\, KN$$

### 4.3.2    EN 1993-1-3 modified method

EN 1993-based method for officially estimating the bearing capacity of any steel member was presented in §4.3.1. However, by modifying the methodology of EN 1993-1-3 for local buckling and EN 1993-1-1 for global buckling, a new set of results can be obtained. Using reduced values for Young's Modulus and yield stress according to EN 1993-1-2 as input in order to feed the effective width method, refined values of the cross-sectional bearing capacity are extrapolated for each temperature. Note that the maximum temperature of the cross-section was considered to reduce the mechanical properties uniformly across the stud. By determining the reduction factor $\chi$ corresponding to flexural buckling according to EN 1993-1-1, but with the diminished material properties as input, we finally exported the new feature set, which proved to be compatible with the rest of the methods. In this method, the provisions of EN 1993-1-2 are used only to define the material properties at each temperature. To that end, reduction laws for mechanical properties proposed by other scientists can be easily utilized to provide another solution set.

### 4.3.3    Direct Strength Method

The Direct Strength Method has proved to be a very useful tool for quick estimation of the bearing capacity of cold-formed sections. Importing the elastic critical buckling loads for each buckling type and calculating the yield load is all it takes for this method to compute the axial strength. Using CUFSM as the provider of the elastic buckling loads, with gradually reduced elasticity modulus, after computing the corresponding strength with reduced yield loads, we can determine another modified relationship between the load factor and the respective temperature. The reduced elastic modulus values were considered uniform across the section corresponding to the maximum temperature of the member.

## 4.4  Results

### 4.4.1  Numerical model output

As it was mentioned earlier, fire resistance estimation usually aims at providing proper curves that express bearing capacity deterioration as a function of time. However, negligible information on structural response emanates from graphs of such type. Time conceals collateral non-structural aspects that affect the structural behavior such as insulation specifications and plasterboard material/thickness, drywall assembly, imposed time-temperature curve etc. Nevertheless, time provides a useful domain to observe the effects of thermal creep. However, thermal creep is not taken into account in our model; hence, load ratios are mainly plotted against temperature. Load ratios express the imposed load as a fraction of the axial strength ($P_{max}$=71.7kN) while temperature usually refers to the exposed flange tip on the fire side of the cross-section.

#### 4.4.1.1  Single walled

The single walled formation refers to cladding the stud with one layer of plasterboard at each side. This assembly has been examined using cavity insulation or no insulation. After applying the ISO 834 time dependent temperature curve a cross-sectional temperature increase is observed. The increase of cross-sectional temperature with respect to elapsed time is depicted in the next figures for both configuration types. These temperature profiles are used to feed the finite element model in order to evaluate the structural adequacy of the stud at elevated temperatures.
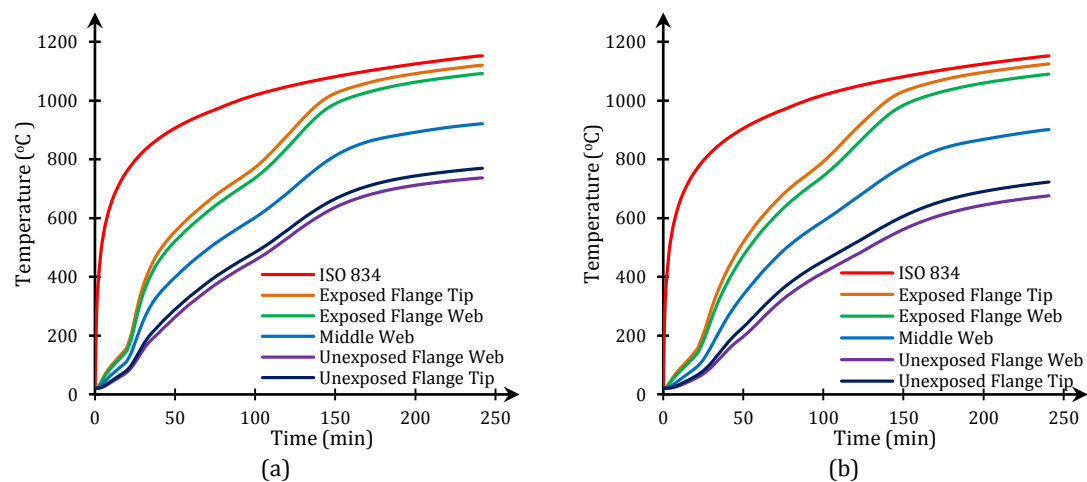


Figure 4-5: Temperature escalation for (a) uninsulated and (b) insulated formation

Steady state and transient state analyses were performed for both cases providing identical results. These outputs express the axial load-bearing capacity of the stud as a function of time or temperature. The ultimate load obtained at each temperature profile is normalized using the ultimate load at ambient conditions. Hence, axial strength attenuation is presented in the next figures as a function of different extents.
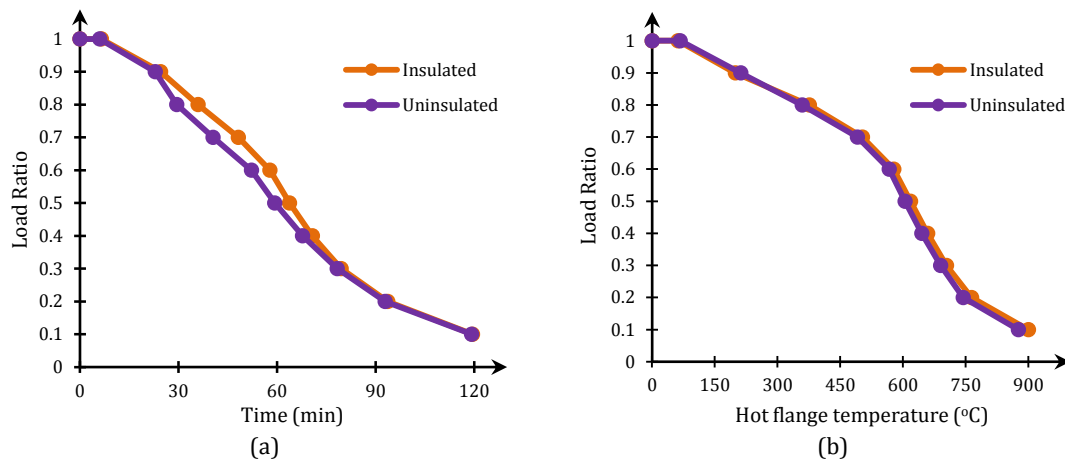
Figure 4-6: Load ratio decrease in terms of (a) time and (b) hot flange temperature

### 4.4.1.2    Double Walled

The double wall configuration refers to cladding the stud with two plasterboard layers at each side. Similar to the single walled formation, cavity insulation or no insulation was considered. The temperature profiles across the stud for each ad hoc specified feature point as a function of time is presented in the next figures for the two cases.
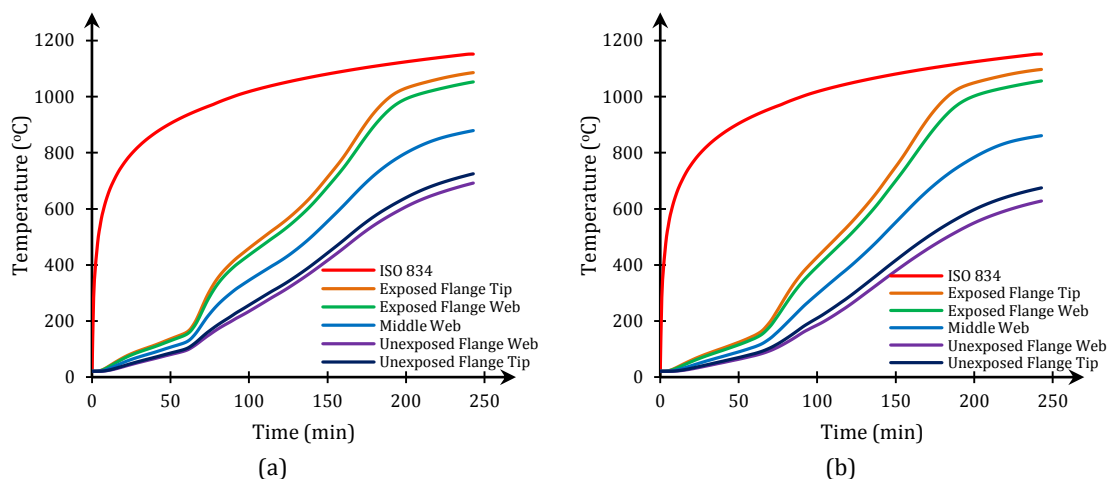


Figure 4-7: Temperature escalation for (a) uninsulated and (b) insulated formation

As in the case of the single walled configuration, steady state and transient state analyses are performed to evaluate the thermal performance of the stud. By utilizing the temperature profiles presented in the previous figures we are able to acquire the load ratio to temperature or time curve in the way depicted in the next two figures. Note that the notation "hot flange temperature" in the figures refers to the maximum cross-sectional temperature, i.e. the temperature of the exposed flange tip.

Figure 4-8: Load ratio reduction with respect to (a) time and (b) maximum cross-sectional temperature

### 4.4.2    Validation of numerical solutions

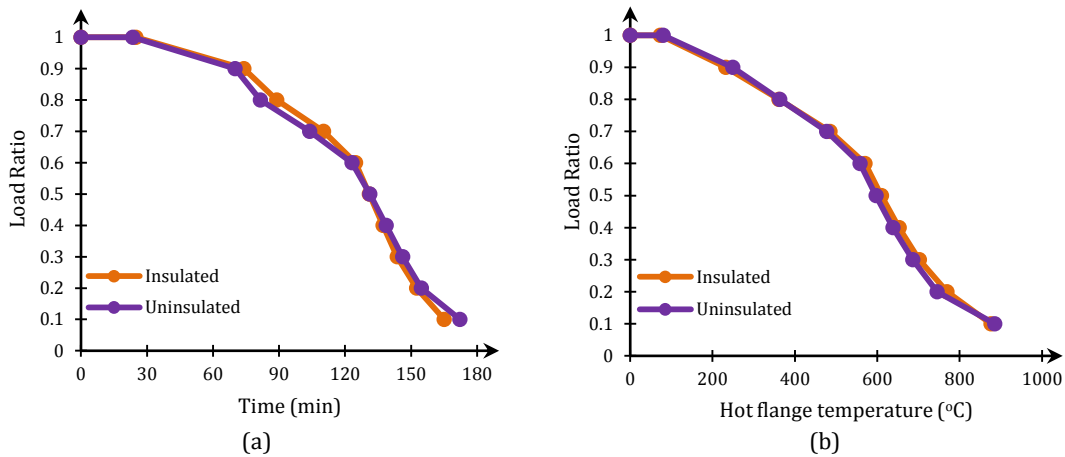The thermal analyses performed provided us with load ratio to time and temperature curves. Studs sheathed in two plasterboard layers show similar reduction curve shapes to the ones obtained from one plasterboard layer cladding. Two layer formations delay their strength deterioration due to the incorporation of an additional plasterboard layer; however, resembling mathematical equations can predict the reduction curve shapes obtained from the two differentiated configurations with a time delay factor. This fact is depicted in the next figure where load ratio is plotted against time for every case.
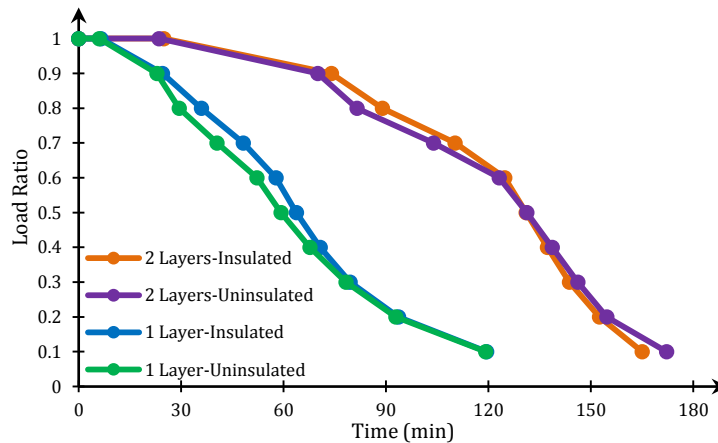


Figure 4-9: Load ratio variation with time for every examined specimen

In order to properly understand the structural behavior we should examine the response in the temperature domain. With temperature building up differential thermal extensions, thermal bowing and mechanical properties reduction is introduced. Irrespective of the insulation types and sheathing formation, eventually, temperature is going to increase in the member under investigation. Cavity insulation does not seem to affect the cross-sectional temperature increase; instead, it affects the cross-sectional temperature variation along with the sheathing formation type (single or double plasterboard layer). Insulated formations present lower cold flange temperatures throughout the whole analysis steps compared to uninsulated configurations. On

the other hand, the exposed flange temperature of insulated assemblies seems to overlap the respective temperature of uninsulated formations after 600ᵒC. These observations can be noticed in the next two figures.
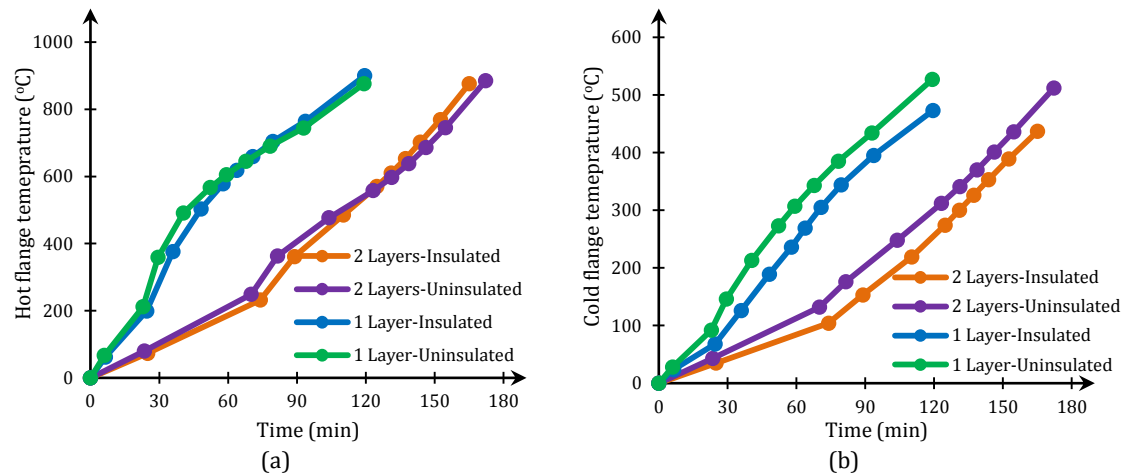


Figure 4-10: Temperature increase with time concerning (a) hot flange and (b) cold flange

EN 1993-1-2 suggests that when non-uniform temperature distribution is applied, the maximum cross-sectional temperature shall be used to carry out the analytical calculations. To that end, we examined the relationship of the axial bearing capacity deterioration and the different cross-sectional temperature values. Those values include, exposed flange temperature, unexposed flange temperature, temperature variation across the member and average cross-sectional temperature. Our goal is to exploit the temperature aspect that seems to contribute the most to the axial strength reduction irrespective of sheathing and cavity preference. Thereby, the maximum cross-sectional temperature truly seems to be the most precise temperature component that affects the loss of strength while average temperature seems to also to be consistent between each sheathing formation. Cold flange temperature demonstrates a significant, almost constant, variation between each assembly and temperature variation cannot be taken into account, especially for temperatures higher than 200ᵒC.
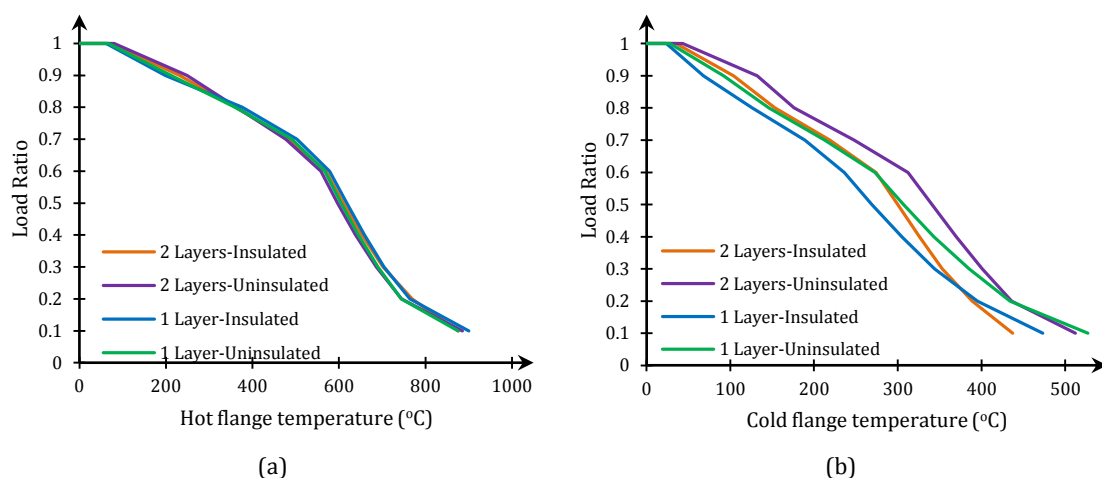


Figure 4-11: Load ratio decrease with respect to (a) hot and (b) cold flange temperature
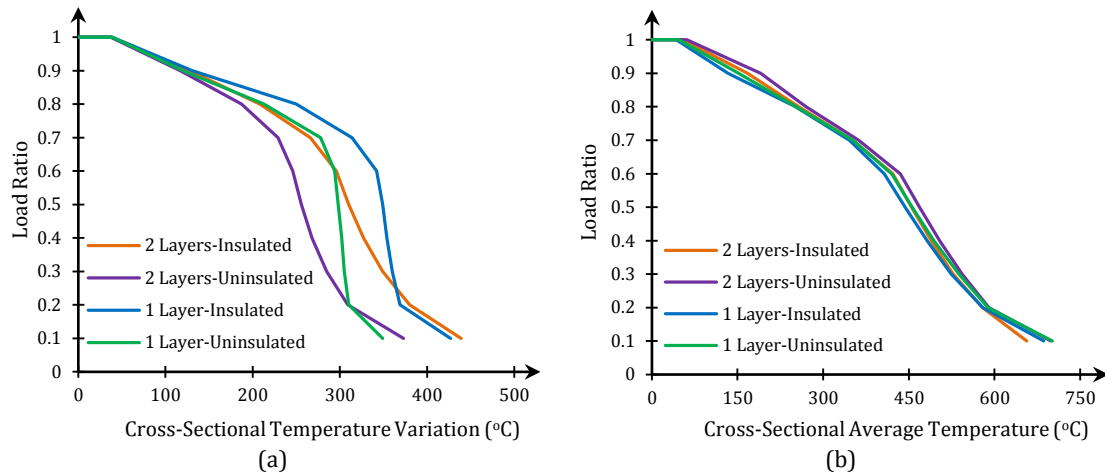
Figure 4-12: Load ratio decrease with respect to (a) temperature variation and (b) average temperature

As it was previously stated, the results of the computational model can be directly compared to the analytical calculations executed according to Eurocode 3 and the Direct Strength Method. The EN 1993 method can be divided into two different methodologies. The one is the original EN 1993-1-2 solution process based on the effective area computed according to EN 1993-1-3 for cold formed sections that was demonstrated in the previous chapter. The other method derives using the equations provided by EN 1993-1-3 after incorporating the reduced mechanical properties of steel at elevated temperatures. Note that the proper methodology according to the EN standards is the one executed according to EN 1993-1-2. The DSM is performed after running sequential linearized buckling analyses using CUFSM with gradually diminishing values of Elasticity Modulus. Then, by utilizing the elastic critical buckling loads corresponding to local, distortional and global buckling modes we can estimate the axial strength using the process suggested by the DSM.

The analytical solutions based on EN provisions and the semi-analytical solution based on DSM provided us with similar load ratio to temperature curves. These three methods are plotted together with the FEM solution using the temperature of the hot flange and equation 4.22 of EN 1993-1-2 which provides a typical relationship between load ratio and increased temperature. The DSM still provides impressively accurate results considering its easier applicability compared to the EN methods while the formal EN 1993-1-2 results prove to be significantly over-conservative with respect to the FEM output. The modified EN 1993-1-3 method presents better results compared to the EN 1993-1-2 methodology. Furthermore, the informative equation 4.22 seems to be very precise for loads below 70% of the axial strength at ambient conditions.
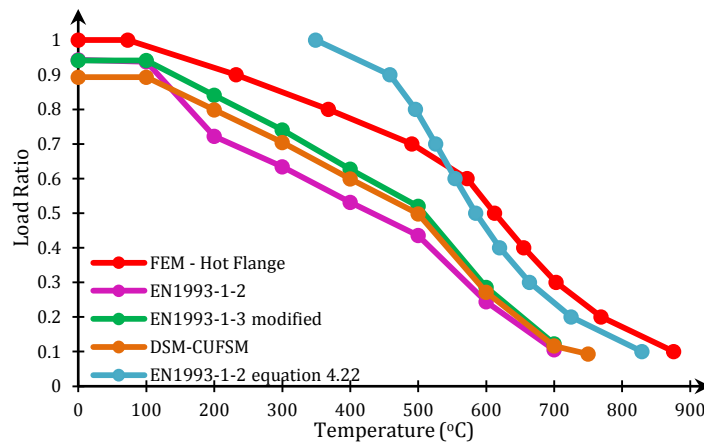
Figure 4-13: Comparison of EN1993 and DSM results with the numerical solution

Eurocode-based methods do not consider the effects of the shift of the major and minor axis nor do they explicitly calculate the effects of thermal bowing. In both cases, the magnification effects due to the additional deflections caused by the axial load are not directly addressed as well. Nonetheless, EN recommends the use of the maximum cross-sectional temperature to carry out the calculations. Trying to identify the coincidence of uniform temperature distribution with our analytical solutions we imposed a uniform temperature profile in the stud, too. The results presented in (Figure 4-14) illustrate the congruency between EN methods and DSM with models based on finite elements subjected to uniform temperature variation across the section.

When uniform temperature is applied we expect an earlier failure due to reduced mechanical properties and increased deformations across the section. However, differential elongations created by a temperature gradient when non-uniform temperature profiles are imposed, cause additional internal forces and lead to sudden failure for high load ratios. When the initial induced load lies near the maximum axial compressive load that the stud can safely bear, even slight differential deformations across the member create stresses that quickly deduce the remaining strength, thus leading to failure. This fact is shown in the next figure where the uniform temperature curve seems to surpass the non-uniform curve at low temperatures that correspond to high load ratios. At moderate and high temperatures, uniform temperature profiles have a 10% to 20% reduced axial strength compared to the non-uniform cases.
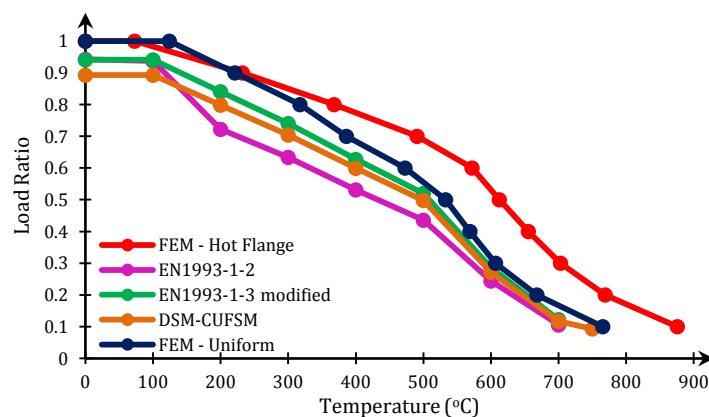


Figure 4-14: Comparison of EN and DSM results with FE uniform and non-uniform temperature analysis

Load ratio reduction with respect to uniformly applied temperature verifies the accuracy of the proposed and modified analytical and semi-analytical solutions according to EN and the DSM. The uniform temperature curve provides higher load ratios at each temperature compared to the regulations' provisions; thus verifying an acceptable conservative ratio for each case. This ratio is expressed in terms of load ratio difference at specific temperature values between the "FEM - Uniform" curve and the other curves. This variation falls within a range of 2% to 20% of the load ratio; the upper bound of this range is designated by the official EN 1993-1-2 method while the lower bound results from the EN 1993-1-3 modified methodology. The fore-mentioned range is arguably acceptable considering the uncertainties of the proposed solution processes; thus establishing a very good relationship between the closed-form proposed expressions and the numerical results.

On the other hand, the analytical solutions and the hot flange-related non-uniform temperature cases can be hardly seen as similar. Load ratio as a function of hot flange temperature provides in general 20% higher load ratios at specific temperature values compared to the close-formed expressions. This variation reaches even a 30% load ratio differential in many cases. This load ratio deficit clarifies the over-conservativeness incorporated in the proposed models yielding inefficient solutions in cases of non-uniform temperature profiles. In the attempt to outflank this fact we also plot the load ratio to cold flange and average cross-sectional temperature, the results are depicted in the next figure. Since different failure types and mechanisms are likely to occur as the temperature gradually increases, choosing other temperature values -and not the maximum temperature- might provide us with higher coincidence at some temperatures.
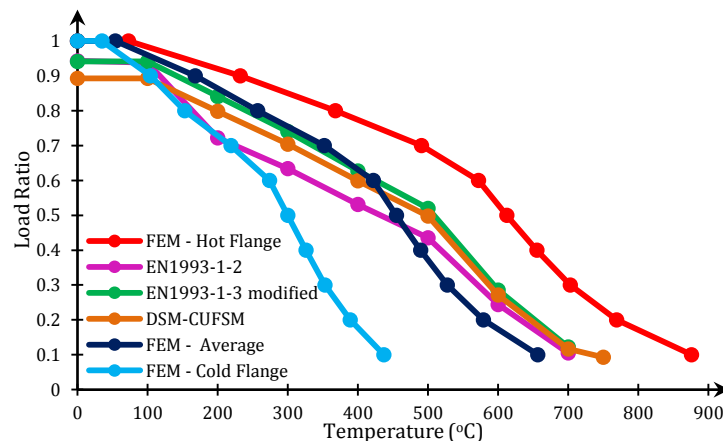


Figure 4-15: Load ratio variation with different temperature values

The average temperature curve converges significantly well with the analytical estimations; much better than cold or hot flange-related temperature values. However, for temperatures higher than 400 ºC the analytical estimations provide non-conservative results, approximately 10% higher load ratio than the FEM. On the contrary, cold flange temperature does not seem to demonstrate any significance with the results. The curve presents a linear decadence that falls within an area with reduced load ratios compared to the other solutions.

### 4.4.3    Failure modes and equilibrium paths

When we examined the structural performance at ambient temperature, a series of non-linear analyses were carried out using different imperfection values. Back then, our goal was to understand the different strength reduction patterns that unraveled after using different combinations of buckling modes and imperfection amplitudes. We observed the susceptibility of the stud to distortional buckling and we concluded that the bearing capacity in terms of a concentric compressive load can be accurately put around 70kN. The shape of deformation at failure varied at each case but distortional buckling was predominant in almost every case such as the ones depicted below (Figure 4-16a-f). These figures represent the shape of deformation at failure using imperfections according to the local, distortional and global modes individually; they also include combinations of those modes with different imperfection amplitudes. The dominant distortional buckling shape is evident in the examination of the thermal performance despite of the effect of thermal bowing; resulting from the inherent tendency of the stud to buckle in such a way.



(a)                                    (b)                                    (c)

(d)                                    (e)                                    (f)
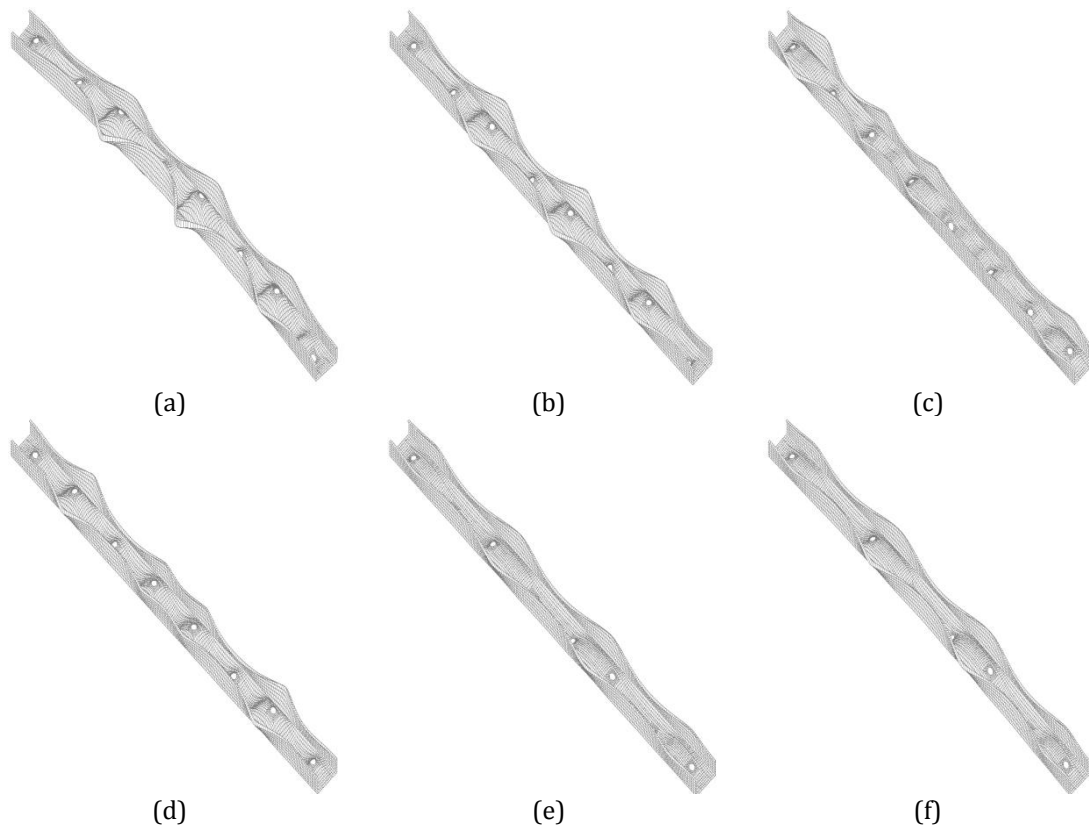
Figure 4-16: Failure shapes for various mode-imperfection combinations

The rising non-uniform temperature across the section induces additional effects that interfere in the structural behavior during ambient conditions. First, neutral axis shift, caused by the reduced stiffness of the exposed side, generates a bending moment that induces additional compressive forces at the exposed side and tensile forces on the ambient side of the cross-section. Furthermore, the differential thermal expansion due to non-uniform temperature will cause thermal bowing, i.e. bowing of the stud towards the furnace. Thermal bowing imposes tensile

forces on the fire side and compressive forces on the ambient side. As a result, hot and cold flanges are prone to failure at specific points along the stud's height.

Near the support, compressive forces due to both the external load and the neutral axis shift are applied at the hot flange. On the other hand, the cold flange is strained by the compressive external load and a tensile force caused by the shift of the neutral axis. At mid-height, thermal bowing will also develop interacting with the other phenomena. A net bending moment will be generated due to neutral axis shift and thermal bowing causing compressive forces on the ambient side and tensile forces on the fire side. Hence, the cold side is compressively strained by the external load and the net effect of bending moment, whereas the hot flange bears a compressive external load and a tensile force due to bending. Finally, we should not that the hot flange has reduced strength compared to the cold flange due to increased temperature. Thus, the stud is likely to fail either close to the support at hot flange or near mid-height at cold flange. The interaction of the elevated temperature effects with the post buckling regime of the stud will determine the exact failure modes.

When high load ratios exist, the failure mode approximates the one occurred during ambient temperature. Distortional buckling governs buckling behavior and the effects of high temperatures have not yet aggravate to match the buckling effects. Differential thermal expansions significantly contribute to the maximum bearing load by causing enough additional stresses to lead into collapse. The member has yet to be exposed to high temperatures thus the temperature difference across the member is small and thermal bowing effects are minimal. The failure mode (Figure 4-17, T=200°C) is very close to the mode during ambient temperatures as it can be observed from the following figure.

As the temperature increases the thermal effects begin to unravel playing a vital role in the structural behavior of the member under investigation. The bending moment created mainly by thermal bowing generates enough additional compressive forces on the cold flange to initiate failure. It seems that at low temperatures the higher deterioration of the hot flange's mechanical properties compared to the cold flange is not enough to counter-balance the much higher compression imposed at the cold flange. Hence, for temperatures up to 500 degrees Celsius, failure occurs at mid-height on the ambient side of the cross-section.

For temperatures higher than 500°C the reduced mechanical properties of the hot side prove to be more susceptible than the cold side. Failure location and mode transfer from the mid-height to near the support at the exposed side of the cross-section while the progressive temperature escalation assuages the effects of distortional buckling. For temperatures around 1000 degrees Celsius, the stud cannot bear any compressive load and the maximum bearing capacity is determined only by the temperature profile across the member. Despite of the thermal effects, however, the failure locations are significantly affected by the distortional buckling half-wave lengths. Mechanical property decadence is not enough to completely mitigate the buckling effects

as it is evident that failure locations are explicitly consistent with the distortional buckling modes.



| | | |
|---|---|---|
| T=200oC | T=400oC | T=500oC |
| T=600oC | T=700oC | T=1000oC |
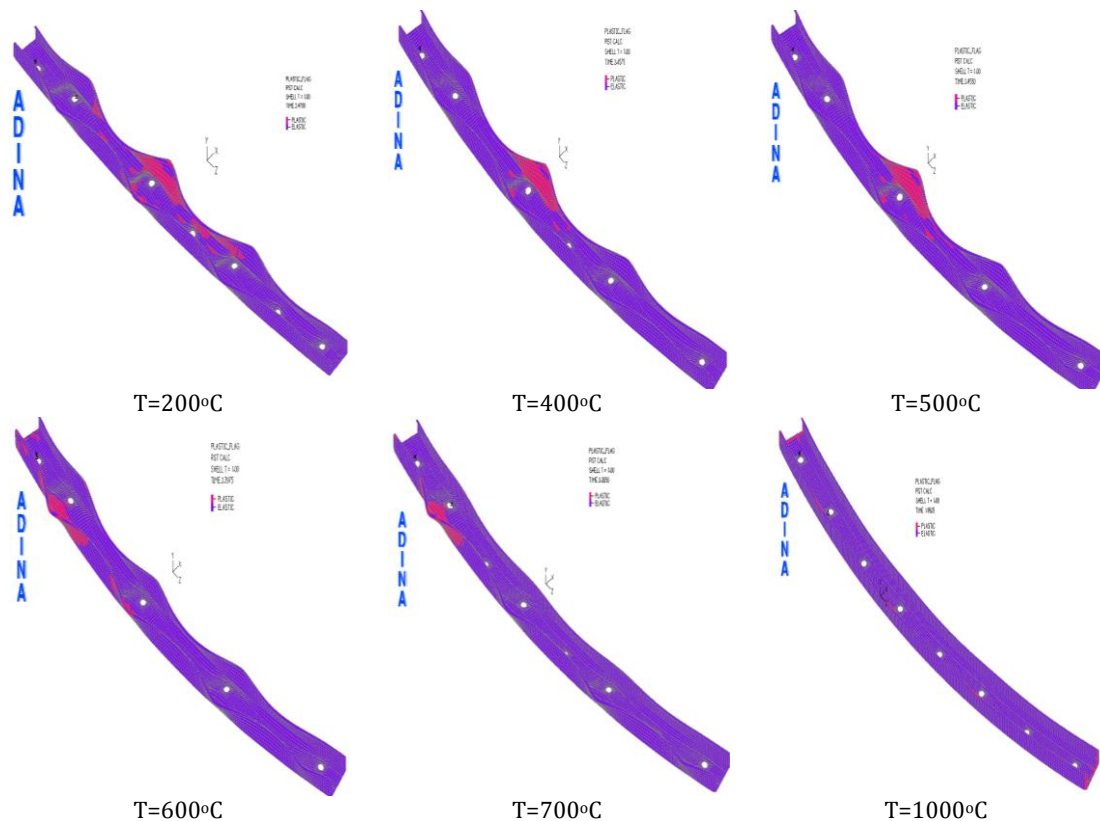
Figure 4-17: Failure modes at various temperatures

The equilibrium paths at various temperatures are presented in Figure 4-18 for the elements exhibiting the earliest failure time. The location of the elements chosen to be presented is assessed using Figure 4-17. As a result, the equilibrium paths do not represent the same element; instead, same failure modes are represented by the same node, i.e. cold or hot flange failure. Thermal bowing drives the stud in bending towards the fire; thus, moving towards the hot flange. When the imposed temperature profile reaches the ad-hoc maximum value for each case, an incremental load is imposed. For temperatures below approximately 500oC, failure occurs at the ambient side; thus, the axial load causes the cold flange to buckle in the opposite direction of the initial displacement caused by thermal bowing. Hence, the equilibrium paths for the corresponding temperatures display a turnaround after the application of the compressive load. On the other hand, when hot side failure takes place, the induced load causes the hot flange to buckle further towards the fire and the equilibrium paths for these temperatures display an additional displacement towards the fire side.
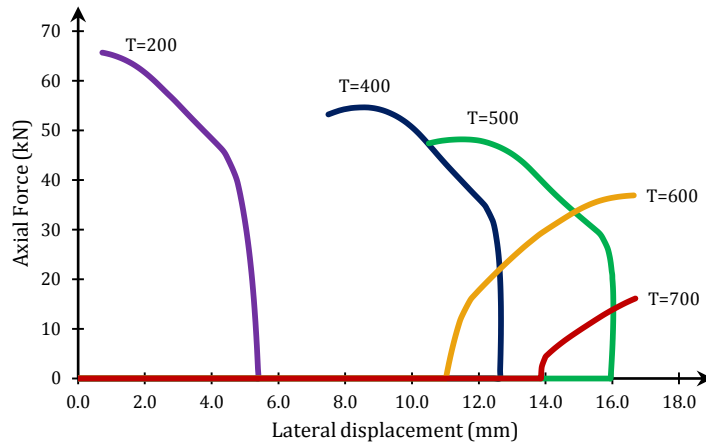
Figure 4-18: Equilibrium paths for failure nodes at various maximum temperatures

### 4.4.4    Axial force - bending moment interaction

For the purpose of aiding the design of the investigated cross-section, interaction diagrams were employed. These diagrams display the reduction of the axial bearing resistance of the stud at the presence of bending moment at various temperatures (Figure 4-20). In each case, a uniform temperature was applied and various axial force-bending moment pairs were examined in order to lay out the corresponding paths. The external bending moment was input in such a way as to produce uniform or triangular strong axis moment distribution along the member accounting for two different design situations (Figure 4-19). In any case, geometric and material non-linear analysis was performed and compared to solely material nonlinearity to elaborate the strength reduction patterns, unfolding by high temperature exposure and geometric non-linearity.



(a)                                                                      (b)

Figure 4-19: External loading causing (a) triangular and (b) uniform bending moment distribution



(a) GMNIA-uniform  distribution                    (b) GMNIA-triangular distribution

Figure 4-20: Axial force-bending moment interaction diagrams for two bending moment distributions

## 4.5 Conclusions

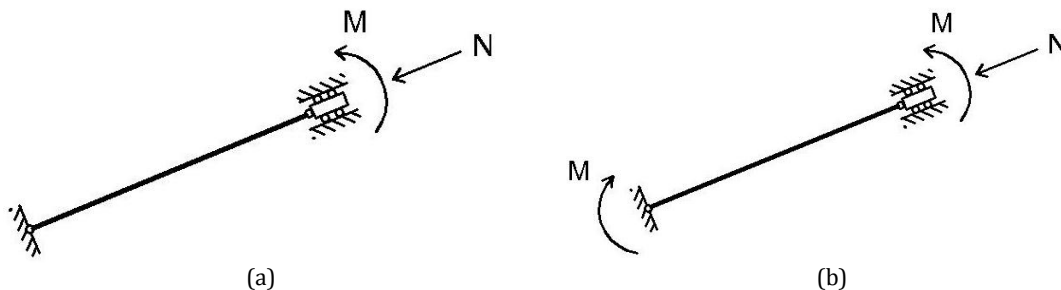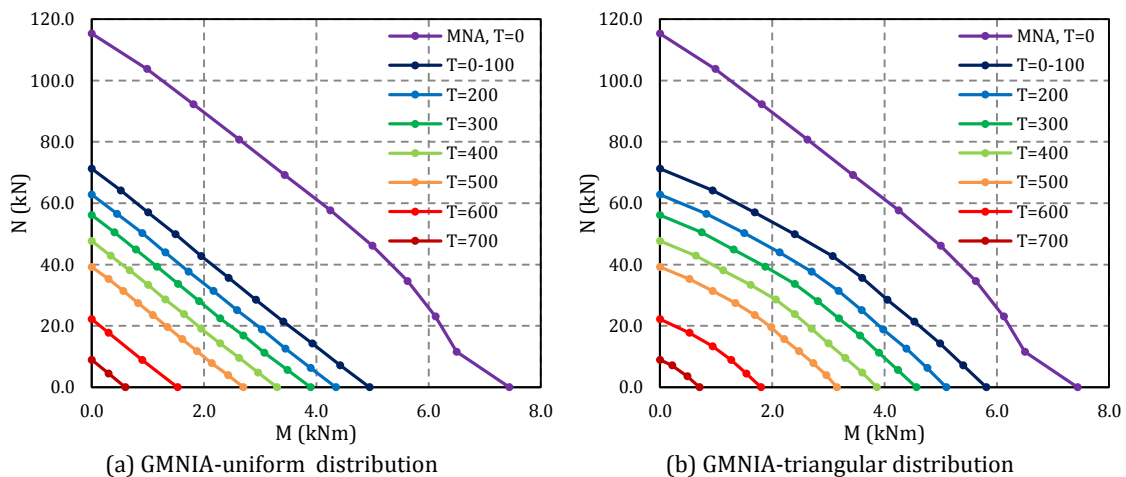This section featured a thorough investigation of the thermal and structural performance of the light-gauge steel wall under consideration. The finite element model utilized to estimate the structural response at ambient conditions is now modified to reflect the behavior at elevated temperatures. A thermo-plastic material is employed to stand for the non-linear behavior of steel exposed to fire situations. Four different drywall assemblies are examined using single or double gypsum plasterboard layers; the air cavities formed between the plasterboard layers and the steel studs are either empty or filled with mineral wool as insulation material. The structural adequacy during elevated temperatures is examined using numerical, semi-analytical and analytical methods for all configurations. Moreover, the consistency of various temperature aspects was examined to check the coincidence of strength reduction laws with different variables across non-identical models.

In order to identify a proper aspect that displays high correlation with bearing capacity deterioration for every test specimen, we examined various temperature extensions. The time domain did not provide a useful tool; although the main provider of fire safety regulations, it gives negligible information regarding the structural behavior since it is affected by non-structural options such as insulation selection. An attempt to evaluate the most representative temperature aspect, that should be considered when dealing with non-uniform elevated temperature exposure, was made. As a result, the temperature of the exposed side proved to be the most suitable value to relate to strength deterioration at fire conditions; a fact consistent with the provisions of EN 1993-1-2. It shall be noted, however, that the average temperature curve has a better fit within the range of the analytical and numerical results, but for temperatures higher than 450$^o$C, the average temperature curve provides unsafe predictions.

The numerical model consolidates the ANSYS CFX and the ADINA algorithms in order to derive the temperature profiles and investigate the structural behavior, respectively. The two orders of magnitude higher thermal conductivity of steel compared to the mineral wool, which is used as cavity insulation, creates a thermal bridge effect around the web of the cross-section, thus reducing the temperature differential across the member. This repercussion of cavity insulated drywalls has been highlighted by previous researches [85], [113], [114] suggesting that external insulation, e.g. sandwiched between plasterboard layers, counterbalances this unfavorable consequence of cavity insulation; nevertheless, the impact of cavity insulation on strength deterioration was found to be negligible based on our test specimens.

The results provided by the finite element analysis present the strength deterioration as a function of time and temperature. All drywall configurations feature similar load ratio to time curve shapes while double-layered assemblies' strength reduction exhibits a time lag resulting from the additional plasterboard layer that hinders heat transfer. Nevertheless, in the temperature domain the four configurations present almost identical strength reduction patterns; a linear reduction regime takes places for temperatures up to 500$^o$C followed by a

steeper linear part that smoothes gradually after 800°C. The area around 500°C marks the shift of failure location from mid-height cold flange to near-support hot flange. Around 750°C the specific heat of steel displays a large spike resulting from the change of the crystalline structure of steel atoms while at 800°C steel's thermal conductivity reaches a minimum. These alterations of the specific heat and thermal conductivity of steel seem to significantly affect the strength reduction pattern as the material requires more energy to increase its temperature while heat transfer is incrementally impaired across the section. Moreover, these shifting points coincide with the shifting points in the temperature-related reduction law of steel's yield stress according to EN 1993-1-2.

The semi-analytical methodology (DSM) introduced the utilization of CUFSM to acquire the elastic critical buckling loads of the three main buckling modes using diminished material properties. This swift method presented an average error of 20% of the maximum axial strength compared to the finite element model for non-uniform temperature profile and an average error of 8% for uniform cross-sectional temperature. Furthermore, the shape of the curve expressing the load ratio reduction as a function of hot flange temperature, constituted by three linear parts, is parallel to the FEA curve offset by 20% of the load ratio.

The analytical methodologies are consistent with the provisions of Eurocode 3 and incorporate suggestions of parts 1.1, 1.2 and 1.3. First, the official EN 1993-1-2 solution process was executed using the effective area calculated after EN 1993-1-3 provisions. This method proved to be the most cumbersome while its output reflected its over-conservative nature. Its deviation from the numerical solution for non-uniform temperature profiles reached as high as 30% of the initial axial resistance while its average divergence maintained a value higher than 20%. An alternative to this method, though not official, was to modify the EN 1993-1-3 provisions of estimating the bearing capacity in terms of axial compression by accounting for the degenerated elasticity modulus and yield strength values. This method comprised the higher prediction accuracy varying less than 5% from the uniform temperature curve and less than 20% from the non-uniform case results obtained using finite element modeling.

# 5 Conclusions and Recommendations

This study has presented a thorough investigation of the structural performance of LSF walls at elevated temperatures formed by lipped channel sections with web stiffeners and perforations. A literature review was performed initially, to acquire pertinent knowledge to this research field and identify the latest amendments on previous thermal and structural models proposed by other researchers. For the purpose of this thesis, a bilinear elasto-plastic constitutive material law was selected in order to represent the behavior of structural steel S320GD+Z. The commercial software ANSYS was used to determine the temperature profiles and ADINA software was utilized to carry out the structural analysis; both programs operate based on the finite element method. CUFSM was also used to verify some stages of the solution process while analytical and semi-analytical relations based on Eurocode 3 and the Direct Strength Method were also employed.

During pre-fire conditions, distortional buckling dominated the structural response while the equilibrium paths of the stud displayed an unstable secondary path. Irrespective of the mode combination examined at each stage, distortional buckling was evident at the last stage of the GMNIA. The most unfavorable mode combination was the result of the critical elastic local and distortional buckling modes, respectively. The use of CUFSM for determining the elastic buckling loads verified the results obtained from ADINA proving the efficiency of the finite strip method, even in the case of perforated members. After extracting the results of the geometric and material non-linear analysis and the derivation of the bearing capacity in terms of a vertical concentric load, the effective width method and the direct strength method were compared to the numerical results. The effective width method, based on the provision of EN 1993-1-3, had a 8.5% offset compared to the numerical solution, whereas the DSM presented a 12.5% differential.

The heat transfer analysis demonstrated the thermal bridge effect taking place around the stud's cross-section due to the two orders of magnitude higher thermal conductivity of steel compared to the thermal insulation material. However, this fact had negligible effects on the reduction of the bearing capacity of the insulated formations.

In the temperature domain, the strength reduction pattern that unfolded was similar to the reduction law of the yield stress according to EN 1993-1-2 that was incorporated in the model. Furthermore, the first shifting point of the reduction curve also marks the transition from mid-height cold-flange failure to near the support hot-flange failure; a fact consistent with relevant findings from previously conducted experiments.

In the case of uniform temperature profiles, DSM predictions differentiated only 8% on average from the numerical results while the official method of Eurocode 3 deviated approximately 15%. The modified method based on EN 1993-1-3 presented an average error of 5%. When non-

uniform temperature profiles were applied, the DSM diverged approximately 20% whereas the official EN 1993-1-2 and the modified EN 1993-1-2 methodologies displayed an average difference slightly higher and lower than 20%, compared to the numerical solution, respectively.

While our model did not account for the inhomogeneous yield stress occurring at cold-formed sections due to manufacturing, incorporation of this fact along with a proper residual stress distribution model might lead to more representative findings concerning the actual behavior. Another interesting statement would result from models that incorporate thermal creep effects. A parametric study that utilizes thermal creep models after imposing various strain rates, in order to properly address the corresponding impacts on the analysis would certainly be aligned with this perspective. Furthermore, modeling the whole plasterboard-stud system, in order to include plasterboard's stiffness and introduction of temperature-related mechanical properties for the ballistic nails would provide an additional increase in prediction accuracy. Certainly, experiment-accompanied studies would be more holistic.

Finally, the use of linear buckling analysis to determine the critical elastic buckling loads/modes at ambient temperatures could be modified in the case of non-uniform elevated temperatures. The predominant effect of thermal bowing at high elevated temperatures, especially for slender members, led many studies in concluding that initial geometric imperfection input is of little importance. Nevertheless, an attempt to incorporate the actual temperature profiles during the linear buckling analysis, by imposing differently reduced elasticity modulus values across the section to reflect the deterioration at each temperature, could result in reduced ultimate load values. This process, although more time-consuming and certainly not representative of a realistic behavior of a specific member, would capture the actual unfavorable response at each investigated temperature by implementing the most unfavorable imperfection shape specifically for each temperature profile.

# 6 References

[1]    Kolarkar, P. N. and Mahendran, M., "Thermal Performance of Plasterboard Lined Steel Stud Wall," in *Proceedings of the 19th International Specialty Conference on Cold Formed Steel Structures*, St. Louis, Missouri, USA, pp. 517 - 530, 2008.

[2]    Kirkland, W. H., Cold Roll Forming Practice in the United States, New York: American Iron and Steel Institute, 1966.

[3]    American Iron and Steel Institute, Specification for the Design of Cold-Formed Steel Structural Members, Washington, DC, 1996.

[4]    Hancock, G. J., Murray, T. M. and Ellifritt, D. S., Cold-Formed Steel Structures to the AISI Specification, New York: Marcel Dekker, Inc., 2001.

[5]    Halmos, G. T., High-Production Roll Forming, Dearborn, MI: Society of Manufacturing Engineering, 1983.

[6]    Chicago Roll Company, [Online]. Available: http://www.chicagoroll.com/AboutUs.aspx. [Accessed 15/05/2015].

[7]    Yu, W.W. and LaBoube, R.A., Cold - Formed Steel Design, New Jersey: John Wiley & Sons, Inc, 2010.

[8]    CustomPartNet, [Online]. Available: http://www.custompartnet.com/wu/sheet-metal-forming. [Accessed 17/05/2015].

[9]    Brockenbrough, R. L. and Merritt, F. S., Structural Steel Designer's Handbook, 3rd Edition, New York: McGraw-Hill, Inc, 1999.

[10]   "FrameMax," [Online]. Available: http://www.framemax.com/. [Accessed 17/05/2015].

[11]   Joseph S. P., "The Times," [Online]. Available: http://www.nwitimes.com/business/local/construction-demand-for-steel-expected-to-hit-highest-point-in/article_01a7e387-ac17-5844-9f1a-bc4bae7fd467.html. [Accessed 17/05/2015].

[12]   Thompson Research Group (TRG), "Industry Update - April Building Products Survey; Findings from TRG's "Real Life" Office Hunt," Nashville, TN, 2015.

[13]   ClarkDietrich Building Systems, "http://www.ronblank.com," 2009. [Online]. Available: http://www.ronblank.com/courses/die05h/die05h.pdf. [Accessed 24/05/2015].

[14]   Gantes, C. J., "Nonlinear Behavior of Steel Structures - Analysis and Design Implications, Chapter 1: Introduction," N.T.U.A., class notes, in preparation, Athens, 2015.

[15]   American Iron and Steel Institute, "Commentary on Appendix 1: Design of Cold-Formed Steel Structural Members with the Direct Strength Method," 2004.

[16]   Schafer, B. W. and Adany, S., "Understanding and Classifying Local, Distortional and Global Buckling in Open Thin-Walled Members," in *Proceeding of the Annual Stability Conference*, Montreal, Canada, 2005.

[17]   Chen, W. F. and Lui, E. M., Handbook of Structural Engineering, Second Edition, Boca Raton, FL: Taylor & Francis Group, LLC, 2005.

[18]   United States Steel Corporation, [Online]. Available: https://www.ussteel.com/uss/portal/home/products/sheet/Cold%20Rolled%20Sheet. [Accessed 20/05/2015].

[19]   Chajes, A., Britvec, S. J., and Winter, G., "Effects of Cold-Straining on Structural Sheet Steels," *Journal of the Structural Division, ASCE Proceedings, vol. 89,* 1963.

[20]   Karren, K. W. and Winter, G., "Effects of cold-forming on light-gage steel members," Center for Cold-Formed Steel Structures Library, Paper 138, 1965.

[21]   Britvec, S. J., Chajes, A., Warren, K. W., Uribe, J. and Winter, G., "Effects of cold work in cold-formed steel structural members," in *Center for Cold-Formed Steel Structures Library*, Paper 170, 1970.

[22]   Indacochea, J. E., "Dislocations and Plastic Deformations," University of Illinois at Chicago, Class Notes, 2015.

[23]   Gantes, C. J., "Nonlinear Behavior of Steel Structures - Analysis and Design Implications, Chapter 2: Material non-linearity," N.T.U.A., class notes, in preparation, Athens, 2015.

[24]   Rondal, J., "Residual stresses in cold-rolled profiles," *Construction and Building Materials, Vol. 1 (3),* pp. 150-164, 1987.

[25]   De Giorgi, M., "Residual stress evolution in cold-rolled steels," *International Journal of Fatigue, Vol. 33 (3),* pp. 507-512, 2011.

[26]   Schafer, B. W. and Pekoz, T., "Computational modeling of cold-formed steel: characterizing geometric imperfections and residual stresses," *Journal of Constructional Steel Research, Vol. 47 (3),* pp. 193-210, 1998.

[27]   Quacha, W. M., Tengb, J. G. and Chungb, K. F., "Residual stresses in steel sheets due to coiling and uncoiling: a closed-form analytical solution," *Engineering Structures, Vol. 26,* pp. 1249-1259, 2004.

[28]   Quacha, W. M., Tengb, J. G. and Chungb, K. F., "Finite element predictions of residual stresses in press-braked thin-walled steel sections," *Engineering Structures, Vol. 28,* p. 1609–1619, 2006.

[29]   Young, B. and Rasmussen, K. J. R., "Compression tests of fixed-ended and pin-ended cold-formed lipped channels," University Of Sydney, School Of Civil And Mining Engineering, Research Report No. R715, Sydney, Australia, 1995.

[30]   Young, B. and Rasmussen, K. J. R., "Compression tests of fixed-ended and pin-ended cold-formed lipped channels," University Of Sydney, School Of Civil And Mining Engineering, Research Report No. R714, Sydney, Australia, 1995.

[31]   Dubina, D. and Ungureanu, V., "Effect of imperfections on numerical simulation of instability behaviour of cold-formed steel members," *Thin-Walled Structures, Vol. 40 (3),* pp. 239-262, 2002.

[32]   Sadovský, Z., Kriváček, J., Ivančo, V. and Ďuricová, A., "Computational modelling of geometric imperfections and buckling strength of cold-formed steel," *Journal of Constructional Steel Research, Vol. 78,* pp. 1-7, 2012.

[33]   EN 1090-2, "Execution of steel structures and aluminium structures - Part 2: Technical requirements for steel structures," European Committee for Standardization, Brussels, 2008.

[34]   Gypsum Association, "Using Gypsum Board for Walls and Ceilings," [Online]. Available: http://www.gypsum.org. [Accessed 25/05/2015].

[35]   Gerlich, J. T., Collier, P. C. R. and Buchanan, A. H., "Design of light steel-framed walls for fire resistance," *Fire and Materials, Vol. 20,* pp. 79-96, 1996.

[36]   Yu, Q. L. and Brouwers, H. J. H. , "Thermal properties and microstructure of gypsum board and its dehydration products: A theoretical and experimental investigation," *Fire and Materials, Vol. 36,* pp. 575-589, 2012.

[37]   Thomas, G., "Thermal properties of gypsum plasterboard at high temperatures," *Fire and Materials, Vol. 26,* pp. 37-45, 2002.

[38]   Paulik, F., Paulik, J. and Arnold, M., "Thermal decomposition of gypsum," *Thermochimica Acta, Vol. 200,* pp. 195-204, 1992.

[39]   Ghazi Wakili, K. and Hugi, E., "Four Types of Gypsum Plaster Boards and their Thermo-physical Properties Under Fire Condition," *Journal of Fire Sciences, Vol. 27,* pp. 27-43, 2009.

[40]   Ghazi Wakili, K., Koebel, M., Kaufmann, J., Derluyn, H., Hofer, M., Glaettli, T. and Modregger, P., "Thermal conductivity of gypsum plasterboard beyond dehydration and its correlation with the pore structure," in *9th International Conference on Heat Transfer, Fluid Mechanics and Thermodynamics*, Malta, 2012.

[41]   Wang, H. B., "Heat transfer analysis of components of construction exposed to fire," PhD Thesis, Department of Civil Engineering and Construction, University of Salford, Manchester, 1995.

[42]   Sultan, M. A., "A Model for Predicting Heat Transfer Through Noninsulated Unloaded Steel-Stud Gypsum Board Wall Assemblies Exposed to Fire," *Fire Technology, Vol. 32 (3),* pp. 239-259, 1996.

[43]   Kaitila, O., *Finite Element Modelling of Cold-Formed Steel Members at High Temperatures,* Licentiate Thesis, Helsinki University of Technology Laboratory of Steel Structures, Espoo, 2002.

[44]   Gunalan, S., "Structural Behaviour and Design of Cold-formed Steel Wall Systems under Fire Conditions," Ph.D Thesis, Queensland University of Technology, Brisbane, Australia, 2011.

[45]   Bénichou, N., Sultan, M. A., MacCallum, C. and Hum, J., "Thermal Properties of Wood, Gypsum and Insulation at Elevated Temperatures," Institute for Research in Construction, National Research Council Canada, Internal Report, 710, 2001.

[46]   DiNenno P. J., Beyler C. L., Custer R. L. P., Walton W. D. and Watts, Jr., J. M., SFPE Handbook of Fire Protection Engineering, 3rd Edition, Massachusetts: National Fire Protection Association, 2002.

[47]   Sultan, M. A., "Effect of Insulation in the Wall Cavity on the Fire Resistance Rating of Full-Scale Asymmetrical (1×2) Gypsum Board Protected Wall Assemblies," in *Proceedings of the International Conference on Fire Research and Engineering, Orlando*, Boston, 1995.

[48]  Wang, Y., Burgess, I., Wald, F. and Gillie, M., "Performance-based fire engineering of structures," CRC Press, 2012.

[49]  Poh, K. W., "Stress-strain-temperature relationship for structural steel," *Journal of Materials in Civil Engineering, Vol. 13 (5),* pp. 371-379, 2001.

[50]  Outinen, J., Kesti, J., and Mäkeläinen, P., "Fire design model for structural steel S355 based upon transient state tensile test results," *Journal of Constructional Steel Research, Vol. 42 (3),* pp. 161-169, 1997.

[51]  Chen, J., Young, B., and Uy, B., ""Behavior of high strength structural steel at elevated temperatures," *Journal of Structural Engineering, Vol. 132 (12),* pp. 1948-1954, 2006.

[52]  Anderberg, Y., "Modelling Steel Behaviour," in *International Conference on Design of Structures Against Fire*, Birmingham, UK, 1986.

[53]  Twilt, L., "Strength and Deformation Properties of Steel at Elevated Temperatures: Some Practical Implications," *Fire Safety Journal, Vol. 13,* pp. 9-15, 1988.

[54]  Kodur, V., Dwaikat, M. and Fike, R., "High-Temperature Properties of Steel for Fire Resistance Modeling of Structures," *Journal of Materials in Civil Engineering, Vol. 22 (5),* pp. 423-434, 2010.

[55]  Outinen, J., and Mäkeläinen, P., "Mechanical properties of structural steel at elevated temperatures and after cooling down," in *Second International Workshop « Structures in Fire »*, Christchurch, 2002.

[56]  Zhao, B., Kruppa, J., Renaud, C., O'Connor, M., Mecozzi, E., Apiazu, W., Demarco, T., Karlstrom, P., Jumppanen, U., Kaitila, O., Oksanen, T. and Salmi, P., "Calculation rules of lightweight steel sections in fire situations," Technical Steel Research, European Union, 2005.

[57]  Dolamune Kankanamge, N. and Mahendran, M., "Mechanical properties of cold-formed steels at elevated temperatures," *Thin-Walled Structures, Vol. 49,* pp. 26-44, 2011.

[58]  Cooke, G. M. E., "An introduction to the mechanical properties of structural steel at elevated temperatures," *Fire Safety Journal, Vol. 13 (1),* pp. 45-54, 1988.

[59]  Choi, I. R., Chung, K. S. and Kim, D. H., "Thermal and mechanical properties of high-strength structural steel HSA800 at elevated temperatures," *Materials and Design, Vol. 63,* pp. 544-551, 2014.

[60]  Kodur, V., Kand, S. and Khaliq, W., "Effect of Temperature on Thermal and Mechanical Properties of Steel Bolts," *Journal of Materials in Civil Engineering, Vol. 24 (6),* pp. 765-774, 2012.

[61]  Dorn, J. E., "Some fundamental experiments on high temperature creep," *Journal of the Mechanics and Physics of Solids, Vol. 3,* pp. 85-116, 1955.

[62]  Harmanthy, T., "A comprehensive creep model," *Journal of Basic Engineering, Vol. 89 (D-3),* pp. 496-502, 1967.

[63]  ANSYS 15.0, "User's Guide," ANSYS, Inc., Canonsburg, U.S.A., 2013.

[64]  The Institution of Structural Engineers (IStructE), Introduction to the fire safety engineering of structures, London: The Institution of Structural Engineers, 2003.

[65]  Lataille, J. I., Fire Protection Engineering in Building Design, USA: Elsevier Science, 2003.

[66]  Purkiss, J. A., Fire Safety Engineering - Design of Structures, Second Edition, Oxford: Elsevier Ltd, 2007.

[67]  Stirland, C., "Sprinklers and the Building Regulations: the Case for Tradeoffs," Report T/RS/1189/22/81/C, Teesside Laboratory, British Steel, Middlesborough, 1981.

[68]  Malhotra, H. L., "Fire compartmentation: needs and specification," *Fire Surveyor, Vol. 22 (2),* pp. 4-9, 1993.

[69]  EN 1991-1-2, Eurocode 1: Actions on Structures - Part 1.2: General Actions - Actions on structures exposed to fire, Brussels: European Committee for Standardization, 2002.

[70]  Law, M., "A review of formulae for T - equivalent," in *Proceedings of Fifth International Symposium on Fire Safety Science*, Melbourne, Australia, 1997.

[71]  Harmathy, T. Z. and Mehaffey, J .R., "Design of buildings for prescribed levels of structural fire safety," in *Fire Safety: Science and Engineering*, Philadelphia, 1985.

[72]  Williams-Lier, G., "Analytical equivalents of standard fire temperature curves," *Fire Technology, Vol. 9,* pp. 132-136, 1973.

[73]  Fackler, J. P., "Concernant la résistance au feu des éléments de," *Cahiers du Centre Scientifique et Technique du Bâtiment, Vol. 37,* pp. 1-20, 1959.

[74] Hietaniemi, J. and Mikkola, E., Design Fires for Fire Safety Engineering, Finland: VTT Technical Research Centre of Finland, 2010.

[75] Drysdale, D., An introduction to fire dynamics, Chichester: John Wiley & Sons Ltd, 1999.

[76] Latham, D. J., Kirby, B. R. and Thomson, G., "The Temperatures Attained by Unprotected Structural Steelwork in Experimental Natural Fires," *Fire Safety Journal, Vol. 12,* pp. 139-152, 1987.

[77] Alfawakhiri, F. and Sultan, M. A., "Fire Resistance of Loadbearing LSF Assemblies," Institute for Research in Construction, National Research Council Canada, Report 41533, 2000.

[78] Chen, J. and Young, B., "Cold-formed steel lipped channel columns at elevated temperatures," *Engineering Structures, Vol. 29,* pp. 2445-2456, 2007.

[79] ABAQUS, "Analysis user's manual," ABAQUS, Inc., 2004.

[80] Young, B. and Rasmussen, K. J. R., "Design of lipped channel columns," *Journal of Structural Engineering, Vol. 124,* pp. 140-148, 1998.

[81] Feng, M., Wang, Y. C. and Davies, J. M., "Structural behaviour of cold-formed thin-walled short steel channel columns at elevated temperatures. Part 1: Experiments.," *Thin Walled Structures, Vol. 41 (6),* pp. 543-570, 2003.

[82] Ranawaka, T. and Mahendran M., "Distortional buckling tests of cold-formed steel compression members at elevated temperatures," *Journal of Constructional Steel Research, Vol 65,* pp. 249-259, 2009.

[83] "Numerical modelling of light gauge cold-formed steel compression members subjected to distortional buckling at elevated temperatures," *Thin-Walled Structures, Vol. 48,* pp. 334-344, 2010.

[84] Ranawaka, T. and Mahendran, M., "Mechanical properties of thin steels at elevated temperatures," in *Proceedings of the 4th international workshop, Structures in fire*, Portugal, 2006.

[85] Kolarkar, P. N., "Fire Performance of Plasterboard Lined Steel Stud Walls," PhD Thesis, Queensland University of Technology, Brisbane, Australia, 2010.

[86] Gunalan, S., Kolarkar, P. and Mahendran, M., "Experimental study of loadbearing cold-formed steel wall systems under fire conditions," *Thin-Walled Structures, Vol. 65,* pp. 72-92, 2013.

[87]    Gunalan, S. and Mahendran, M., "Finite element modelling of load bearing cold-formed steel wall systems under fire conditions," *Engineering Structures, Vol. 56,* pp. 1007-1027, 2013.

[88]    Gunalan, S. and Mahendran, M., "Development of improved fire design rules for cold-formed steel wall systems," *Journal of Constructional Steel Research, Vol. 88,* pp. 339-362, 2013.

[89]    Gunalan, S. and Mahendran, M., "Fire performance of cold-formed steel wall panels and prediction of their fire resistance rating," *Fire Safety Journal, Vol. 64,* pp. 61-80, 2014.

[90]    Gunalan, S., Bandula Heva, Y., and Mahendran, M., "Flexural–torsional buckling behaviour and design of cold-formed steel compression members at elevated temperatures," *Engineering Structures, Vol. 79,* pp. 149-168, 2014.

[91]    Gunalan, S. and Mahendran, M., "Improved design rules for fixed ended cold-formed steel columns subject to flexural–torsional buckling," *Thin-Walled Structures, Vol. 73,* pp. 1-13, 2013.

[92]    Gunalan, S., Bandula Heva, Y., and Mahendran, M., "Local buckling studies of cold-formed steel compression members at elevated temperatures," *Journal of Constructional Steel Research, Vol. 108,* pp. 31-45, 2015.

[93]    Ariyanayagam, A. D., and Mahendran, M., "Numerical modelling of load bearing light gauge steel frame wall systems exposed to realistic design fires," *Thin-Walled Structures, Vol. 78,* pp. 148-170, 2014.

[94]    Barnett C. R., "BFD curve: a new empirical model for fire compartment temperatures," *Fire Safety Journal, Vol. 37,* pp. 437-463, 2002.

[95]    Ranawaka, T. and Mahendran, M., "Experimental study of the mechanical properties of light gauge cold-formed steels at elevated temperatures," *Fire Safety Journal, Vol. 44 (2),* pp. 219-229, 2009.

[96]    Landesmann, A. and Camotim, D., "DSM to predict distortional failures in cold-formed steel columns exposed to fire: Effect of the constitutive law temperature-dependence," *Computers and Structures, Vol. 147,* pp. 47-67, 2015.

[97]    Bebiano, R., Pina, P., Silvestre, N. and Camotim, D., "GBTUL 1.0β - Buckling and Vibration Analysis of Thin-Walled Members," DECivil/IST, Technical University of Lisbon, Portugal, 2008.

[98]   Lee, J. H., Mahendran, M. and Makelainen, P., "Prediction of mechanical properties of light gauge steels at elevated temperatures," *Journal of Constructional Steel Research, Vol. 59 (12),* pp. 1517-1532, 2003.

[99]   Chen, J. and Young, B., "Experimental investigation of cold-formed steel material at elevated temperatures," *Thin-Walled Structures, Vol. 45 (1),* pp. 96-110, 2007.

[100] Wei, C. and Jihong, Y., "Mechanical properties of G550 cold-formed steel under transient and steady state conditions," *Journal of Constructional Steel Research, Vol. 73,* pp. 1-11, 2012.

[101] Feng, M. and Wang, Y. C., "An analysis of the structural behaviour of axially loaded full-scale cold-formed thin-walled steel structural panels tested under fire conditions," *Thin-Walled Structures, Vol 43,* pp. 291-332, 2005.

[102] ADINA R & D, Inc, *ADINA System 9.0, Release Notes,* Watertown, MA, 2013.

[103] Li, Z. and Schafer, B. W., "Buckling analysis of cold-formed steel members with general boundary conditions using CUFSM: conventional and constrained finite strip methods," in *Proceedings of the 20th Int;l. Spec. Conf. on Cold-Formed Steel Structures*, St. Louis, MO, 2010.

[104] Feng, M., Wang, Y. C. and Davies, J. M., "Axial strength of cold-formed thin-walled steel channels under non-uniform temperatures in fire," *Fire Safety Journal, Vol. 38,* pp. 679-707, 2003.

[105] Schafer, B. and Pekoz, T., "Direct Strength Prediction of Cold-Formed Steel Members Using Numerical Elastic Buckling Solutions," in *Proceedings, Second International Conference on Thin-Walled Structures*, Singapore, 1998.

[106] EN 1993-1-5, Eurocode 3: Design of steel structures - Part 1.5: General rules - Plated structural elements, Brussels: European Committee of Standardization, 2004.

[107] EN 1993-1-1, "Eurocode 3: Design of steel structures - Part 1-1: General rules and rules for buildings," European Committee for Standardization, Brussels, 2005.

[108] EN 1993-1-3, Eurocode 3: Design of steel structures - Part 1.3: General rules - Supplementary rules for cold-formed members and sheeting, Brussels: European Committee of Standardization, 2006.

[109] ISO 834 - 1, "Fire-resistance tests - Elements of building construction - Part 1: General requirements," Internation Organization for Standardization, Switzerland, 1999.

[110] Kolaitis, D. I. and Founti, M. A., "Development of a solid reaction kinetics gypsum dehydration model appropriate for CFD simulation of gypsum plasterboard wall assemblies exposed to fire," *Fire Safety Journal, Vol. 58,* pp. 151-159, 2013.

[111] EN1993-1-2, Eurocode 3: Design of steel structures - Part 1-2: General rules - Structural fire design, Brussels: European Committee of Standardization, 2002.

[112] ISO 6946, Building components and building elements - Thermal resistance and thermal transmittance - Calculation method, Switzerland: International Organization for Standardization, 1996.

[113] Alfawakhiri F., "Behaviour of cold-formed-steel-framed walls and floors in standard fire resistance tests," PhD thesis, Carlton University, Ontario, Canada, 2001.

[114] Kodur, V. R. and Sultan, M. A., "Factors governing fire resistance of load-bearing steel," in *Proceeding of the fifth AOSFST international conference*, Newcastle, Australia, 2001.

[115] Kenedi, R. M., and Shearer Smith W., Applications of Colf-Formed Sections, Glasgow: The West of Scotland Iron and Steel Institute, 1958.

[116] American Iron and Steel Institute, North American Specification for the Design of Cold-Formed Steel Structural Members, Washington, DC: AISI/COS/NASPEC 2001, 2001.

[117] Bentz, D. P. and Prasad, K. R., "Thermal Performance of Fire Resistive Materials I. Characterization with Respect to Thermal Performance Models," National Institute of Standards and Technology, Gaithersburg, 2007.